
Phase separation of active fluids

Inaugural-Dissertation

zur Erlangung des Doktorgrades
der Mathematisch-Naturwissenschaftlichen Fakultät
der Heinrich-Heine-Universität Düsseldorf

vorgelegt von

Alexander Julian Marcel Bialké

aus Düsseldorf

Düsseldorf, März 2015

aus dem Institut für Theoretische Physik II: Weiche Materie
der Heinrich-Heine-Universität Düsseldorf

Gedruckt mit der Genehmigung der
Mathematisch-Naturwissenschaftlichen Fakultät der
Heinrich-Heine-Universität Düsseldorf

Referent: Prof. Dr. Hartmut Löwen
Korreferent: Prof. Dr. Thomas Speck

Tag der mündlichen Prüfung: 27.03.2015

Preface

In January 2012 I have started working on my dissertation together with my supervisor Prof. Dr. Hartmut Löwen at the department for Theoretical Physics II: Soft Matter at the Heinrich - Heine - University of Düsseldorf. During this process I have had the privilege to work at the current state of research, present my work within the scope of international conferences and publish results in scientific journals. I would not miss any of the experiences I have made during the last years, especially dealing with failures along the route towards success.

I want to take this opportunity and thank Prof. Dr. Hartmut Löwen for giving me the chance to apply for a doctoral degree and to work with him, which was a great experience. I appreciate his support throughout the whole time and thank him for always having an open ear regarding any concerns. I would also like to express my gratitude to Prof. Dr. Thomas Speck, with whom I have had the pleasure to collaborate very closely and who has always taken time to give me helpful advices. Special thanks goes to my colleagues Matthias Kohl, Tobias Glanz, Nicolas Höft and Andreas Kaiser for proofreading my thesis.

Finally, I would like to express my special appreciation and thanks to my mother who supported me extensively during my academic career. One catchy moment was for sure in 9th grade where we both went through the physical concept of a refrigerator to prepare myself for a written exam. Probably the time where I began to develop a growing interest in physics, eventually leading to this thesis. What a memorable journey!

Düsseldorf, February 2, 2015

List of published work

This thesis is based on the publications listed below. Most of the text has been rewritten but some parts are similar to the original publications.

[1] **Dynamical Clustering and Phase Separation in Suspensions of Self-Propelled Colloidal Particles**

I. Buttinoni, J. Bialké, F. Kümmel, H. Löwen, C. Bechinger, and T. Speck
Physical Review Letters **110**, 238301 (2013).

Abstract: We study experimentally and numerically a (quasi-)two-dimensional colloidal suspension of self-propelled spherical particles. The particles are carbon-coated Janus particles, which are propelled due to diffusiophoresis in a near-critical water-lutidine mixture. At low densities, we find that the driving stabilizes small clusters. At higher densities, the suspension undergoes a phase separation into large clusters and a dilute gas phase. The same qualitative behavior is observed in simulations of a minimal model for repulsive self-propelled particles lacking any alignment interactions. The observed behavior is rationalized in terms of a dynamical instability due to the self-trapping of self-propelled particles.

Statement of the author: This paper was written in close collaboration with the 2. *Physikalisches Institut* of the University of Stuttgart. The authors affiliated with the University of Stuttgart, namely I. Buttinoni, F. Kümmel and C. Bechinger, have cooperatively obtained and analyzed all experimental data of this paper. The computer simulations and analysis of numerical results was done by me while T. Speck created the figures concerning numerical results. H. Löwen, C. Bechinger and T. Speck merged the experimental and numerical results and organized the outline of the paper. The numerical results and parts of the experimental results of the article will mainly be presented in Chap. 3.

[2] **Microscopic theory for the phase separation of self-propelled repulsive disks**

J. Bialké, T. Speck, H. Löwen
Europhysics Letters **103**, 30008 (2013).

Abstract: Motivated by recent experiments on colloidal suspensions, we study analytically and numerically a microscopic model for self-propelled particles lacking alignment interactions. In this model, even for purely repulsive interactions, a dynamical instability leading to phase separation has been reported. Starting from the many-body Smoluchowski equation, we develop a mean-field description based on a novel closure scheme and derive the effective hydrodynamic equations. We demonstrate that the microscopic origin of the instability is a force imbalance due to an anisotropic pair distribution leading to self-trapping. The phase diagram can be understood in terms of two quantities: a minimal drive and the force imbalance. At sufficiently high propulsion speeds there is a reentrance into the disordered fluid.

Statement of the author: This paper was mainly written by T. Speck and me. The theory was derived by T. Speck while permanent meetings with H. Löwen and me occurred on a regular basis. In close collaboration with T. Speck I have followed the theory and reassured its correctness. In addition I have bridged the gap between theory and simulation by performing and analyzing computer simulations and comparing the results to the theoretical predictions. H. Löwen helped by supervising and guiding the whole working process and organizing the outline of this article. The results of this paper will mostly be presented in Chap. 3.

[3] **Effective Cahn-Hilliard Equation for the Phase Separation of Active Brownian Particles**

T. Speck, J. Bialké, A. M. Menzel, H. Löwen
Physical Review Letters **112**, 218304 (2014).

Abstract: The kinetic separation of repulsive active Brownian particles into a dense and a dilute phase is analyzed using a systematic coarse-graining strategy. We derive an effective Cahn-Hilliard equation on large length and time scales, which implies that the separation process can be mapped onto that of passive particles. A lower density threshold for clustering is found, and using our approach we demonstrate that clustering first proceeds via a hysteretic nucleation scenario and above a higher threshold changes into a spinodal-like instability. Our results are in agreement with particle-resolved computer simulations and can be verified in experiments of artificial or biological microswimmers.

Statement of the author: This article was written by T. Speck and me. The analytical part of the paper was derived by T. Speck and A. M. Menzel. I have connected the results of computer simulations with the outcome of the theory. H. Löwen contributed by guiding the theoretical as well as the numerical working process and arranging the outline of the paper. This work will be discussed in Chap. 4.

[4] **Active colloidal suspensions: Clustering and phase behavior**

J. Bialké, T. Speck, H. Löwen

Journal of Non-Crystalline Solids **407**, 367 (2015), 7th IDMRCs: Relaxation in Complex Systems.

Abstract: We review recent experimental, numerical, and analytical results on active suspensions of self-propelled colloidal beads moving in (quasi-)two dimensions. Active colloids form part of the larger theme of active matter, which is noted for the emergence of collective dynamic phenomena away from thermal equilibrium. Both in experiments and computer simulations, a separation into dense aggregates, i.e., clusters, and a dilute gas phase has been reported even when attractive interactions and an alignment mechanism are absent. Here, we describe three experimental setups, discuss the different propelling mechanisms, and summarize the evidence for phase separation. We then compare experimental observations with numerical studies based on a minimal model of colloidal swimmers. Finally, we review a mean-field approach derived from first principles, which provides a theoretical framework for the density instability causing the phase separation in active colloids.

Statement of the author: This review article was mainly written by me. T. Speck wrote parts of the article and helped with the creation of figures. H. Löwen and T. Speck contributed by linking the results of the different works considered and organizing the outline of the paper.

[5] **Negative interfacial tension in phase-separated active suspensions**

J. Bialké, H. Löwen, T. Speck

ArXiv e-prints **arXiv:1412.4601** (2014), submitted.

Abstract: We study numerically a model for active suspensions of self-propelled repulsive particles, for which a stable phase separation into a dilute and a dense phase is observed. We exploit that for non-square boxes a stable "slab" configuration is reached, in which interfaces align with the shorter box edge. Evaluating a recent proposal for an intensive active swimming pressure, we demonstrate that the excess stress within the interface separating both phases is negative. The occurrence of a negative tension together with stable phase separation is a genuine non-equilibrium effect that is rationalized in terms of a positive stiffness, the estimate of which agrees excellently with the numerical data. Our results challenge effective thermodynamic descriptions and mappings of active suspensions onto passive pair potentials with attractions.

Statement of the author: This article was written by T. Speck and me. All the numerical data in this work has been obtained and evaluated by me. The results have been interpreted and linked to one another by all authors who also cooperatively organized the outline of the article.

Abstract

In this work the phase separation of active fluids is investigated analytically and numerically. For a proper comparison with hard spheres in experiments, in particular the experiment performed by the *2. Physikalisches Institut* at the University of Stuttgart, particles interaction is modeled by the Weeks-Chandler-Andersen pair potential. The spherical particles are also assumed to be restricted to a plane while their direction of propulsion is uncorrelated. Although particles interact purely repulsive, contradictorily to systems in equilibrium, this system exhibits phase separation caused by the activity, where the steady state consists of one large dense cluster surrounded by a dilute phase.

The first chapter provides an introduction to soft active matter. The second chapter revisits theoretical basics needed for the following chapters which present the results of this dissertation.

In Chap. 3, starting from the Smoluchowski equation, a microscopic theory is derived which describes the system near homogeneity and leads to an effective swimming speed of the particles which is solely determined by a new defined quantity, the so-called force imbalance coefficient. An instability analysis predicts a threshold for the force imbalance coefficient, determining the onset of a density instability in the system. The phase separation observed in simulations is then quantified to estimate the critical velocity of the onset of the phase separation. These values do indeed correspond to a force imbalance coefficient being at the theoretically predicted boundary of the unstable region of the system. Besides a comparison to the experimental data obtained by the *2. Physikalisches Institut* at the University of Stuttgart also the robustness of the microscopic theory is shown by performing computer simulations of three further pair potentials.

In Chap. 4 the theory is extended to gain a deeper insight into the large-scale behavior of the phase separation process. Eventually, this leads to an effective free energy functional which is valid for a homogeneous non-equilibrium system at the onset of an instability. The evolution equation for the rescaled density implying the existence of such a free energy functional is recognized as the Cahn-Hilliard equation which is typically employed to study phase separation in equilibrium. For this effective Cahn-Hilliard description the spinodal is constructed and shows excellent agreement with the numerically obtained phase diagram of the non-equilibrium simulations. In addition, by analytically analyzing the evolution of the amplitude of a density fluctuation, it is shown that the hysteresis of the phase separation discovered in simulations is already qualitatively contained in the effective Cahn-Hilliard description.

In Chap. 5 the interfacial tension of the interface separating the two phases is investigated with two different concepts known from studies of equilibrium systems: via the anisotropy of the pressure at the interface and the fluctuations of the interface. Surprisingly, by taking into account the negative work spent on the solvent by the swimming particles, both results coincide excellently.

Zusammenfassung

Im Rahmen dieser Dissertationsschrift wird die Phasenseparation aktiver Fluide sowohl analytisch als auch numerisch mit Hilfe von Computersimulationen untersucht. Um eine möglichst hohe Vergleichbarkeit mit Experimenten zu erzielen, insbesondere dem Experiment am *2. Physikalischen Institut* der Universität Stuttgart, wird die Wechselwirkung zwischen Teilchen entsprechend dem Weeks-Chandler-Andersen Paarpotential modelliert. Darüber hinaus wird angenommen, dass sich Teilchen ausschließlich in zwei Dimensionen bewegen können. Trotz rein repulsiver Wechselwirkung zeigt das System, im Widerspruch zu Systemen im Gleichgewicht, makroskopische Phasenseparation welche durch den intrinsischen Antrieb der Teilchen verursacht wird.

Das erste Kapitel bietet eine Einführung in das Gebiet der aktiven weichen Materie. Im Anschluss werden im zweiten Kapitel theoretische Konzepte erläutert, welche die Grundlage für die folgenden Kapitel bilden.

Um die makroskopische Phasenseparation des aktiven Systems zu beschreiben wird zunächst in Kapitel 3, ausgehend von der Smoluchowski-Gleichung, eine mikroskopische Theorie hergeleitet welche ein homogenes System kurz vor der Phasenseparation beschreibt. Die Theorie führt auf einen Ausdruck für die effektive Schwimmgeschwindigkeit der Teilchen, welche durch einen neu definierten Parameter bestimmt wird, dem Kräfte-Ungleichgewicht-Koeffizienten. Eine Stabilitätsanalyse führt auf einen Schwellenwert für diesen Koeffizienten, sodass sich ein System mit einem höheren Wert instabil gegenüber geringen Dichtefluktuationen verhält, was letztendlich zur Phasenseparation führt. Anschließend wird mit Hilfe von Computersimulationen die kritische Geschwindigkeit für die Phasenseparation numerisch bestimmt und mit dem entsprechenden Kräfte-Ungleichgewicht-Koeffizienten verglichen, was exzellent mit der theoretischen Vorhersage übereinstimmt. Zusätzlich werden die Simulationsergebnisse mit experimentellen Ergebnissen aus dem *2. Physikalischen Institut* der Universität Stuttgart verglichen. Um die hergeleitete Theorie weiterhin zu überprüfen werden Computersimulationen mit drei weiteren Wechselwirkungsmodellen durchgeführt und mit den Vorhersagen der mikroskopischen Theorie verglichen.

In Kapitel 4 wird die Theorie erweitert um das Verhalten auf großen Skalen näher zu untersuchen. Dies führt auf ein Funktional für die effektive freie Energie des Systems im Nichtgleichgewicht, jedoch nur gültig zu Beginn der Phasenseparation. Die Differentialgleichung, die das zeitliche Verhalten der Dichte beschreibt und letztlich auf das Funktional führt, ist bekannt als Cahn-Hilliard-Gleichung und wird üblicherweise angewandt um die Phasenseparation im Gleichgewicht zu untersuchen. Ausgehend von dieser effektiven Beschreibung wird die Spinodale des Systems konstruiert und zeigt eine sehr gute Übereinstimmung mit dem numerisch bestimmten Phasendiagramm. Außerdem wird gezeigt, dass die numerisch beobachtete Hysterese bezüglich der Phasenseparation ebenfalls durch die Cahn-Hilliard-Beschreibung hergeleitet werden kann.

In Kapitel 5 wird mit Hilfe von zwei unabhängigen Methoden die Oberflächenspannung zwischen den Phasen untersucht: Über die Anisotropie des Druckes an der Phasengrenze sowie die Fluktuationen der Phasengrenze. Beachtet man darüber hinaus, dass die Teilchen aufgrund ihrer persistenten Schwimmbewegung kontinuierlich Arbeit am Dispersionsmedium verrichten, stimmen die beiden unabhängig berechneten Ergebnisse hervorragend überein.

Contents

Preface	iii
List of published work	iv
Abstract	viii
Zusammenfassung	ix
1 Introduction	1
2 Theoretical basics	7
2.1 Brownian motion	7
2.2 Langevin equation	8
2.3 Smoluchowski equation	9
2.3.1 Particles in an external potential	9
2.3.2 Interacting particles	10
2.4 Particle model	11
2.4.1 Experimental realization	11
2.4.2 Particle interaction	12
2.4.3 Propulsion mechanism	14
2.5 Brownian dynamics simulation	16
2.5.1 Reduced units and time step	17
2.6 Virial pressure	17
2.7 Phase coexistence	18
2.7.1 Line tension	19
3 Phase separation	21
3.1 Analytical description	23
3.1.1 One-particle density	23
3.1.2 Effective swimming speed	27
3.2 Linear stability analysis	28
3.2.1 Effective hydrodynamic equations	28
3.2.2 Perturbation of the homogeneous suspension	29
3.2.3 Scaling argument	31

3.2.4	Discussion	31
3.3	Numerical results	35
3.3.1	Quantifying the phase transition	35
3.3.2	Force imbalance coefficient	37
3.3.3	Long-time diffusion	38
3.3.4	Further pair potentials and reentrant behavior	38
3.3.5	Experimental results	41
3.4	Conclusion	45
4	Effective Cahn-Hilliard description	49
4.1	Effective free energy functional	52
4.1.1	Free energy coefficients	56
4.2	Phase diagram	57
4.2.1	Numerical results	57
4.2.2	Instability line construction	58
4.3	Nature of the phase transition	60
4.3.1	Numerical evidence	60
4.3.2	Bifurcation diagrams	63
4.4	Numerical coexistence curve	68
4.5	Conclusion	71
5	Interfacial tension	75
5.1	Virial route	76
5.1.1	Active pressure tensor	76
5.1.2	Mechanical pressure	77
5.1.3	Active interfacial tension	79
5.2	Fluctuation route	80
5.2.1	Derivation	81
5.2.2	Active interfacial tension	82
5.3	Housekeeping work	83
5.4	Conclusion	84
A	Appendix	85
A.1	Finite size analysis of the phase transition	85
A.2	Free energy functional	87
A.3	Lower order expansion	87
A.4	Numerical phase diagrams for different threshold choices	90
	Bibliography	91

Chapter 1

Introduction

In the ancient Greece, the philosopher Leucippus (5th century BC) and his pupil Democritus (ca. 460 BC - ca. 370 BC) developed the philosophy *atomism* which got its name from the Greek word *atomon*, i.e., uncuttable or indivisible. The philosophy states that everything is composed of small indestructible building blocks (atoms) which cooperatively form the macroscopic visible matter in the world. Nowadays, thanks to pioneering works like the publication of the periodic table in 1869 by Dmitri Mendeleev, the discovery of the electron by J. J. Thomson in 1897 [6], the evidence of a positively charged atomic nucleus by E. Rutherford in 1909 [7] and the discovery of the neutron by J. Chadwick in 1932 [8], humankind knows that matter consists of atoms which are formed by an electron cloud containing a several orders of magnitude smaller atomic nucleus built out of protons and neutrons¹.

Although everything is made of atoms, we know from our experiences in everyday life that there are rather hard materials, like gold, wood or copper, which are not easy to deform under normal conditions, i.e., room temperature. On the other hand there are easily deformable materials, like liquids, plastic, toothpaste or rubber, whose shear moduli are several orders of magnitude lower than those of hard materials. These easily deformable systems are so-called soft matter systems and are treated exclusively in this thesis. The size of the building blocks of soft matter systems fall into the mesoscopic length scale, ranging from hundreds of nanometers to a few micrometers, allowing experimental physicists to study systems via light microscopy. Usually, the building blocks (particles) are dispersed in a medium of much smaller particles, e.g., water molecules, so that the dispersion medium can be treated as a continuum. Due to the lower limit of the mesoscopic length scale quantum mechanical effects do not need to be taken into account. The upper boundary of the mesoscopic length scale ensures that the system can still be considered as soft since the total energy of the particles is comparable to the energy scale of thermal fluctuations (Brownian motion). There are two main types of sus-

¹Unlike the electron, which is an elementary particle, protons and neutrons are composed of even smaller elementary particles, so-called quarks.

pendent particles: polymers which are chains consisting of smaller subunits (monomers) and colloids which are arbitrary shaped particles like spheres, platelets or rods. Examples of soft matter in everyday life are beer foam (trapped gas pockets in liquid), hand cremes (oil-in-water emulsions), blood (platelets-like thrombocytes dispersed in a liquid) and liquid crystal displays (rod-like elongated particles ordering in a liquid due to an electric field). The huge variety of systems offers various complex observable phases, but whose description is desirable to be based on simple concepts. This breakthrough was achieved by Pierre-Gilles de Gennes, who was awarded with the Nobel prize in 1991 *"for discovering that methods developed for studying order phenomena in simple systems can be generalized to more complex forms of matter, in particular to liquid crystals and polymers"*².

The systems from everyday life mentioned above have a wide range of different components and are therefore difficult to be analyzed numerically, analytically and experimentally. Hence, physicists help themselves by employing quite simple model systems which still capture the main aspects. One famous and often mentioned example is a system of hard spheres suspended into a liquid. The spherical particles do not interact with one another, but are also not able to interpenetrate each other, just like billiard balls. This was one of the first systems studied using computer simulations [9–11] of less than a hundred particles. Also the famous experiment by Pusey and van Meegen has been performed to study the behavior of colloidal spheres made of polymethylmethacrylate (PMMA) [12]. Almost two decades later this system is still topic of soft matter research, so that experiments under the influence of microgravity in the space shuttle Columbia and Discovery have been carried out [13]. To this day, the melting scenario of the corresponding two-dimensional case of hard disks is not clear yet and highly discussed [14]. Nonetheless, on which physicist do agree is the existence of a density (entropically) driven liquid-solid phase transition being describable by an order parameter measuring the crystalline (hexagonal) structure, being showed in both computer simulations and experiments. If the hard spheres additionally repel each other, e.g., due to surface charges of equal sign, two new system parameters, the strength and range of the repulsion, influence the liquid-solid phase transition. However, whether liquid or solid, the phases are always homogeneous for a one component (monodisperse) system of pure repulsive colloids.

This observation changes as soon as sufficiently strong attractive particle interactions are introduced. The existence of such attractive interactions can arise from short ranged van der Waals forces explained by the dipole-dipole interactions between the material the particles are made of. One simple and famous concept is the Lennard-Jones potential modeling the interaction between a pair of neutral particles [15]. Several studies have shown, that particles will microscopically or macroscopically separate into dense and dilute regions within the system if attraction is strong enough [16,17]. This phenomenon is called phase separation, generally described by a certain order parameter, often the local density, which is no longer distributed homogeneously throughout the system.

²"The Nobel Prize in Physics 1991". *Nobelprize.org*. Nobel Media AB 2014. Web. 17 Nov 2014. <http://www.nobelprize.org/nobel_prizes/physics/laureates/1991/>

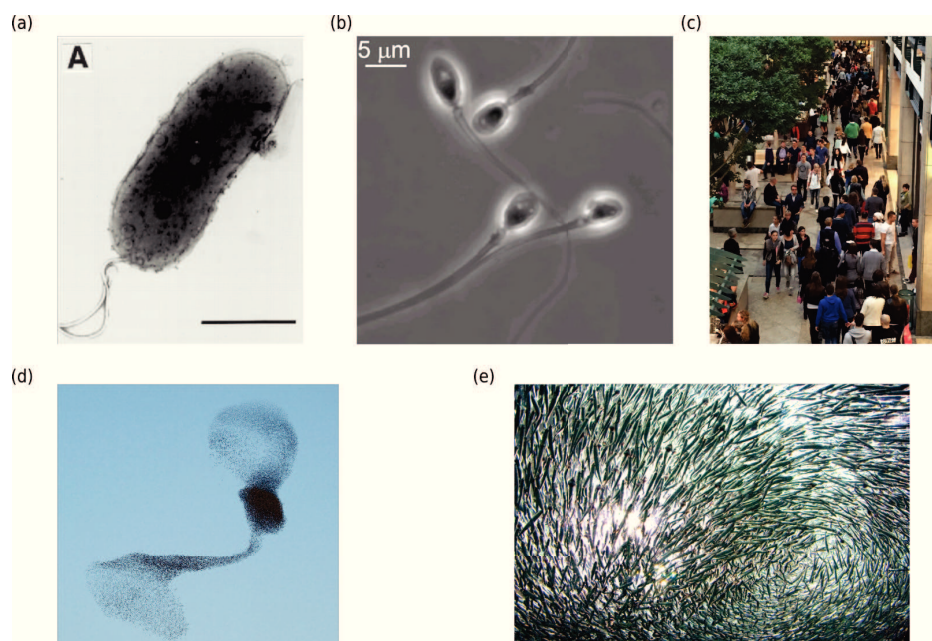


Figure 1.1: (a) Electron microscopy of the stomach bacterium *Helicobacter Pylori*, which propels itself through the stomach mucus. The bar corresponds to $1\ \mu\text{m}$. Adapted from Ref. 20. (b) Sperm sample imaged by phase contrast microscopy. Adapted from Ref. 21. (c) Pedestrians in the shopping mall *CentrO Oberhausen*, Germany. Photo taken by Rainer Freytag. (d) Flock of starlings. Picture: Flickr.com by Ed Yourdon. (e) Swarm of fish. Picture (contrast/brightness slightly changed): Flickr.com by Lance McCord. All pictures from Flickr.com have been used according to the Creative Commons license.

The properties of the interface separating those phases, i.e., the interfacial tension and stiffness [18, 19], is to this day subject of current research. An example for a phase separating system from everyday life was in principle already mentioned: a hand creme without an emulsion stabilizer would phase separate into oil-rich (water-poor) and oil-poor (water-rich) regions. In an ordinary experiment at home a water-oil mixture will always macroscopically phase separate due to gravity since common cooking oil has a lower mass density than water and will be the upper phase. In the absence of gravity and if one shakes the mixture, the oil breaks up into droplets which, if the oil concentration is low enough, do not merge and illustrates the scenario of microscopic phase separation.

So far only systems in thermodynamic equilibrium have been considered, where there is no macroscopic net flow of matter or energy within the system. Motivated through microscopic biological systems like bacteria and spermatozoa (see Fig 1.1 (a), (b)), but also macroscopic biological systems like humans, flock of birds and school of fish (see Fig 1.1 (c)-(e)), particles are considered which can intrinsically propel themselves

through the dispersion medium. The class of such suspensions of self-propelled particles is referred to as soft active matter [22]. Under certain circumstances active systems exhibit collective dynamics which are in principle already known from everyday life, like the laning of pedestrians on busy streets or the swarming behavior of birds and fishes, see Fig. 1.1(c)-(e). Again, theoretical physicists help themselves by introducing quite simple models which still capture the essential physics of the more complex systems in real life. The introduction of the Vicsek model in 1995 [23] was a pioneering work which led to a wide field of theoretical models being studied for the last twenty years. There exist approaches to theoretically describe motion of polarized animal groups [24, 25]. In experiments either actual bacteria, starlings or school of fish have been studied [26–29] or artificial particles mimicking the swimming behavior have been crafted [30–32]. Since energy is constantly pumped into the system so particles can maintain a certain velocity, active systems fall into the class of non-equilibrium systems where thermodynamical concepts, like the Helmholtz free energy or the fundamental thermodynamic relations, are not applicable a priori. Due to the relation to everyday life and the new class of non-equilibrium systems, active matter is studied extensively, leading to a wealth of new non-equilibrium phenomena like swarming, clustering and active turbulence. The propulsive motion of particles can even lead to phase separation in monodisperse systems of pure repulsive particles [2, 33, 34].

In this thesis the phase separation of self-propelled disks in two dimensions will be investigated from different perspectives. In chapter 2, theoretical concepts needed for this work are revisited where amongst others the so-called Weeks-Chandler-Anderson (WCA) model is introduced, which serves as a good approximation for hard disks due to the excellent agreement with experiments. By numerically introducing an intrinsic propulsion of the particles, one observes a phase transition from a homogeneous fluid to a phase separated system containing one dense large cluster surrounded by a dilute phase.

In the third chapter a microscopic theory is developed from first principles which describes the onset of such a phase separation and whose predictions are compared to numerical results. Furthermore, the robustness of this phenomenon is shown by investigating three further pure repulsive particle models. In addition the numerical results are compared to the experimental data of artificial light-activated swimmers in the experiment of the *2. Physikalisches Institut* at the University of Stuttgart.

In the fourth chapter the analytic theory is extended, leading to the existence of an effective free energy functional, which is normally only given for equilibrium systems. The corresponding evolution equation for the density field is recognized as the Cahn-Hilliard equation [35] and therefore maps the non-equilibrium system to an effective equilibrium system. Based on this description parts of the phase diagram are constructed and compared to numerical results as well as different phase separation scenarios are discussed both numerically and in terms of the Cahn-Hilliard description.

In the last chapter the tension of the interface between the two phases is investigated in detail. Motivated by the effective Cahn-Hilliard description of the system the validity of equilibrium methods to calculate the interfacial tension of the interface is tested. On the

one hand the interfacial tension, or stiffness, is estimated via the pressure anisotropy at the interface. On the other hand the interfacial stiffness is calculated by analyzing the fluctuations of the interface which coincides surprisingly well with the former method.

Chapter 2

Theoretical basics

2.1 Brownian motion

In 1827, Robert Brown, a scottish botanist, extracted particles from pollen of plants, suspended them into water and observed their behavior through a microscope. He noticed a vibrating, jittering-like motion of the suspended particles, which could not be caused by a living organism alone since he made the same observation for inorganic particles. In 1905, the german physicist Albert Einstein provided an analytical description for this diffusive motion [36]. He showed that the spatial and temporal evolution of the one dimensional particle density $\rho(x, t)$ of N identical independently freely moving particles suspended in a solvent obeys the diffusion equation

$$\frac{\partial \rho}{\partial t} = D_0 \frac{\partial^2 \rho}{\partial x^2}. \quad (2.1)$$

The prefactor D_0 denotes the bare diffusion coefficient of the freely moving particle with its general expression

$$D_0 = \frac{k_B T}{\lambda}, \quad (2.2)$$

where k_B is the Boltzmann constant, T is the absolute Temperature and λ is the translational friction coefficient of the particle in the solvent. Under the initial condition $\rho(x, t = 0) = N\delta(x)$, where $\delta(x)$ is the Dirac delta function, the solution of Eq. (2.1) is given by the Gaussian form

$$\rho(x, t) = \frac{N}{\sqrt{4\pi D_0 t}} e^{-\frac{x^2}{4D_0 t}}. \quad (2.3)$$

The first moment of this Gaussian distribution, which corresponds to the mean particle position, is zero. The second moment, i.e., the mean squared displacement of particles with respect to their initial position $x(t = 0)$, is given by

$$\langle (x(t) - x(0))^2 \rangle = 2D_0 t. \quad (2.4)$$

Consequently, diffusion is described as a Gaussian stochastic process and is easily applicable to d spatial dimensions due to the uncorrelated movement in each dimension, giving

$$\langle \mathbf{r}(t) \rangle = 0, \quad (2.5)$$

$$\langle (\mathbf{r}(t) - \mathbf{r}(0))^2 \rangle = 2dD_0t. \quad (2.6)$$

Throughout this work the ergodicity hypothesis is applied so that $\langle \cdot \rangle$ denotes both the time and ensemble average.

2.2 Langevin equation

In 1908, Paul Langevin, a french physicist, introduced the picture of a random force $\mathbf{f}^{(r)}(t)$ acting on the suspended particles, see Ref. 37 for a translation of his work. This stochastic force models the coupling between the suspended particles and the solvent molecules and is comparable to the so-called random walk [38, 39]. The physical picture is that the solvent molecules are much faster than the larger suspended particle. One simple example is a sphere of $1 \mu m$ radius being suspended into water at $20^\circ C$. The H_2O molecules can be approximated with a diameter of $d_{H_2O} = 2.75 \cdot 10^{-10} m$ and have a self-diffusion coefficient of about $D_s = 2.025 \cdot 10^{-9} m^2/s$ [40], which is normalized to the molecules diameter $D_s/d_{H_2O}^2 \simeq 2.67 \cdot 10^{10} s^{-1}$. This is 12 orders of magnitude larger than the diffusion coefficient of the suspended sphere normalized to its diameter and implies that the collision frequency between solvent molecules and the suspended sphere is so high, that time scales can be separated. Since one is interested in the time scale of the suspended particles, the solvent is treated as a continuum which randomly *kicks* against the suspended particle at a very high frequency. Of course this phenomenological derivation only works for particles which are sufficiently larger than the solvent molecules. The equation of motion for particle i under that random force is written as

$$m\ddot{\mathbf{x}}_i = -\lambda\dot{\mathbf{x}}_i + \mathbf{f}_i^{(r)}(t). \quad (2.7)$$

For a correct description of the diffusion process, it was found [41] that the stochastic force obeys

$$\langle \mathbf{f}_i^{(r)}(t) \rangle = 0 \quad (2.8)$$

$$\langle \mathbf{f}_i^{(r)}(t) \mathbf{f}_j^{\text{tr},(r)}(t') \rangle = 2k_B T \lambda \mathbb{1} \delta(t - t') \delta_{ij}, \quad (2.9)$$

where the superscript tr denotes the vector transpose, $\delta(\cdot)$ is the Dirac delta function and δ_{ij} is the Kronecker-Delta, indicating a temporal and spatial uncorrelated random force. Throughout this work only colloidal suspensions are considered which consist of suspended particles with their typical size being in the mesoscopic length scale ranging from hundreds of nm to several μm . The ratio between inertial forces and viscous forces in a suspension is characterized by the Reynolds number

$$Re = \frac{\rho_s \tilde{v} l}{\eta}, \quad (2.10)$$

where \tilde{v} is the typical relative velocity to the solvent (thermal velocity), l denotes the typical length scale traveled (size of the particle), ρ_s is the mass density of the solvent and η represents the dynamic viscosity of the solvent. An example for a realistic colloidal system would be a set of particles being suspended into water at room temperature, yielding $Re \ll 1$, which is equivalent to a strong dominance of viscous forces. In that case the inertia term in Eq. (2.7) can be neglected, i.e., $m\ddot{\mathbf{r}}_i \ll \lambda\dot{\mathbf{r}}_i$, and the Langevin equation is reduced to the overdamped case

$$\lambda\dot{\mathbf{r}}_i = \mathbf{f}_i^{(r)}(t). \quad (2.11)$$

Starting from Eq. (2.11) one can easily derive in d spatial dimensions

$$\langle \mathbf{r}(t) \rangle = 0 \quad (2.12)$$

$$\langle (\mathbf{r}(t) - \mathbf{r}(0))^2 \rangle = 2dD_0t, \quad (2.13)$$

which is the exact result given by the Einstein description in Sec. 2.1. If particles are under the influence of an external potential $V(\mathbf{r}, t)$, e.g., gravity, the Langevin Eq. (2.11) needs to be modified to

$$\lambda\dot{\mathbf{r}}_i = -\nabla V(\mathbf{r}, t) + \mathbf{f}_i^{(r)}(t), \quad (2.14)$$

where ∇ is the nabla operator. The aspect of particles interacting with one another will be discussed in the following.

2.3 Smoluchowski equation

2.3.1 Particles in an external potential

In this section, the derivation of the Smoluchowski equation is shown, which can also be followed in Ref. 42. For free particles, Fick's first law [43] yields

$$\mathbf{j} = -D_0\nabla\rho, \quad (2.15)$$

where \mathbf{j} is the particle flux. The second law of Fick is a combination of the first one and the continuity equation

$$\frac{\partial\rho}{\partial t} = -\nabla\mathbf{j}, \quad (2.16)$$

leading to the diffusion equation (2.1) derived by Einstein (if $\nabla D_0 = 0$ which is assumed throughout the whole work). However, particles in an external potential $V(\mathbf{r}, t)$ experience an additional velocity drift $-\nabla V/\lambda$ and Fick's first law changes to

$$\mathbf{j} = -D_0\nabla\rho - \rho\frac{1}{\lambda}\nabla V. \quad (2.17)$$

By linking Eq. (2.16) and Eq. (2.17) one gets

$$\partial_t\rho = \mu_0k_B T\Delta\rho + \mu_0\nabla(\rho\nabla V), \quad (2.18)$$

where $\Delta = \nabla^2$ is the Laplace operator, $\mu_0 = 1/\lambda$ the mobility of a free particle and the notation $\partial^{(n)}/\partial x^{(n)} \equiv \partial_x^{(n)}$ is introduced. Since particles are not interacting one can go back to the probability density function $\Psi(\mathbf{r}, t)$ of one particle, where $\Psi(\mathbf{r}, t)d\mathbf{r}$ is the probability to find the particle at time t within the volume element $d\mathbf{r}$ centered around its position \mathbf{r} . Scaling this for N non-interacting particles yields the relation

$$\rho(\mathbf{r}, t) = N\Psi(\mathbf{r}, t). \quad (2.19)$$

Plugging this result into Eq. (2.18) leads to the Smoluchowski equation of non-interacting particles in an external potential

$$\partial_t \Psi = \mu_0 [k_B T \Delta \Psi + \nabla(\Psi \nabla V)], \quad (2.20)$$

which is sometimes also mistakenly referred to as the Fokker-Planck equation, a rather general description for the temporal evolution of a probability function.

2.3.2 Interacting particles

For N interacting particles the Smoluchowski equation needs to be adjusted. It is clear, that the probability function does now also depend on the set of the particles degrees of freedom. For particle interactions solely depending on the particle positions, this is written as $\{\mathbf{r}_i\} \equiv \{\mathbf{r}_1, \dots, \mathbf{r}_N\}$, giving $\Psi = \Psi(\{\mathbf{r}_i\}, t)$, which is now the joint probability density function of finding a system at a certain particle configuration at time t . Besides the interaction between particles, which is usually modeled via a pairwise particle potential, one also needs to take care of hydrodynamic effects, since the movement of a particle creates a flow field around itself, which may have an influence on other particles in the suspension. Assuming conservative forces, the total force acting on a particle j can be written as

$$\mathbf{F}_j = -\nabla_j U(\{\mathbf{r}_i\}, t), \quad (2.21)$$

where $U(\{\mathbf{r}_i\}, t)$ is the total potential energy including both particle interactions and external forces, and ∇_j denotes the gradient with respect to \mathbf{r}_j . This force acting on the particle j leads to a motion and consequently induces a flow of the solvent, which may move another particle i . This hydrodynamic effect is generally included by a linear coupling between the forces acting on all particles (labeled by the index j) and the actual velocity of particle i , i.e.,

$$\mathbf{v}_i = \sum_{j=1}^N L_{ij}(\{\mathbf{r}_i\}) \mathbf{F}_j = -\sum_{j=1}^N L_{ij}(\{\mathbf{r}_i\}) \nabla_j U. \quad (2.22)$$

One should note, that the sum does also include the index i which corresponds to the hydrodynamic friction of the particle itself. The coefficients L_{ij} are the entries of the symmetric positive definite mobility matrix, which determines the particle mobility due to the spatial configuration. It also includes the effect of the particle itself, i.e., the

scalar mobility of a free particle $L_{ii} = \mu_0$. Consequently, the scalar free mobility μ_0 in the previous equations needs to be replaced by the concept of the mobility matrix. Thus the total flux is now given by the sum of each single particle flux and reads

$$\mathbf{j} = - \sum_{i=1}^N \left[\sum_{j=1}^N k_B T L_{ij} \nabla_j \rho - \rho \left(\sum_{j=1}^N L_{ij} \nabla_j U \right) \right]. \quad (2.23)$$

The quantity ρ is referred to as the one-particle density since it is connected to the probability density of finding any particle, arbitrary labeled as 1, at a volume $d\mathbf{r}_1$ centered around \mathbf{r}_1 at time t . Accordingly, the two-particle density is connected to the joint probability density function of finding one arbitrary particle at position \mathbf{r}_1 under the condition that another arbitrary particle is at position \mathbf{r}_2 , both at the same time t . This relation can be generalized by the n -particle density

$$\rho_n(\mathbf{r}_1, \dots, \mathbf{r}_n) = \frac{N!}{(N-n)!} \int d\mathbf{r}_{n+1} \dots d\mathbf{r}_N \Psi \quad (2.24)$$

with $N!/(N-n)!$ being a combinatorial factor arising from the number of possibilities of successively picking n particles out of an ensemble of N indistinguishable particles. Combining the continuity equation (2.16) with Eq. (2.23) one gets the Smoluchowski equation for interacting particles

$$\partial_t \Psi = \sum_{i,j=1}^N \nabla_i L_{ij} [k_B T \nabla_j \Psi + (\nabla_j U) \Psi], \quad (2.25)$$

where $i, j = 1$ is the notation for a double sum over indices i and j . This expression describes the diffusion of the joint probability density function $\Psi(\{\mathbf{r}_i\}, t)$ in phase space including the drift velocities in phase space due to the total force acting on the particles.

2.4 Particle model

In this section, the model for the self-propelled particles considered in this work is introduced. The goal of the particle model is to be as simple as possible, but yet being able to capture the essential phenomena observed in experiments of self-propelled spheres in a quasi two-dimensional setup [1, 44, 45]. In particular the experiment in Ref. 1 served as reference, i.e., a pair potential had to be found so that the equilibrium structure obtained in the experiment coincides with results from computer simulations. A brief description of the concept of Brownian dynamics computer simulations will be given later in Sec. 2.5.

2.4.1 Experimental realization

Here, the experiment of Ref. 1 is presented briefly, while the author stresses that the experiment has been performed by the research group of *C. Bechinger* at the University of Stuttgart (*2. Physikalisches Institut*). The main experimental work was done

by *I. Buttinoni*. There are also other publications, which classify this novel technique of self-propelled light-activated particles in detail [31, 46]. In case of the experiment in Ref. 1, the suspension consists of so-called Janus particles, which in general are colloids consisting of two surfaces with different physical properties, which is the reason these particles are named after the roman god Janus of beginnings and transitions who was illustrated with two faces. In this particular experiment, spherical particles are prepared from SiO_2 beads with radius $R \simeq 2.13 \mu m$ where one hemisphere is coated with graphite. In principle the particles could have been coated with any other sufficient light absorbing material, e.g., gold, but graphite has been used to minimize attractive forces, i.e., van-der-Waals forces, also called Hamaker forces. The particles are suspended into a water-2,6-lutidine mixture (28 mass% lutidine), which is homogeneous below its critical temperature of approximately $34^\circ C$. The experiments have been performed in a $400 \mu m \times 400 \mu m$ cavity with a height of about $6 \mu m$, so that particle motion can be considered as quasi two dimensional, while particles are able to rotate in three dimensions. The experiments have been performed at room temperature where the solvent is homogeneous, so that the system is at equilibrium and can generally be described with the Smoluchowski Eq. (2.25). If the suspension is illuminated by a widened laser beam of wavelength $532 nm$ particles start to move and the system is constantly driven out of equilibrium. The underlying mechanism is diffusiophoresis, caused by the absorbed light at the graphite side of the sphere, so that the solvent is locally heated above the critical temperature at one side of the particle. Therefore water and lutidine start to separate, leading to a density gradient around the particle, which causes the sphere to move along its symmetry axis and successfully mimics a self-propelled particle.

2.4.2 Particle interaction

Motivated through this experimental setup the simplest possible particle model considers N spheres at constant temperature T with all particle centers being restricted to the same plane, which means particles are theoretically modeled as self-propelled disks in the xy -plane. In addition, for the sake of simplicity, hydrodynamic interactions are neglected, leading to a very simple expression for the mobility matrix entries $L_{ij} = \mu_0 \delta_{ij}$. Furthermore a possible polydispersity is neglected, i.e., all spheres are modeled with a mutual radius R , so that their translational friction coefficient at small Reynolds number is given by the Stokes' law

$$\mu_0^{-1} = \lambda = 6\pi\eta R. \quad (2.26)$$

At first, the Smoluchowski equation reduces to

$$\partial_t \Psi = \sum_{i=1}^N \mu_0 \nabla_i [k_B T \nabla_i + \nabla_i U] \Psi. \quad (2.27)$$

Essential is, that one can demonstrate that this expression is equivalent to the overdamped Langevin equation [41]

$$\lambda \dot{\mathbf{r}}_i = -\nabla_i U(\{\mathbf{r}_i\}, t) + \mathbf{f}_i^{(r)}(t), \quad (2.28)$$

where in comparison to Eq. (2.14) the external potential V has been replaced by the total potential U . The interaction between particles is modeled by an isotropic pairwise potential $u(r_{ij})$, which only depends on the interparticle distance $r_{ij} \equiv |\mathbf{r}_{ij}|$ with $\mathbf{r}_{ij} \equiv \mathbf{r}_j - \mathbf{r}_i$. For a proper comparison with the experiment in Ref. 1, the experimentalist *I. Buttinoni* has measured the pair correlation function

$$g(r) = \frac{1}{N\rho} \sum_{\substack{i,j=1 \\ i \neq j}} \delta(\mathbf{r} - (\mathbf{r}_i - \mathbf{r}_j)) \quad (2.29)$$

in an equilibrated passive suspension. By projecting the particle position on the plane perpendicular to the direction gravity is acting, the area packing fraction has been approximated to $\phi = N\pi R^2/A \simeq 0.37$, where N is the total number of particles in the monitored area A . In order to do the same in simulations and compare numerical and experimental results, one first needs to think of a suitable pair potential. Since the suspension is confined in a cell with an approximate height of $6 \mu m$, spheres are not fully restricted to two dimensions and, when approaching each other, they might move in z -direction. That effect might not be so much pronounced if there is enough space for both, i.e., if the interparticle distance $r_{ij} > 2R$. Projecting this behavior onto the xy -plane leads to the picture of disks which are able to overlap a bit, but try to prevent such an event, i.e., repel each other if an overlap occurs. In addition, one could claim that particles may attract each other due to van-der-Waals forces exerted by the material of the particles. These two properties can be achieved by employing the following potential

$$u(r) = \begin{cases} \epsilon u_{LJ}(r) + u_{LJ}(2R)(\lambda_a - \epsilon) & (r \leq 2R) \\ \lambda_a u_{LJ}(r) & (r > 2R), \end{cases} \quad (2.30)$$

where the expression

$$\epsilon u_{LJ}(r) = 4\epsilon \left[\left(\frac{\sigma}{r} \right)^{12} - \left(\frac{\sigma}{r} \right)^6 \right] \quad (2.31)$$

is the Lennard-Jones potential [15, 47]. Here, the parameter λ_a is the strength of the attraction, i.e., the depth of the attractive part of the potential ($r > 2R$). For distances $r \leq 2R$ the potential always exhibits a repulsive core, namely the WCA (Weeks-Chandler-Andersen) potential [48]. The parameters $\epsilon = 100k_B T$ and $\sigma/(2R) = 2^{-1/6} \simeq 0.891$ have been fixed throughout the whole work. Fig. 2.1 shows the corresponding pair potentials for a pure repulsive ($\lambda_a = 0$) and a slightly attractive system ($\lambda_a = 0.5k_B T$) and the comparison with the experimental data. Apparently, the pair potential with the slightly attractive tail of depth $\lambda_a = 0.5k_B T$ shows somewhat better agreement with the experimental data for small distances than the pure repulsive potential. Nonetheless throughout this work only the WCA potential ($\lambda_a = 0$) has been used to show that the observed phenomena do not arise from attractive pair interactions, but are an effect solely induced by the activity of the system.

Since particles are restricted to the xy -plane, gravity, which is considered to act perpendicular to this plane, is irrelevant. Other possible external forces like interaction between

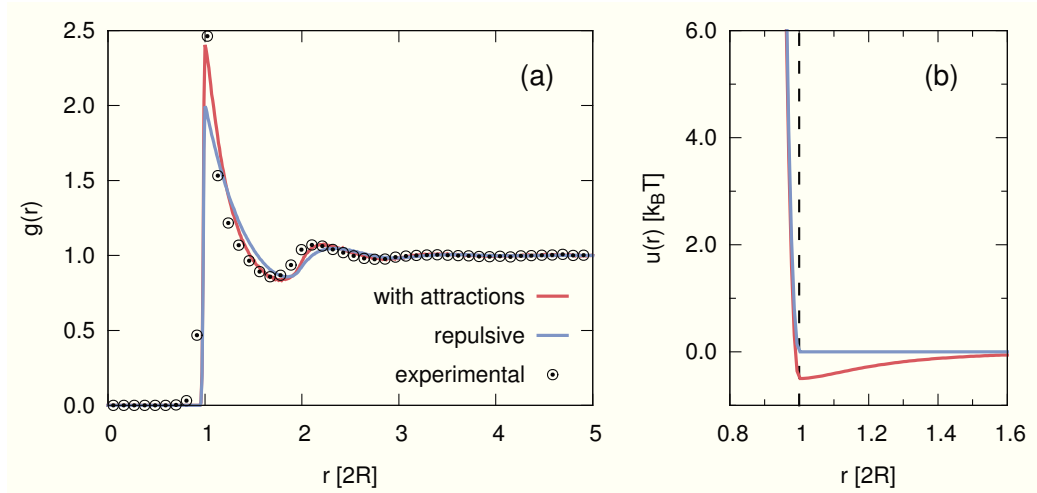


Figure 2.1: (a) Pair correlation function $g(r)$ at packing fraction $\phi = 0.37$ for the experiment (circles) and simulations considering the pair potential given by Eq. (2.30) with $\lambda_a = 0$ (blue) and $\lambda_a = 0.5k_B T$ (red). (b) Pair potentials according to $\lambda_a = 0$ (blue) and $\lambda_a = 0.5k_B T$ (red).

particles and the cell walls are neglected as well, giving the total potential energy which solely depends on the spatial configuration, i.e.,

$$U(\{\mathbf{r}_i\}) = \sum_{i=1}^N \sum_{j>i}^N u(|\mathbf{r}_{ij}|). \quad (2.32)$$

2.4.3 Propulsion mechanism

The propulsion of particles is also modeled as simple as possible, so the possibility of the particles to rotate in three dimensions has been neglected intentionally to achieve the most minimalistic model. In addition it is desirable to show that the observed phenomena in the experiment are not an effect of the quasi-two dimensional setup. Hence each particle is assigned an orientational vector, which is restricted to the xy -plane and is written as

$$\mathbf{e} = \begin{pmatrix} \cos\varphi \\ \sin\varphi \end{pmatrix}, \quad (2.33)$$

where φ is the angle enclosed between the vector \mathbf{e} and the x -axis. Each particle possesses the same constant intrinsic velocity v_0 propelling itself into the direction of its orientational vector. The orientation of each particle undergoes free diffusion with rotational diffusion coefficient D_r according to

$$\langle \dot{\varphi}_i(t) \rangle = 0 \quad (2.34)$$

$$\langle \dot{\varphi}_i(t) \dot{\varphi}_j(t') \rangle = 2D_r \delta(t - t') \delta_{ij}. \quad (2.35)$$

In consistency with real systems, the rotational diffusion is hydrodynamically coupled to the translational diffusion, yielding the Stokes-Einstein-Debye relation [49, 50]

$$\frac{D_0}{D_r} = \frac{4}{3}R^2. \quad (2.36)$$

Finally, the overdamped Langevin equation of the particle model of this work is

$$\dot{\mathbf{r}}_i = \mu_0[-\nabla_i U + \mathbf{f}_i^{(r)}(t)] + v_0 \mathbf{e}_i. \quad (2.37)$$

In Ref. 46 it is shown, that the experimental data is in accordance with this model of active Brownian motion.

According to Eq. (2.37) the Smoluchowski description needs to be extended to the model of self-propelled disks. The first step is that the joint probability density function now depends also on the set of particle orientations due to the additional degree of freedom, i.e., $\Psi = \Psi(\{\mathbf{r}_i\}, \{\varphi_i\}, t)$. Since the orientation does not depend on the spatial configuration, the joint probability density function $\Psi(\{\mathbf{r}_i\}, \{\varphi_i\}, t)$ may also be written as the product of the spatial and orientational probability density at time t , i.e.,

$$\Psi(\{\mathbf{r}_i\}, \{\varphi_i\}, t) = \Psi_r(\{\mathbf{r}_i\}, t)\Psi_\varphi(\{\varphi_i\}, t), \quad (2.38)$$

where Ψ_r and Ψ_φ are the spatial and orientational joint probability density functions respectively. By including the velocity drift $v_0 \mathbf{e}_i$ arising from the propulsion of particle i the evolution of the spatial part is written as

$$\partial_t \Psi_r = \sum_{i=1}^N \mu_0 \nabla_i [k_B T \nabla_i + \nabla_i U - \mu_0^{-1} v_0 \mathbf{e}_i] \Psi_r. \quad (2.39)$$

Since the particle model lacks any interaction between the particle orientations the orientational joint probability density function follows

$$\partial_t \Psi_\varphi = \sum_{i=1}^N D_r \partial_{\varphi_i}^2 \Psi_\varphi, \quad (2.40)$$

which is a pure diffusive behavior. Furthermore

$$\partial_t \Psi = \Psi_r \partial_t \Psi_\varphi + \Psi_\varphi \partial_t \Psi_r \quad (2.41)$$

leads to

$$\partial_t \Psi = \Psi_r \sum_{i=1}^N D_r \partial_{\varphi_i}^2 \Psi_\varphi + \Psi_\varphi \sum_{i=1}^N \mu_0 \nabla_i [k_B T \nabla_i + \nabla_i U - \mu_0^{-1} v_0 \mathbf{e}_i] \Psi_r \quad (2.42)$$

$$= \sum_{i=1}^N D_r \partial_{\varphi_i}^2 \Psi_\varphi \Psi_r + \sum_{i=1}^N \mu_0 \nabla_i [k_B T \nabla_i + \nabla_i U - \mu_0^{-1} v_0 \mathbf{e}_i] \Psi_r \Psi_\varphi \quad (2.43)$$

$$= \sum_{i=1}^N D_r \partial_{\varphi_i}^2 \Psi + \sum_{i=1}^N \mu_0 \nabla_i [k_B T \nabla_i + \nabla_i U - \mu_0^{-1} v_0 \mathbf{e}_i] \Psi, \quad (2.44)$$

which is the Smoluchowski equation of this particle model and is equivalent to the description given by Eq. (2.37).

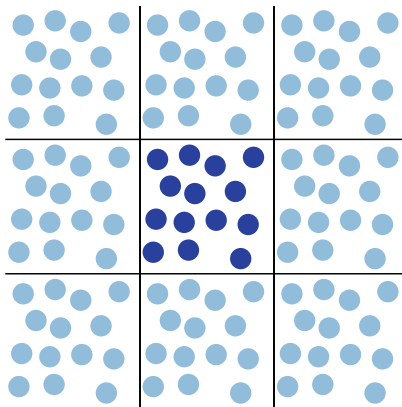


Figure 2.2: Sketch of the employed periodic boundary conditions. Particles represented by a dark blue circle are in the actual simulation box (middle), while light blue circles correspond to copies of the particles to approximate an infinite system.

2.5 Brownian dynamics simulation

This section shortly presents the simulation technique used throughout the whole work. The idea behind the algorithm of Brownian dynamics simulations is to use the Langevin Eq. (2.37) with a single realization of the stochastic force for each time step [51, 52]. By integrating the equation of motion with a finite time step Δt , one assumes that this time step is sufficiently small to consider the force $-\nabla_i U$ acting on particle i to be constant during the time interval $[t, t + \Delta t]$. Consequently, the algorithm is given by

$$\mathbf{r}_i(t + \Delta t) = \mathbf{r}_i(t) + \Delta t[-\mu_0 \nabla_i U + v_0 \mathbf{e}_i] + \Delta \mathbf{r}_G. \quad (2.45)$$

Instead of the Gaussian force $\mathbf{f}^{(r)}(t)$, the algorithm contains a Gaussian displacement vector $\Delta \mathbf{r}_G$, where, in accordance with the stochastic properties of $\mathbf{f}^{(r)}(t)$, in each time step each component is chosen from a Gaussian distribution with zero mean and variance $2D_0 \Delta t$. The technical realization of the Gaussian distributed numbers has been implemented using the Box-Muller algorithm given in Refs. 53, 54, which generates two Gaussian distributed numbers in each run. The short time dynamics of Eq. (2.45) is diffusive with the diffusion coefficient D_0 of a free particle. Due to particle interactions and the propulsion of particles this is not the case for long times. In general for d spatial dimensions one can define a long time diffusion coefficient

$$D = \lim_{t \rightarrow \infty} \frac{1}{2d} \frac{d}{dt} \langle [\mathbf{r}(t) - \mathbf{r}(0)]^2 \rangle. \quad (2.46)$$

In order to approximate an infinite system periodic boundary conditions have been employed by duplicating the actual simulation box of size $L_x \times L_y$ in all spatial directions (see Fig. 2.2). The packing fraction of the system is given by $\phi = N\pi R^2 / (L_x L_y) = \rho\pi R^2$.

2.5.1 Reduced units and time step

For more general results physical quantities, if not stated otherwise (only the case in Sec. 3.3.4), are normalized to typical units of the system: energy is given in units of the thermal energy $k_B T$ and length is measured in units of the particle diameter $2R$. The unit of time is the typical Brownian time $\tau_B = (2R)^2/D_0$ which corresponds to the time a free particle needs to achieve a mean squared displacement of $(2R)^2$, often illustrated as the time the free particle needs to explore an area of size $(2R)^2$. In these units the reduced propelling speed of a system is equivalent to the Péclet number

$$\text{Pe} = \frac{2Rv_0}{D_0}, \quad (2.47)$$

which characterizes the ratio of the rate of advection due to activity and the rate of diffusion due to thermal motion. If not mentioned explicitly, all simulations have been carried out with a time step $\Delta t = 10^{-5}\tau_B$ if $Pe < 120$ and $\Delta t/2$ for $Pe \geq 120$.

2.6 Virial pressure

The pressure of a three dimensional system is known as the ratio of force per unit area, like the force which enclosed gas atoms exert on the walls of the container. In this work solely two dimensional systems are treated, hence the pressure is force per unit length. In order to extract the pressure out of particle resolved computer simulations one calculates the virial pressure [51]

$$p = \frac{N}{\Omega_d} k_B T + \frac{1}{d\Omega_d} \sum_{i=1}^N \langle \mathbf{r}_i \mathbf{f}_i \rangle \quad (2.48)$$

with \mathbf{f}_i being the force acting on particle i and Ω_d the space in d spatial dimensions. In the following, according to the systems considered in this work, these values are fixed to $d = 2$ and $\Omega_d = A$ where $A = L_x L_y$ is the area of the simulation box. Restricting Eq. (2.48) to pairwise interparticle forces one can derive

$$p = \bar{\rho} k_B T + \frac{1}{2A} \sum_{i=1}^N \sum_{j>i}^N \langle \mathbf{r}_{ij} \mathbf{f}_{ij} \rangle \quad (2.49)$$

with the global surface density $\bar{\rho} = N/A$, the connection vector $\mathbf{r}_{ij} = \mathbf{r}_j - \mathbf{r}_i$ and the force \mathbf{f}_{ij} acting on particle j due to the presence of particle i . One can also consider the pressure tensor

$$\bar{\bar{p}} = \bar{\bar{p}}_{id} + \bar{\bar{p}}^{(i)} \quad (2.50)$$

with the pressure tensor \bar{p}_{id} known from the corresponding ideal gas and the part $\bar{p}^{(i)}$ due to particle interactions. These tensors are written as

$$\bar{p}_{id} = \bar{\rho}k_B T[\mathbf{e}_x \otimes \mathbf{e}_y], \quad (2.51)$$

$$\bar{p}^{(i)} = \frac{1}{A} \sum_{i=1}^N \sum_{j>i}^N \langle \mathbf{r}_{ij} \otimes \mathbf{f}_{ij} \rangle, \quad (2.52)$$

where \otimes is the dyadic product or also called outer product. The scalar pressure given by Eq. (2.49) is then obtained by the average of the diagonal elements

$$p = \frac{1}{2} \text{Tr}(\bar{p}) \quad (2.53)$$

with $\text{Tr}(\bar{p})$ being the trace of the 2×2 matrix representing the tensor \bar{p} . This allows to regard the directional pressure arising from diagonal terms

$$p_{xx} = \bar{\rho}k_B T + \frac{1}{A} \sum_{i=1}^N \sum_{j>i}^N \langle x_{ij} f_{x,ij} \rangle, \quad (2.54)$$

$$p_{yy} = \bar{\rho}k_B T + \frac{1}{A} \sum_{i=1}^N \sum_{j>i}^N \langle y_{ij} f_{y,ij} \rangle, \quad (2.55)$$

where $\mathbf{r}_{ij} = (x_{ij}, y_{ij})$ and $\mathbf{f}_{ij} = (f_{x,ij}, f_{y,ij})$. These expressions only describe the pressure components originated from a force acting on a line segment perpendicular to the force and do not care about pressure arising from a shear stress like p_{xy} . In the bulk of a phase, i.e., far away from any influences like enclosing walls or interfaces, the shear stresses vanish and the pressure is isotropic leading to $p_{xx} = p_{yy}$.

2.7 Phase coexistence

If systems consist of two phases, like liquid water and vapor in a closed container, one speaks of phase coexistence. The stable coexistence of two phases A and B in thermodynamic equilibrium requires equal temperatures

$$T_A = T_B \quad (2.56)$$

and mechanical equilibrium normal to the separating surface (interface)

$$P_{A,N} = P_{B,N} \quad (2.57)$$

since the forces normal to the contact surface must cancel out each other for the interface to be stable. In the bulk, sufficiently far away from the interface, the pressure has to be isotropic again, leading to the bulk pressure relation

$$P_A = P_B. \quad (2.58)$$

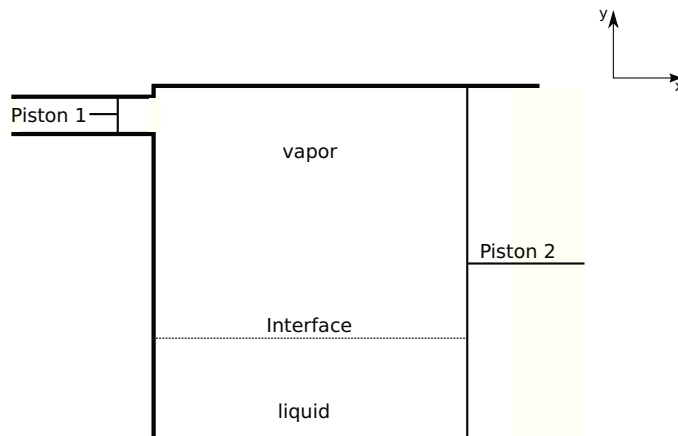


Figure 2.3: Thought experiment adapted from Ref. 55. The system consists of a vapor and liquid phase. There exists an opening at the vapor phase with piston 1 being located far away from the interface. The piston 2 expanding through both phases is movable so that both pistons can be moved simultaneously such that the total volume/area of the system does not change.

Since the chemical potential $\mu(p, T)$ is a function of pressure and temperature one gets the condition

$$\mu_A = \mu_B \quad (2.59)$$

where the chemical potential is given through the free Helmholtz energy F as $\mu = \partial F / \partial N$ at constant temperature and volume, see also introduction of Chap. 4.

2.7.1 Line tension

For a further insight into the properties of the interface separating two phases the thought experiment mentioned in Ref. 55 is applied to two dimensions, see Fig. 2.3. The piston 1 is considered to be located far away from the interface such that the pressure acting on it is equal to the isotropic pressure p . Now, the reversible process is considered where both pistons are moved simultaneously while the total area A of the system remains unchanged. The total work done contains two contributions, each from every piston,

$$dW = -pdA + dx \int p_T(y)dy. \quad (2.60)$$

The second term in Eq. (2.60) is given by piston 2 where the inhomogeneous density along the y -direction implies the pressure p_T tangential to the interface which also depends on the position y , i.e., the distance to the interface. By applying $dA = l_y dx = \int dy dx$ the upper Eq. (2.60) is rewritten as

$$dW = -dx \int [p - p_T(y)]dy. \quad (2.61)$$

For a system at thermodynamic equilibrium and constant temperature, volume and number of molecules, the total work done is equal to the change of free Helmholtz energy $dF = -dW$, which is also connected to the line tension γ via $dF = \gamma dx$. Substituting Eq. (2.61) into this relation one obtains

$$\gamma = \int [p - p_T(y)] dy \quad (2.62)$$

which quantifies the energy needed to create an interface of unity length for a system at thermodynamic equilibrium.

Chapter 3

Phase separation

In the past decades the phenomena of self-propelled particles have gained enormous interest in the field of soft matter. There have been studies on the single particle level [56–60] as well as experimental and theoretical work on the rich collective behavior of systems of interacting self-propelled particles. In the early stages, motivated from biological systems of colonies of elongated bacteria [29, 61, 62], suspensions of active rod-like particles have been studied in experiments with artificial swimmers [63–65]. The several driving mechanisms of those artificial active particles are based on chemical reactions, chemical gradients, diffusiophoresis, gravitation, thermophoresis, magnetic or electric fields [30, 66–70] and have also been analyzed theoretically [71–76]. Due to the effective alignment of rod-like particles, see Fig. 3.1(a), active systems provide a broad spectrum of collective behavior such as laning, swarming, clustering, swirling, active turbulence and phase separation [77–88] which has also been shown for systems containing an artificial alignment of particles [23, 89–96]. In addition other types of asymmetric particles have been studied, resulting in a wide variety of collective dynamics [97–100] but also

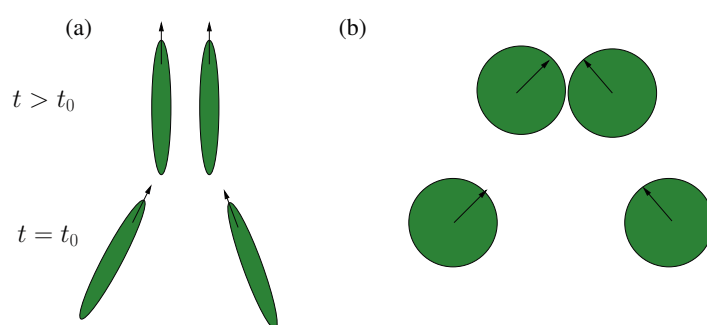


Figure 3.1: Illustration of (a) the effective alignment of rod-like particles and (b) the uncorrelated motion of spherical particles due to isotropic interaction. The lower configuration is before the collision while the upper one is after the particles collided. The arrows indicate the swimming direction.

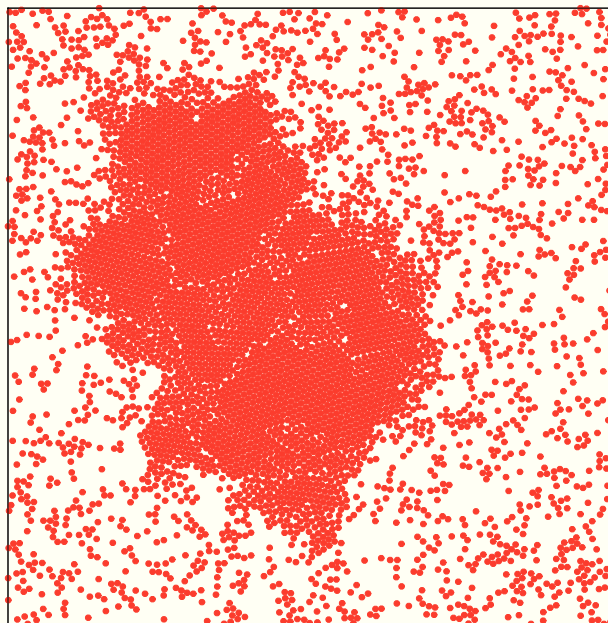


Figure 3.2: Simulation snapshot of a phase separated system containing $N = 4900$ spherical particles at area packing fraction $\phi = 0.4$ and Péclet number $Pe = 80$. Particles do interact with one another according to the model introduced in Sec. 2.4. The circles are just an approximate sketch of the particles to illustrate the phase separation and do not correspond to the actual size.

surprising results on the single particle level [101]. Besides different mixtures [102, 103] also the structural and transport properties of confined active suspensions, or more general swimmers in the presence of obstacles, have been studied not only for self-propelled rods [104–108] and ellipsoidal particles [109, 110], but also for active spherical particles [46, 111–124]. Even deformable self-propelled particles have been discussed in detail [125–130].

However, the study of active spherical rigid particles have attracted a lot of attention of several research groups due to the equilibrium analog of hard spheres and the fact that in case of negligible hydrodynamic interactions the propelling direction of spherical particles is uncorrelated and not determined by anisotropic volume exclusion or other alignment mechanisms, see Fig. 3.1(b). In analogy to active rods, non biological spherical swimmers have been crafted [45, 69, 131], but also novel types of light-activated swimmers, briefly introduced in Sec. 2.4.1, have been developed [31, 32, 44, 46]. Although lacking any orientational interactions, these systems do also exhibit collective behavior like clustering and phase separation, cf. Fig. 3.2, in both experiments [1, 44, 45] and theoretical works [2, 33, 34, 132–141, 141–144]. Also the influence on the freezing and glass transition due to activity has been studied [145–149].

This section discusses the phase separation of such swimmers without alignment mechanism and is based on publications 1 and 2. An analytical description for the particle

model introduced in Sec. 2.4 is derived from first principles, where an equation of motion for the one-particle density is found. In addition the description yields an effective swimming speed where the slowdown due to nearby particles is absorbed into one single parameter, the so-called force imbalance coefficient, which depends on the pair potential employed and the anisotropic pair correlation function. Furthermore the effective hydrodynamic equations for the density and orientational field are derived. Subsequently, a linear stability analysis is performed, leading to a prediction for the system to become unstable for certain values of the force imbalance coefficient. It is also shown that a simple scaling argument adiabatically enslaves the orientational field to the density field, yielding the same results as the linear stability analysis. After a discussion of these results, a comparison to Brownian dynamics simulations is shown. The numerical data is also compared to the experiment performed by the research group of *C. Bechinger* at the University of Stuttgart (*2. Physikalisches Institut*).

3.1 Analytical description

The purpose of the analytical description is to provide a theoretical framework derived from first principles, which describes and possibly predicts the onset of the phase separation observed in simulations, see Fig. 3.2. In other words, one starts at the microscopic level of the system, which is given by the Smoluchowski equation derived in Sec. 2.4.3, i.e.,

$$\partial_t \Psi = \sum_{i=1}^N \mu_0 \nabla_i [\nabla_i U - \mu_0^{-1} v_0 \mathbf{e}_i + k_B T \nabla_i] \Psi + \sum_{i=1}^N D_r \partial_{\varphi_i}^2 \Psi. \quad (3.1)$$

3.1.1 One-particle density

The first step is to derive an evolution equation for the one-particle probability density function $\Psi_1(\mathbf{r}_1, \varphi_1, t)$, with $\Psi_1 d\mathbf{r}_1$ being the probability to find a particle, arbitrary labeled with the index 1, at time t in the volume $d\mathbf{r}_1$ around position \mathbf{r}_1 with orientation φ_1 regardless of the configuration of the remaining $N-1$ particles. The considered system contains indistinguishable particles of one single species unlike systems of oppositely driven particles [150, 151], oppositely charged particles [152] or a binary mixture of self-propelled particles [153]. Consequently, Ψ_1 should have the same form no matter which particle is considered. Therefore the subscript of \mathbf{r}_1, φ_1 can be dropped and a randomly tagged particle at position \mathbf{r} with orientation φ is considered, while without loss of generality the remaining particles are numbered from 2 to N . Then, the tagged particle probability density $\Psi_1(\mathbf{r}, \varphi, t)$ is given by integrating the joint probability density function over all possible configurations of the remaining particles, yielding

$$\Psi_1(\mathbf{r}, \varphi, t) = \int d\mathbf{r}_2 \dots d\mathbf{r}_N \int d\varphi_2 \dots d\varphi_N \Psi(\{\mathbf{r}_i\}, \{\varphi_i\}, t), \quad (3.2)$$

where positions are integrated over the total space and the angular integration goes from 0 to 2π . Performing this integration in Eq (3.1). and already applying the reduced units mentioned in Sec. 2.5, i.e., $k_B T = 1$ and $\mu_0 = 1$, Eq. (3.1) becomes

$$\partial_t \Psi_1 = -\nabla \cdot [\mathbf{F}_m + v_0 \mathbf{e} \Psi_1 - \nabla \Psi_1] + D_r \partial_\varphi^2 \Psi_1, \quad (3.3)$$

where the first term in the squared brackets

$$\mathbf{F}_m = \int d\mathbf{r}_2 \dots d\mathbf{r}_N \int d\varphi_2 \dots d\varphi_N (-\nabla_1 U) \Psi \quad (3.4)$$

is the mean force acting on the tagged particle due to pair interactions. The subscript of ∇_1 is only used to distinguish from the variables being integrated and will be dropped later. The second term in Eq. (3.3) is calculated via the fact that the integration over any particle except the tagged one vanishes. Explicitly the calculation is

$$\sum_{i=1}^N \int d\mathbf{r}_2 \dots d\mathbf{r}_N \int d\varphi_2 \dots d\varphi_N \nabla_i (\Psi v_0 \mathbf{e}_i) \quad (3.5)$$

$$= \sum_{i=1}^N v_0 \int d\mathbf{r}_2 \dots d\mathbf{r}_N \int d\varphi_2 \dots d\varphi_N (\mathbf{e}_i \nabla_i \Psi + \underbrace{\Psi \nabla_i \mathbf{e}_i}_{=0}) \quad (3.6)$$

$$= v_0 \mathbf{e}_1 \nabla_1 \Psi_1 + \sum_{i=2}^N v_0 \int \underbrace{d\mathbf{r}_2 \dots d\mathbf{r}_{i-1} d\mathbf{r}_{i+1} \dots d\mathbf{r}_N}_{=d\mathbf{r}_3 \dots d\mathbf{r}_N \text{ for } i=2} \int d\varphi_2 \dots d\varphi_N \mathbf{e}_i [\Psi]_{\mathbf{r}_i \rightarrow -\infty}^{\mathbf{r}_i \rightarrow \infty} \quad (3.7)$$

$$= v_0 \mathbf{e}_1 \nabla_1 \Psi_1, \quad (3.8)$$

where the subscript for ∇_1 and \mathbf{e}_1 is dropped after the calculation. The squared brackets in Eq. (3.7) indicate that Ψ is evaluated at $x_i, y_i \rightarrow \pm\infty$, which needs to vanish in any case, otherwise it would not be able to normalize the function. The third term of Eq. (3.3) is calculated in a similar way with the same argument regarding the behavior of Ψ towards infinity. The last term of Eq. (3.3) is given by the following calculation

$$\sum_{i=1}^N D_r \int d\mathbf{r}_2 \dots d\mathbf{r}_N \int d\varphi_2 \dots d\varphi_N \partial_{\varphi_i}^2 \Psi \quad (3.9)$$

$$= D_r \partial_{\varphi_1}^2 \Psi_1 + D_r \sum_{i=2}^N \int d\mathbf{r}_2 \dots d\mathbf{r}_N \int \underbrace{d\varphi_2 \dots \varphi_{i-1} \varphi_{i+1} \dots d\varphi_N}_{=d\varphi_3 \dots d\varphi_N \text{ for } i=2} [\partial_{\varphi_i} \Psi]_{\varphi_i=0}^{\varphi_i=2\pi} \quad (3.10)$$

$$= D_r \partial_{\varphi_1}^2 \Psi_1, \quad (3.11)$$

where one has used that Ψ and all its derivatives are 2π -periodic functions with respect to φ_i . Again, to finally obtain the fourth term of Eq. (3.3) the subscript of φ_1 is dropped. The next step is now to rewrite Eq. (3.3) in terms of the one-particle density $\rho_1(\mathbf{r}, \varphi, t)$, which is done by a simple multiplication with N , more precisely

$$\rho_n(\mathbf{r}_1, \dots, \mathbf{r}_n, \varphi_1, \dots, \varphi_n, t) = \frac{N!}{(N-n)!} \int d\mathbf{r}_{n+1} \dots d\mathbf{r}_N \int d\varphi_{n+1} \dots d\varphi_N \Psi. \quad (3.12)$$

Eq. (3.3) now reads

$$\partial_t \rho_1 = -\nabla \cdot [\mathbf{F} + v_0 \mathbf{e} \rho_1 - \nabla \rho_1] + D_r \partial_\varphi^2 \rho_1, \quad (3.13)$$

with

$$\mathbf{F} = N \int d\mathbf{r}_2 \dots d\mathbf{r}_N \int d\varphi_2 \dots d\varphi_N (-\nabla_1 U) \Psi. \quad (3.14)$$

The quantity $-\nabla_1 U$ can be expressed as

$$-\nabla_1 U = - \sum_{j=2}^N u'(|\mathbf{r}_j - \mathbf{r}_1|) \frac{\mathbf{r}_j - \mathbf{r}_1}{|\mathbf{r}_j - \mathbf{r}_1|} \cdot (-1) \quad (3.15)$$

$$= - \sum_{j=2}^N u'(|\mathbf{r}_1 - \mathbf{r}_j|) \frac{\mathbf{r}_1 - \mathbf{r}_j}{|\mathbf{r}_1 - \mathbf{r}_j|}, \quad (3.16)$$

where $u'(r)$ denotes the derivative of $u(r)$ with respect to the argument. After dropping the subscript, Eq. (3.14) is given by

$$\mathbf{F} = -N \int d\mathbf{r}_2 \dots d\mathbf{r}_N \int d\varphi_2 \dots d\varphi_N \left(\sum_{j=2}^N u'(|\mathbf{r}_j - \mathbf{r}|) \frac{\mathbf{r} - \mathbf{r}_j}{|\mathbf{r} - \mathbf{r}_j|} \right) \Psi. \quad (3.17)$$

The sum is now written as $N-1$ separate integrals, where in each the particle interacting with the tagged particle is labeled as particle 2, which is allowed since particles are indistinguishable. The position and orientation of this arbitrary particle is now written as \mathbf{r}' and φ' to avoid further confusion, which leads to

$$\mathbf{F} = -N(N-1) \int d\mathbf{r}' d\mathbf{r}_3 \dots d\mathbf{r}_N \int d\varphi' d\varphi_3 \dots d\varphi_N u'(|\mathbf{r} - \mathbf{r}'|) \frac{\mathbf{r} - \mathbf{r}'}{|\mathbf{r} - \mathbf{r}'|} \Psi. \quad (3.18)$$

Again, the subscript does not imply fixed particle indices, but serve to distinguish between the variables being integrated. According to Eq. (3.12) the quantity \mathbf{F} is written in terms of a two-particle density

$$\mathbf{F} = - \int d\mathbf{r}' \int d\varphi' u'(|\mathbf{r}' - \mathbf{r}|) \frac{\mathbf{r} - \mathbf{r}'}{|\mathbf{r} - \mathbf{r}'|} \rho_2(\mathbf{r}, \mathbf{r}', \varphi, \varphi', t) \quad (3.19)$$

$$= - \int d\mathbf{r}' u'(|\mathbf{r}' - \mathbf{r}|) \frac{\mathbf{r} - \mathbf{r}'}{|\mathbf{r} - \mathbf{r}'|} \tilde{\rho}_2(\mathbf{r}, \mathbf{r}', \varphi, t). \quad (3.20)$$

In the last step it has already been integrated over the orientational degree of freedom of a particle at \mathbf{r}' so that $\tilde{\rho}_2(\mathbf{r}, \mathbf{r}', \varphi, t)$ is the two-particle density of finding a particle at time t at position \mathbf{r}' with arbitrary orientation, while the tagged particle is at \mathbf{r} with orientation φ . One could now go back to the Smoluchowski equation and integrate it over the degrees of freedom of $N-2$ particles, which would then give a connection between the two particle density and the three particle density. This systematic coupled chain of equations is called the BBGKY (Bogoliubov-Born-Green-Kirkwood-Yvon) hierarchy [154–159].

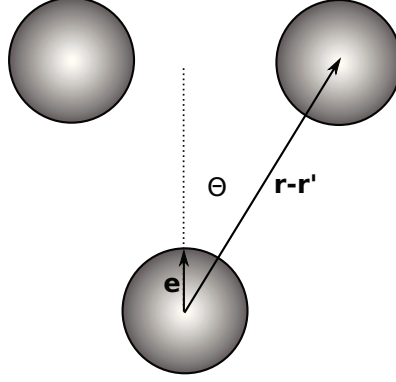


Figure 3.3: Sketch of the reference frame for the function $g(|\mathbf{r} - \mathbf{r}'|, \theta|_{\langle (\mathbf{r} - \mathbf{r}', \mathbf{e})}, t)$.

At this part of the derivation an approximate closure for the coupled chain of equations needs to be found. Generally, the pair correlation function is the normalized two particle density, yielding

$$\rho_2(\mathbf{r}, \mathbf{r}', t) = \rho_1(\mathbf{r}, t)\rho_1(\mathbf{r}', t)g(\mathbf{r}, \mathbf{r}', t). \quad (3.21)$$

Applying this relation and extending it to orientational degrees of freedom, but with only the orientation of one particle being relevant, one gets

$$\tilde{\rho}_2(\mathbf{r}, \mathbf{r}', \varphi, t) = \rho_1(\mathbf{r}, \varphi, t)\rho_1(\mathbf{r}', t)g(\mathbf{r}, \mathbf{r}', \varphi, t). \quad (3.22)$$

As mentioned before, the goal is to develop a theoretical framework for the onset of the phase separation. Hence the quantity $\tilde{\rho}_2$ can be approximated by treating it as being evaluated in a homogeneous system and Eq. (3.22) is approximated as

$$\tilde{\rho}_2(\mathbf{r}, \mathbf{r}', \varphi, t) \simeq \rho_1(\mathbf{r}, \varphi, t)\bar{\rho}g(|\mathbf{r} - \mathbf{r}'|, \theta|_{\langle (\mathbf{r} - \mathbf{r}', \mathbf{e})}, t), \quad (3.23)$$

where $\bar{\rho}$ is the homogeneous density of the suspension regardless of the particle orientation. In addition the reference frame has changed such that φ is considered to be fixed along a given axis, but \mathbf{r}' is moved accordingly, so that θ is the angle enclosed by the connection vector $\mathbf{r}' - \mathbf{r}$ (pointing away from the tagged particle) and the orientation \mathbf{e} of the tagged particle, see Fig. 3.3. Furthermore two assumptions are made: time dependency is neglected (initially homogeneous suspension) and it is assumed that the pair correlation function depends only on relative and not absolute particle positions. Thereby the projection $\mathbf{e}\mathbf{F}$ on the orientation of the tagged particle is written as

$$\mathbf{e}\mathbf{F} = -\bar{\rho}\zeta\rho_1 \quad (3.24)$$

with

$$\zeta = \int_0^\infty dr r[-u'(r)] \int_0^{2\pi} d\theta \cos\theta g(r, \theta). \quad (3.25)$$

The quantity $\mathbf{e}\mathbf{F}$ can be seen as the force exerted on the tagged particle because it is persistently propelling against other particles, which is the reason why ζ will be referred

as the force imbalance coefficient. So far the specific form of the pair potential $u(r)$ has not been taken into account. If the specific function of the pair potential is known, the first integral in Eq. (3.25) can be calculated analytically or approximated numerically. For a fixed pair potential ζ is mainly determined by the degree of anisotropy of the pair correlation function. It is also noteworthy that the calculations above do not give an analytical closed theory to fully characterize the system, but rather provide the desired theoretical framework, where the pair correlation function is needed as an input, which will be obtained via computer simulations.

The next step is to assume that the vectors \mathbf{e} and $\nabla\rho_1$ are linear independent, which is quite reasonable considering that other particles also propel themselves while one given particle moves through the suspension. As a result the particles orientation is rarely exactly parallel or antiparallel to the density gradient. Then the vector \mathbf{F} can be decomposed in terms of the non orthogonal basis given by \mathbf{e} and $\nabla\rho_1$, i.e.,

$$\mathbf{F} = (\mathbf{e}\mathbf{F})\mathbf{e} + (1 - D)\nabla\rho_1, \quad (3.26)$$

where D is technically given by

$$D = 1 - \mathbf{F} \frac{\nabla\rho_1 - \mathbf{e}(\mathbf{e}\nabla\rho_1)}{|\nabla\rho_1|^2}. \quad (3.27)$$

Finally, by putting Eqs. (3.24) and (3.26) into Eq. (3.13) one obtains the evolution equation for the one-particle density of an interacting system of self-propelled particles

$$\partial_t\rho_1 = -\nabla[(v_0 - \bar{\rho}\zeta)\mathbf{e} - D\nabla]\rho_1 + D_r\partial_\varphi^2\rho_1. \quad (3.28)$$

In equilibrium the particles do not propel themselves ($v_0 = 0$) and the suspension is homogeneous, implying $\zeta = 0$. Consequently, to be consistent with the description of the equilibrium system, disregarding the rather complex form of Eq. (3.27), the coefficient D is associated with the long time diffusion coefficient of the corresponding passive suspension.

3.1.2 Effective swimming speed

By introducing an effective swimming speed

$$v = v_0 - \bar{\rho}\zeta, \quad (3.29)$$

one can rewrite Eq. (3.28) into

$$\partial_t\rho_1 = -\nabla[v\mathbf{e} - D\nabla]\rho_1 + D_r\partial_\varphi^2\rho_1, \quad (3.30)$$

where all particle interactions are completely absorbed into the effective swimming speed v and the long time diffusion coefficient D . This implies a mapping to non-interacting particles with an intrinsic swimming speed equal to v (instead of v_0) and a bare diffusion coefficient D (instead of D_0). The long-time diffusion coefficient D_{lt} of such an effective system can be derived by the corresponding Langevin equation and is given by

$$D_{lt} = \lim_{t \rightarrow \infty} \frac{1}{4} \frac{d}{dt} \langle [\mathbf{r}(t) - \mathbf{r}(0)]^2 \rangle = D + \frac{v^2}{2D_r}. \quad (3.31)$$

3.2 Linear stability analysis

The key towards an analytical description of the phase separation dynamics is to study the stability of the system with respect to small density fluctuations, which, if the system is unstable, grow and are responsible for a phase separation scenario. The approach is to derive an evolution equation for the local density $\rho(\mathbf{r}, t)$ of the suspension. Then, the local density is considered to be homogeneous, but with a small deviation, i.e., $\rho(\mathbf{r}, t) = \bar{\rho} + \delta\rho(\mathbf{r}, t)$, where the temporal evolution of the perturbation $\delta\rho$ is analyzed.

3.2.1 Effective hydrodynamic equations

First, from Eq. (3.30) a more familiar description is derived, which are effective hydrodynamic equations coupling the density and orientational field of the suspension, see also Refs. 160, 161. The density field is given by integrating ρ_1 over the orientational degree of freedom, i.e.,

$$\rho(\mathbf{r}, t) = \int_0^{2\pi} d\varphi \rho_1(\mathbf{r}, \varphi, t), \quad (3.32)$$

while the orientational field is the first moment of the orientation, yielding

$$\mathbf{p}(\mathbf{r}, t) = \int_0^{2\pi} d\varphi \mathbf{e} \rho_1(\mathbf{r}, \varphi, t). \quad (3.33)$$

By performing these integrations in Eq. (3.30) one gets for the density field the following differential equation

$$\partial_t \rho = -\nabla \cdot [v\mathbf{p} - D\nabla\rho], \quad (3.34)$$

while for the orientational field one have at first to treat terms involving

$$\mathbf{e}\mathbf{e}^T = \frac{1}{2}\mathbf{1} + \frac{1}{2} \begin{pmatrix} \cos 2\varphi & \sin 2\varphi \\ \sin 2\varphi & -\cos 2\varphi \end{pmatrix}. \quad (3.35)$$

In order to obtain a closure the second harmonic terms are dropped. Later in this section it will be shown, that only instabilities on large length scales are able to cause the instability and since the system is initially considered to be near the homogeneous solution, the term with the second harmonics can be neglected by imagining averaging over all orientations in a large area, yielding the second term in Eq. (3.35) to become zero. The evolution equation of the orientational field then reads

$$\partial_t \mathbf{p} = -\frac{1}{2}\nabla(v\rho) + D\nabla^2 \mathbf{p} - D_r \mathbf{p}. \quad (3.36)$$

3.2.2 Perturbation of the homogeneous suspension

The homogeneous solutions of the coupled Eqs. (3.34) and (3.36) are given by $\rho = \bar{\rho}$ and $\mathbf{p} = 0$ with $\bar{\rho}$ being the homogeneous density. Now, small perturbation fields of this solutions are considered, i.e., $\rho(\mathbf{r}, t) = \bar{\rho} + \delta\rho(\mathbf{r}, t)$ and $\mathbf{p}(\mathbf{r}, t) = \delta\mathbf{p}(\mathbf{r}, t)$. In order to analyze the temporal evolution of these perturbations, the force imbalance coefficient ζ is treated as a controllable parameter independent of the density. In addition, it is reasonable to assume that the effective swimming speed depends on the local density, whose expression is still needed to close the equations¹. That expression has been approximated by simply replacing the homogeneous density $\bar{\rho}$ in $v = v_0 - \bar{\rho}\zeta$ with the local density ρ , which is obviously contradictory regarding the previous results, but not a too big mistake regarding small deviations $\delta\rho$. In the following, the expression v denotes the global effective swimming speed $v = v_0 - \bar{\rho}\zeta$, while the expression $v_l = v_0 - \rho\zeta$ is the approximated local swimming speed depending on the local density $\rho(\mathbf{r}, t)$. The expression $v_l\rho$ is then given by

$$v_l\rho = (v_0 - \zeta\rho)\rho = v\bar{\rho} + w\delta\rho + \mathcal{O}(\delta\rho^2) \quad (3.37)$$

with $w = v_0 - 2\bar{\rho}\zeta$ and $\mathcal{O}(\delta\rho^2)$ indicating terms of second order in $\delta\rho$ being neglected in the following. Finally, the temporal evolution of the perturbations is given by setting $\rho = \bar{\rho} + \delta\rho$, $\mathbf{p} = \delta\mathbf{p}$ and $v = v_l$ in Eqs. (3.34) and (3.36), which is written as

$$\partial_t\delta\rho = -\nabla[v_l\delta\mathbf{p} - D\nabla\delta\rho], \quad (3.38)$$

$$\partial_t\delta\mathbf{p} = -\underbrace{\frac{1}{2}\nabla(v\bar{\rho} + w\delta\rho)}_{=-\frac{1}{2}w\nabla\delta\rho} + D\nabla^2\delta\mathbf{p} - D_r\delta\mathbf{p}. \quad (3.39)$$

By neglecting nonlinear terms of the perturbations, Eqs. (3.38) and (3.39) are given by

$$\partial_t\delta\rho = -\nabla[v\delta\mathbf{p} - D\nabla\delta\rho], \quad (3.40)$$

$$\partial_t\delta\mathbf{p} = -\frac{1}{2}w\nabla\delta\rho + D\nabla^2\delta\mathbf{p} - D_r\delta\mathbf{p}. \quad (3.41)$$

Note that the only difference is v instead of v_l on the right hand side of Eq. (3.40). Now the spatial Fourier transforms of $\delta\rho$ and $\delta\mathbf{p}$ are considered. In d spatial dimensions the Fourier transform of a function $f(\mathbf{r}, t)$ is given by

$$\tilde{f}(\mathbf{q}, t) = \frac{1}{(2\pi)^{d/2}} \int d\mathbf{r} f(\mathbf{r}, t) e^{i\mathbf{q}\mathbf{r}} \quad (3.42)$$

where \mathbf{q} is the d -dimensional wave vector in Fourier space. The inverse Fourier transform then reads

$$f(\mathbf{r}, t) = \frac{1}{(2\pi)^{d/2}} \int d\mathbf{q} \tilde{f}(\mathbf{q}, t) e^{-i\mathbf{q}\mathbf{r}}. \quad (3.43)$$

¹It has been shown generally, that density dependent local mobility can cause phase separation in case of run-and-tumble bacteria [132, 134], which can be mapped to the here employed system of active Brownian particles [162].

By defining the vector $\mathbf{z} = (\delta\tilde{\rho}, \delta\tilde{p}_x, \delta\tilde{p}_y)$, where $\delta\tilde{p}_\alpha$ is the Fourier transform of the component α of $\delta\mathbf{p}$, Eqs. (3.40) and (3.41) are written as

$$\partial_t \mathbf{z}(\mathbf{q}, t) = -\mathbb{A}(\mathbf{q})\mathbf{z}(\mathbf{q}, t), \quad (3.44)$$

whose solution is

$$\mathbf{z}(\mathbf{q}, t) = e^{-\mathbb{A}t}\mathbf{z}(\mathbf{q}, 0). \quad (3.45)$$

Here the 3×3 coefficient matrix has been introduced, which is given by

$$\mathbb{A}(\mathbf{q}) = \begin{pmatrix} Dq^2 & ivq_x & ivq_y \\ \frac{1}{2}iwq_x & Dq^2 + D_r & 0 \\ \frac{1}{2}iwq_y & 0 & Dq^2 + D_r \end{pmatrix}. \quad (3.46)$$

If one of the eigenvalues of \mathbb{A} is negative, small density perturbations would not only grow exponentially, cf. Eq. (3.45), but also unbounded, which is actually an artifact of the linearization, since the coupling to higher nonlinear orders leads to a saturation of the instability. However, the three eigenvalues of \mathbb{A} are given by

$$\lambda_0 = Dq^2 + D_r \quad (3.47)$$

$$\lambda_{\pm} = Dq^2 + \frac{D_r}{2} \pm \sqrt{\frac{D_r^2}{4} - \frac{1}{2}vwq^2}, \quad (3.48)$$

where the diffusion coefficients D and D_r are positive, so that the only possible negative eigenvalue is λ_- . At this step, very small wave vectors are considered, i.e., $D_r^2/4 \gg vwq^2/2$, which is true for $q \rightarrow 0$ corresponding to an instability on large length scales and was already used to neglect the second harmonics in Eq. (3.35). After approximating the square root for $q \rightarrow 0$ the relevant eigenvalue reads

$$\lambda_- \approx \left(D + \frac{vw}{2D_r} \right) q^2, \quad (3.49)$$

which is negative if $D + vw/(2D_r) < 0$. Since ζ has been treated as a controllable parameter this condition is solved in terms of ζ , which yields an unstable behavior ($\lambda_- < 0$) for $\zeta_- \leq \zeta \leq \zeta_+$, where the boundaries are given by

$$\bar{\rho}\zeta_{\pm} = \frac{3}{4}v_0 \pm \frac{1}{4}\sqrt{v_0^2 - v_*^2} \quad (3.50)$$

with

$$v_* = 4\sqrt{DD_r}. \quad (3.51)$$

Eq. (3.50) provides a possible prediction for what values of ζ the system will be unstable. In addition, ζ is a real value, so that $v_0 > v_*$ needs to be fulfilled. Therefore v_* is the minimal (not the critical) intrinsic velocity needed for the instability to occur.

3.2.3 Scaling argument

In this section a more demonstrative derivation of Eq. (3.50) is provided. Starting with the effective hydrodynamic Eqs. (3.34) and (3.36), the effective swimming speed is again approximated to be locally dependent on the density according to

$$v_l = v_0 - \zeta\rho, \quad (3.52)$$

yielding

$$\partial_t \rho = -\nabla \cdot [v_l \mathbf{p} - D \nabla \rho] \quad (3.53)$$

$$\partial_t \mathbf{p} = -\frac{1}{2} \nabla (v_l \rho) + D \nabla^2 \mathbf{p} - D_r \mathbf{p}. \quad (3.54)$$

Instead of performing a linear stability analysis in Fourier space, two assumptions are now made regarding the length and time scales of the instability. First, in accordance with the previous assumption $q \rightarrow 0$, the limit of large length scales is considered as well as times much longer than the reorientation time $1/D_r$ of a particle. Hence, Eq. (3.54) simplifies to

$$\mathbf{p} \approx -\frac{1}{2D_r} \nabla (v_l \rho) = -\frac{v_0 - 2\rho\zeta}{2D_r} \nabla \rho, \quad (3.55)$$

where the orientational field is adiabatically enslaved to the density field. Plugging this result into Eq. (3.53) yields the diffusion equation

$$\partial_t \rho = \nabla \left[D + \frac{(v_0 - \zeta\rho)(v_0 - 2\rho\zeta)}{2D_r} \right] \nabla \rho = \nabla \mathcal{D} \nabla \rho, \quad (3.56)$$

where one can define the local diffusion coefficient

$$\mathcal{D}(\rho) = \left[D + \frac{(v_0 - \zeta\rho)(v_0 - 2\rho\zeta)}{2D_r} \right]. \quad (3.57)$$

For negative values the suspension is unstable, since particles accumulate at denser regions. Consequently, an initial homogeneous suspension needs to fulfill $\mathcal{D}(\bar{\rho}) < 0$ to be unstable, which gives the already derived instability region $\zeta_- \leq \zeta \leq \zeta_+$ presented in Eq. (3.50) with

$$\bar{\rho}\zeta_{\pm} = \frac{3}{4}v_0 \pm \frac{1}{4}\sqrt{v_0^2 - v_*^2}. \quad (3.58)$$

3.2.4 Discussion

In this section the results and its consequences of the previous analysis are presented qualitatively. First, the minimal velocity for the instability to occur is considered to be fixed, assuming the arbitrary reduced value $v_* = 1$. The instability region can now be plotted in the $v_0 - \bar{\rho}\zeta$ plane, which is seen in Fig. 3.4. The previous analysis predicts an unstable system for values of $\bar{\rho}\zeta$ within the blue-filled area in Fig. 3.4. The dashed

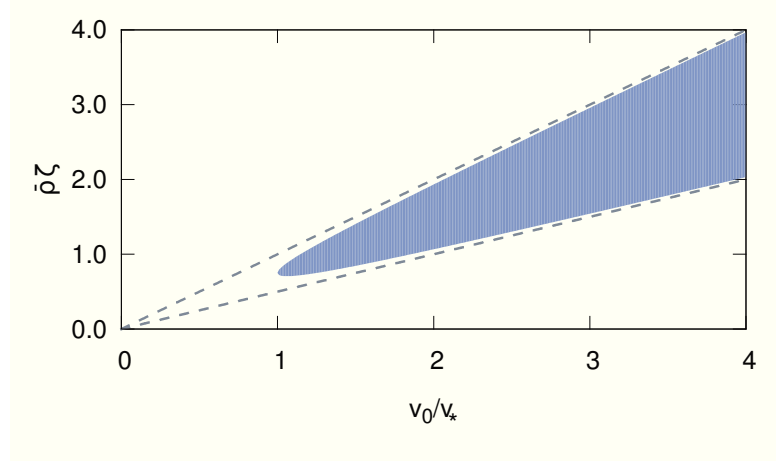


Figure 3.4: $\bar{\rho}\zeta$ plotted as a function of the reduced intrinsic swimming speed v_0 at fixed $v_* = 1$. The blue-filled area is the instability region according to Eq. (3.58), while the dashed lines correspond to the asymptotes $\bar{\rho}\zeta = v_0/2$ and $\bar{\rho}\zeta = v_0$.

lines in Fig. 3.4 are the asymptotes of this area, i.e., $\bar{\rho}\zeta = v_0/2$ and $\bar{\rho}\zeta = v_0$ respectively. Recalling the expression of the effective swimming speed

$$v = v_0 - \bar{\rho}\zeta, \quad (3.59)$$

one can see, that values beyond the upper dashed line ($\bar{\rho}\zeta > v_0$) are unphysical, since this would result in a slowdown being stronger than the intrinsic speed itself and the particle would propel in the opposite direction ($v < 0$). Another point is that the instability only occurs if the slowdown is sufficiently strong. This provides the microscopic picture of particles trapping each other due to the persistence of their self-propulsion, which leads to an unstable system if other particles join these trapped particles before they can reorient and leave the aggregate. This picture is also reflected in the evolution equation of the density field and the adiabatic coupling between orientational field and density field, i.e.,

$$\partial_t \rho = -\nabla \cdot [v_l \mathbf{p} - D \nabla \rho], \quad (3.60)$$

$$\mathbf{p} = -\frac{1}{2D_r} \nabla(v_l \rho). \quad (3.61)$$

Putting those equations together yields

$$\partial_t \rho = -\nabla \cdot \left[-\frac{v_l}{2D_r} \nabla(v_l \rho) - D \nabla \rho \right], \quad (3.62)$$

which is a diffusion equation with the two competing fluxes pointing in directions $-\nabla(v_l \rho)$ and $-\nabla \rho$. As sketched in Fig. 3.5, the flux $-\nabla \rho$ always points to the dilute region of the system, favoring stability. The direction of the flux $-\nabla(v_l \rho)$ cannot be specified in general. Assuming the local velocity v_l of the particles outside a dense

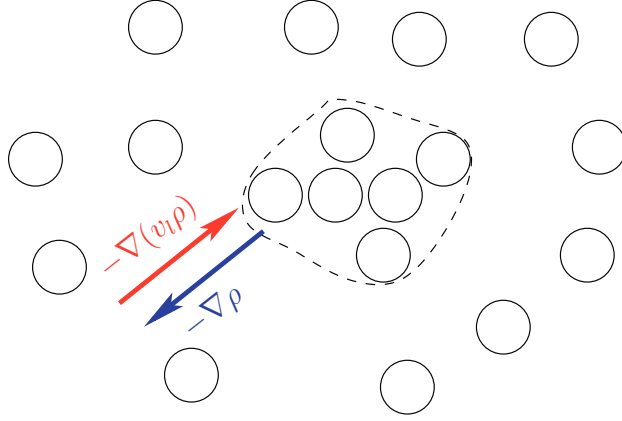


Figure 3.5: Sketch of the two competing fluxes $-\nabla(v_l\rho)$ (red) and $-\nabla\rho$ according to Eq. (3.62). The area enclosed by the dashed line indicates a denser region than on the outside. It is assumed that the product $v_l\rho$ is smaller in the denser region than in the dilute surrounding, causing the vector $-\nabla(v_l\rho)$ (red) to point in the opposite direction of $-\nabla\rho$ (blue).

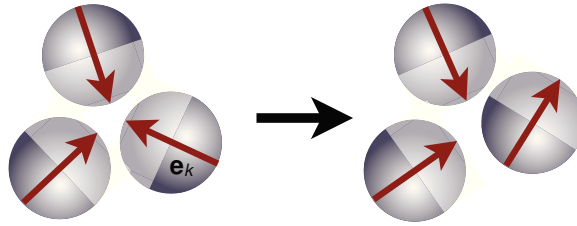


Figure 3.6: Sketch of the self-trapping mechanism where for a stable suspension particles need to reorient before further particles can join the cluster. If reorientation is too slow this would lead to a phase separated system.

region (area enclosed by the dashed line) does not differ a lot from those in the dense region, this flux would also point to the dilute region and stabilize the system. But if particles are slowed down a lot due to the interparticle collisions, the particles in the dilute region are significantly faster. Then the product $v_l\rho$ is lower in the dense region, yielding a flux which points towards the dense aggregate, i.e., particles accumulate at dense regions until steady state (a finite cluster size) is reached. In addition Eq. (3.62) shows that the flux which might favor phase separation scales as v_l/D_r , while the diffusion part scales as expected linearly with D . This demonstrates the competition between timescales, where particles at first collide and form an initial cluster. If they do not leave the cluster too quick due to reorientation or translational diffusion, i.e., D_r and D are sufficiently small, surrounding particles might join the initial cluster, see also Ref. 34 for kinetic rate equations based on this physical picture. In the following this effect is referred as *self-trapping* mechanism of particles and is sketched in Fig. 3.6.

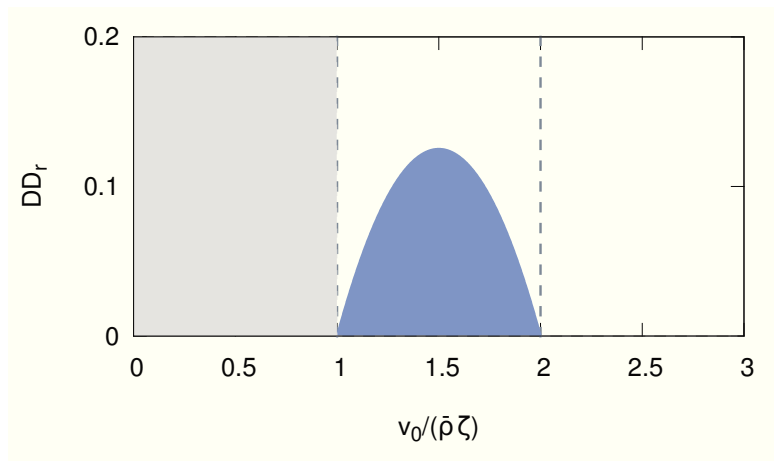


Figure 3.7: DD_r plotted as a function of the reduced intrinsic swimming speed v_0 at fixed $\bar{\rho}\zeta = 1$. The blue-filled area is the instability region according to Eq. (3.58), while the dashed lines correspond to $\zeta\bar{\rho} = v_0/2$ and $\zeta\bar{\rho} = v_0$. The gray filled area corresponds to physical forbidden data points.

However, the force imbalance coefficient ζ is a rather abstract quantity based on the structure of the suspension. Another approach is to fix $\bar{\rho}\zeta$, again $\bar{\rho}\zeta = 1$ is chosen arbitrary, and plot the instability region in the $v_0 - DD_r$ plane, see Fig. 3.7. One should note that $\bar{\rho}\zeta = 1$ has been fixed, so that the system is considered as already self-propelled and values $v_0 < \bar{\rho}\zeta$ are unphysical ($v < 0$ not allowed). Therefore only values to the right of the left dashed line are considered in Fig. 3.7. The quantity DD_r is now connected to more demonstrative quantities, i.e., one could claim that DD_r grows as temperature increases while it decreases as the system gets denser. The specific functional relation is not needed for a qualitative discussion. At $T = 0$ the minimal velocity for an unstable system is zero, resulting in a suspension, which is unstable for very low propulsion speeds. Again, this is reflected in the competition of timescales, where no diffusion is present to compete against the persistence motion. In addition, Fig. 3.7 shows a reentrant behavior, which is not so much reflected in Fig. 3.4. If the particles propulsion is too strong, the system gets stable again, which is at first glance surprising since very fast particles have a large persistence length and translational diffusion is of course not dominant. The explanation is that particles which are very fast compared to the velocities arising from particle interactions do not block each other anymore, or at least the blocking is not sufficiently strong, i.e., colliding particles are just pushed away very quickly. Fig. 3.7 also shows that there is a maximum value of DD_r , equivalent to a minimal density, for which the system can become unstable in the first place. The form of the blue-filled area also indicates, that for dilute systems, i.e. higher DD_r , a stronger propulsion is needed to achieve an unstable system, but a lower swimming speed to reenter the stable regime.

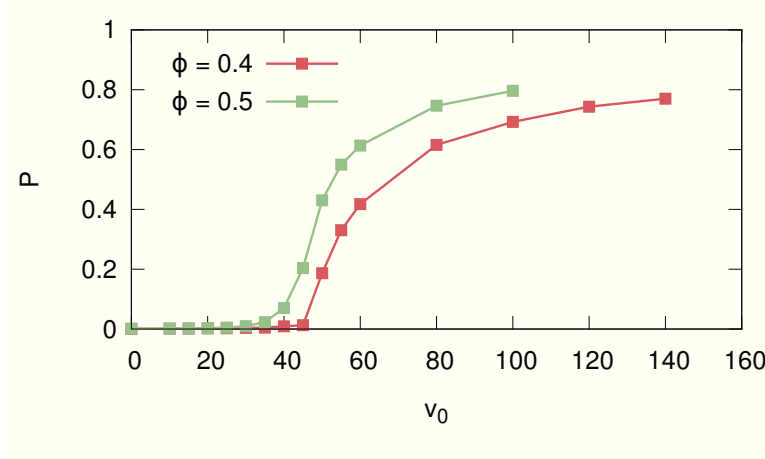


Figure 3.8: Mean relative size P of the largest cluster in the system as a function of free propelling speed v_0 at packing fractions $\phi = 0.4$ and $\phi = 0.5$. The squares correspond to results from simulation runs, which are connected by straight lines.

3.3 Numerical results

3.3.1 Quantifying the phase transition

The calculations above are now compared to the results of Brownian dynamics simulations with $N = 4900$ particles in a quadratic simulation box at packing fractions $\phi \geq 0.36$ (lower packing fractions are discussed in Chap. 4) and various propelling speeds v_0 . Starting from the passive suspension at equilibrium (randomly distributed orientations), the propulsion has been turned on and the suspension first relaxed for $t_r = 100$ into steady state before data has been collected for another simulation time $t_s = 100$. As mentioned before, for sufficiently strong propelling speeds, one observes phase separation into one large dense cluster surrounded by a dilute fluid phase. First of all, for a proper comparison with the analytical results, an appropriate order parameter needs to be defined which characterizes this transition. A good quantity is certainly the mean relative size (strength) of the largest cluster in the system. Particles are considered to be in the same cluster if they overlap ($r_{ij} < 2R$), so that

$$P = \frac{\langle N_c \rangle}{N} \quad (3.63)$$

is the mean relative size of the largest cluster in the system, where N_c is the number of particles in the largest cluster. In App. A.1 a finite size analysis based on the order parameter P is performed to show that the system size $N = 4900$ is sufficiently large to study the properties of the steady state. Fig. 3.8 shows a continuous increase of the order parameter P , which is an indication of a second order phase transition. One should note that the denser system at $\phi = 0.5$ phase separates at lower propelling speeds than

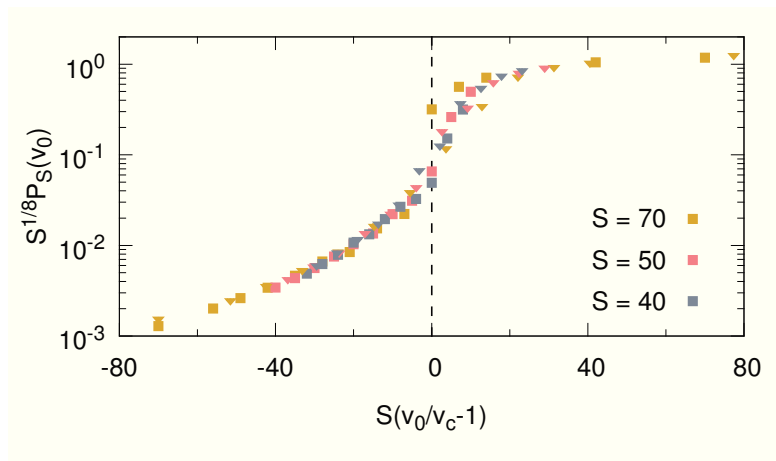


Figure 3.9: Plot of $P_S(v_0)S^{\beta/\nu}$ on a logarithmic scale as a function of $S^{1/\nu}\epsilon$, which results in a collapse into the universal scaling function \tilde{P} by applying the critical exponents of the 2d Ising model $\beta = 1/8$ and $\nu = 1$ for packing fractions $\phi = 0.4$ (\blacksquare , $v_c = 50$) and $\phi = 0.5$ (\blacktriangledown , $v_c = 38$).

the system at $\phi = 0.4$, which confirms the previous statement that dense systems need a lower propelling speed to get unstable. In accordance with the analytical results, but not plotted here, it has been observed that for this particular simulation protocol (starting as a homogeneous equilibrium suspension) a minimal density is necessary for which the order parameter P shows indication of a phase transition in the first place. The details of the phase transition to a phase separated system turned out to be more complex than it appears at first glance and are discussed extensively in Chap. 4. Nevertheless it is necessary to somehow define a critical velocity for this transition. Motivated from the continuous increase of P , which has the appearance of a second order phase transition, a finite size analysis has been performed, where also the system sizes $S = \sqrt{N} = 40$ and $S = \sqrt{N} = 50$ are considered. Defining $\epsilon = v_0/v_c - 1$ as the relative deviation from the critical velocity, finite size scaling predicts [163]

$$P_S(v_0) = S^{-\beta/\nu} \tilde{P}(S^{1/\nu}\epsilon), \quad (3.64)$$

where S is the characteristic size of the system (here \sqrt{N}), $P_S(v_0)$ the order parameter as a function of v_0 for the system size S and \tilde{P} is a universal scaling function [164]. Hence, by applying the critical exponents of a given universality class² and plotting the product $P_S(v_0)S^{\beta/\nu}$ as a function of $S^{1/\nu}\epsilon$, the curves for all system sizes should collapse on one curve: the universal scaling function \tilde{P} . This procedure is performed for each packing fraction and each system size, resulting in 6 graphs, where for each packing fraction (3 graphs) the value of the critical velocity v_c is tuned to optimize the collapse behavior. The best collapse has been achieved for the critical exponents of the 2d Ising

²universality classes serve to classify phase transitions where close to the critical point the physical quantities scale according to power laws with critical exponents. See Ref. 165 for a detailed review on universality classes

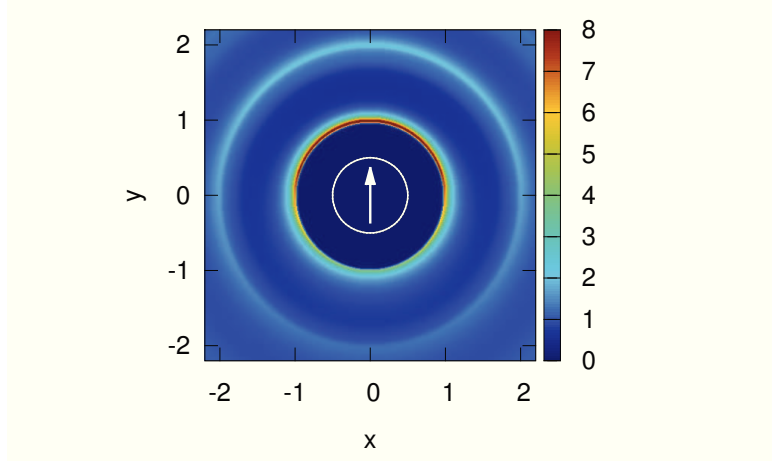


Figure 3.10: Anisotropic pair correlation function $g(r, \theta)$ in the xy -plane at intrinsic swimming speed $v_0 = 20$ and packing fraction $\phi = 0.5$. The white circle indicates the shape of the particle and the white arrow its orientation. The pair correlation function is colored according to its value, showing that particles accumulate in the direction of propulsion, leaving a lack of particles behind the reference particle.

model [166] $\beta = 1/8$ and $\nu = 1$ and critical velocities $v_c = 38$ and $v_c = 50$ respectively for the packing fractions $\phi = 0.5$ and $\phi = 0.4$, see Fig. 3.9. It is noteworthy to point out that there is no theoretical basis of applying the two-dimensional Ising model and that the collapse is somehow better for $v_0 < v_c$. This finite size analysis should only be seen as a method to give an estimation of the critical propelling velocities v_c .

3.3.2 Force imbalance coefficient

Now, the force imbalance coefficient ζ is calculated by evaluating the integrals in Eq. (3.25). In Fig. 3.10 an example for $g(r, \theta)$ is shown, where the highest probability to find particles is in the direction of propulsion, which is reasonable since the particle is slowed down due to collisions appearing in the direction of its persistent motion. However, the values calculated for ζ are now compared to the boundaries ζ_{\pm} of an unstable system, which is illustrated in Fig. 3.11. The previously estimated critical velocities v_c of the finite size analysis are represented by the vertical dashed lines and do indeed coincide quite well with the values of v_0 where the measured slowdown $\bar{\rho}\zeta$ crosses the lower dashed line and enters the instability region. In addition, by measuring the long-time diffusion coefficient of the passive suspension, the free swimming speed v_0 is normalized to the minimal velocity v_* necessary for an unstable system. This illustrates that v_* can indeed be seen as a minimal velocity but not as a critical velocity since the system gets unstable for swimming speeds which are about one order of magnitude larger.

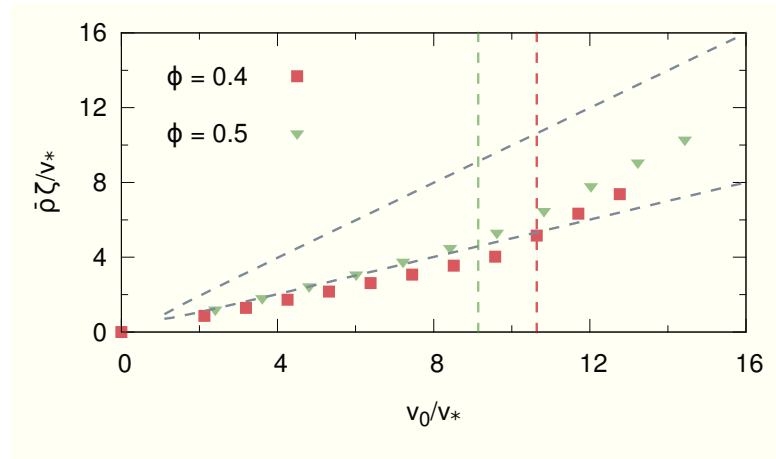


Figure 3.11: Reduced force imbalance coefficient ζ as a function of the free swimming speed v_0 normalized to the minimal velocity v_* necessary for an unstable system at packing fractions $\phi = 0.4$ and $\phi = 0.5$. The vertical red and green dashed lines correspond to the critical velocities $v_c = 50$ (■, $\phi = 0.4$) and $v_c = 38$ (▼, $\phi = 0.5$) estimated by the finite size analysis in Section 3.3.1. The two other dashed lines are the asymptotes of the values ζ_{\pm} , which enclose the instability region.

3.3.3 Long-time diffusion

In Sec. 3.1.2 the effective long-time diffusion coefficient has been introduced

$$D_{lt} = \lim_{t \rightarrow \infty} \frac{1}{4} \frac{d}{dt} \langle [\mathbf{r}(t) - \mathbf{r}(0)]^2 \rangle = D + \frac{v^2}{2D_r}. \quad (3.65)$$

As mentioned before, this implies that the interacting system with intrinsic swimming speed v_0 can be mapped to a free particle by interchanging $v_0 \leftrightarrow v$ and $D_0 \leftrightarrow D$. In Fig. 3.12 this is tested by measuring the long time diffusion coefficient and comparing it to the analytical prediction. For sufficiently low values of the effective swimming speed v the mapping of Eq. (3.65) holds, while it breaks down as soon as the effective swimming speed saturates and only the long-time diffusion keeps growing. These values correspond to a phase separated suspension and show that the mapping only holds for stable suspensions. The fact that the long-time diffusion coefficient still grows shows that particles are constantly exchanged between the two phases.

3.3.4 Further pair potentials and reentrant behavior

In this section it is demonstrated that the phase separation is a generic phenomenon and also appears for other pure repulsive pair potentials. The previous numerical results do not show the expected reentrant behavior from a phase separated suspension to a

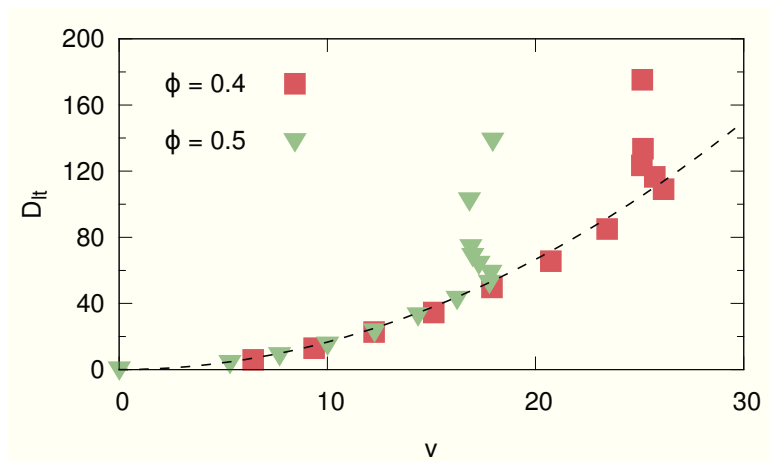


Figure 3.12: Long-time diffusion coefficient D_{lt} as a function of the effective swimming speed v at packing fractions $\phi = 0.4$ and $\phi = 0.5$. The dashed line corresponds to the approximation $D_{lt} \approx v^2/(2D_r)$ since $v^2/(2D_r) \gg D$ for sufficiently large v .

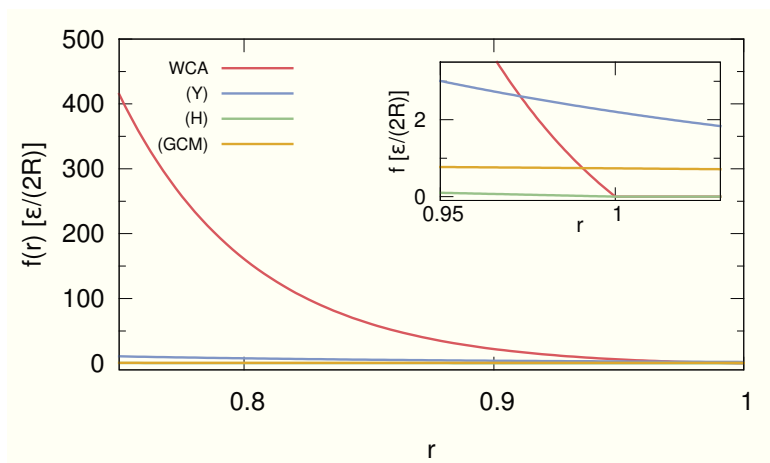


Figure 3.13: Magnitude of the force $f(r) = |u'(r)|$ acting on a pair of particles as a function of distance r for the four potentials WCA from Sec. 2.4, (Y), (H) and (GCM). The inset shows the behavior for interparticle distances around $r = 1$.

stable fluid as the swimming speed increases. This has not been simulated since this transition would occur at a very high Péclet number due to the very strong ($\epsilon = 100$) and steep ($\propto r^{-12}$) pair potential, which requires very small time steps for the integration, resulting in a too long computational time to achieve reasonable results in steady state. In order to show this phenomenon three further pair potentials are employed: harmonic interaction (H) if particles overlap

$$u(r) = \begin{cases} \epsilon \left(\frac{r}{2R} - 1\right)^2 & (r \leq 2R) \\ 0 & (r > 2R), \end{cases} \quad (3.66)$$

the Gaussian core model (GCM) [167, 168]

$$u(r) = \epsilon e^{-(r/(2R))^2}, \quad (3.67)$$

and a Yukawa potential (Y) known from the DLVO theory [169, 170]

$$u(r) = \epsilon \frac{e^{-\kappa(r-2R)-2R}}{r} \quad (3.68)$$

with inverse screening length $\kappa = 5(2R)^{-1}$. In Fig. 3.13 the four different pair potentials are compared in terms of the magnitude of the force $f(r) = |u'(r)|$ acting between particles at center-to-center distance r . Indeed, one observes that the WCA potential is significantly stronger than the three potentials mentioned above, while the pair interaction modeled by (Y) and (GCM) is more long ranged and particles do repel each other beyond overlap, see inset of Fig. 3.13.

Another goal besides showing that phase separation is generic, is also to demonstrate the temperature dependence of the phase transition, which has been illustrated in Fig. 3.7, especially the reentrant behavior into a stable suspension. Therefore the temperature T is treated as a controllable parameter and only in this section the units for physical quantities change, yielding the interaction strength ϵ as the unit of energy and $(2R)^2/(\mu_0\epsilon)$ as the unit of time, while $2R$ is still the unit of length. In these units, Brownian dynamics simulations have been performed with a time step $\Delta t = 0.05$. Consequently, this section decouples completely from the particle model introduced in Sec. 2.4, in particular because the rotational diffusion coefficient is treated as a controllable parameter and is fixed to $D_r = 3 \cdot 10^{-5}$ instead of using the Stokes-Einstein-Debye relation. Starting from an equilibrated passive fluid with randomly distributed particle orientations, the swimming motion of the particles is turned on and after a relaxation time of $t_r = 100000$, data has been collected for a total simulation time $t = 250000$.

Similar to the WCA model, $N = 4900$ particles have been simulated at various swimming speeds $v_0 < 1$ and packing fractions: (H) $\phi = 0.7$, (GCM) $\phi = 0.091$ and (Y) $\phi = 0.2$. Here it is indeed important to point out that the numerical values for v_0 might appear small, but needs to be seen relatively to both the potential strength $f(r)$ and diffusion. At first, the systems are simulated at $k_B T = 0$, where Fig. 3.14(a) shows the behavior of the static structure factor

$$S(\mathbf{q}) = \frac{1}{N} \left| \sum_{i=1}^N e^{-i\mathbf{q}\mathbf{r}_i} \right| \quad (3.69)$$

at the considered free swimming speeds with \mathbf{q} being the wave vector. One observes a diverging behavior for $q \rightarrow 0$, indicating density fluctuations at large length scales, but also non-diverging graphs are shown, which correspond to a stable system. In Fig. 3.14(b) the force imbalance coefficient ζ is plotted as a function of the free swimming speed v_0 . Since for $T = 0$ particles do not diffuse, i.e., $D = 0$, the minimal velocity for the instability to occur is $v_* = 0$, which is the reason that for all three systems the first measured point at $v_0 = 0.01$ already corresponds to a phase separated system where the static structure factor diverges (closed symbols). In accordance to the WCA model, there surely exists a critical velocity for the phase transition, but its numerical value in these units is very low and determining its value is not the goal of this section. For larger swimming speeds all three systems show a reentrant behavior where the measured force imbalance coefficient leaves the unstable region, which coincides quite well with measuring a non-diverging static structure factor (open symbols). In Fig. 3.14(c) and (d) two snapshots of the simulation box of the harmonic system (H) are provided, which show the corresponding states of a phase separated and a homogeneous fluid after reentering the stable region. Particles are colored according to their persistence of motion quantified by

$$\alpha_i = \frac{\mathbf{e}_i(t) \cdot [\mathbf{r}_i(t + \Delta t) - \mathbf{r}_i(t)]}{v_0 \Delta t}, \quad (3.70)$$

which is 1 for a freely moving swimmer at $T = 0$ and -1 if a particle is being pushed in the opposite direction of its propulsion during the lag time Δt . This parameter reveals that particles within a cluster are mostly not able to keep their persistence motion due to the self-trapping mechanism in the dense aggregate, while the swimmers in the dilute region and stable suspension move quite persistent.

Now the system (H) is also considered at $k_B T = 0.01$ to qualitatively verify the consequences of Fig. 3.7, claiming that if DD_r increases, one needs a larger propelling force v_0 to achieve phase separation (already shown for the WCA model), but also that the velocity for reentering the stable region is reduced, which has not been investigated yet. Fig. 3.15 shows density maps of systems at $k_B T = 0$ and $k_B T = 0.01$ at various swimming speeds. The first observation is that, as expected, the system at $k_B T = 0$ is unstable for $v_0 = 0.01$ and the system at $k_B T = 0.01$ is stable at the same intrinsic swimming speed, but phases separate at $v_0 = 0.05$. Another observation is that the edge of the cluster is more fuzzy for $k_B T = 0.01$, which is due to the translational diffusion of the particles. If a propelling speed of $v_0 = 0.2$ is considered, the system at zero temperature is still phase separated, while the system at $k_B T = 0.01$ is quite homogeneous, which is a qualitative confirmation for the behavior of the critical velocity for reentering a stable region in the phase diagram.

3.3.5 Experimental results

Since the particle model is motivated by the experiment performed by the *2. Physikalisches Institut* at the University of Stuttgart, which has been explained in Sec. 2.4.1, it is essential to compare numerical and experimental results. Fig. 3.16(a) shows the

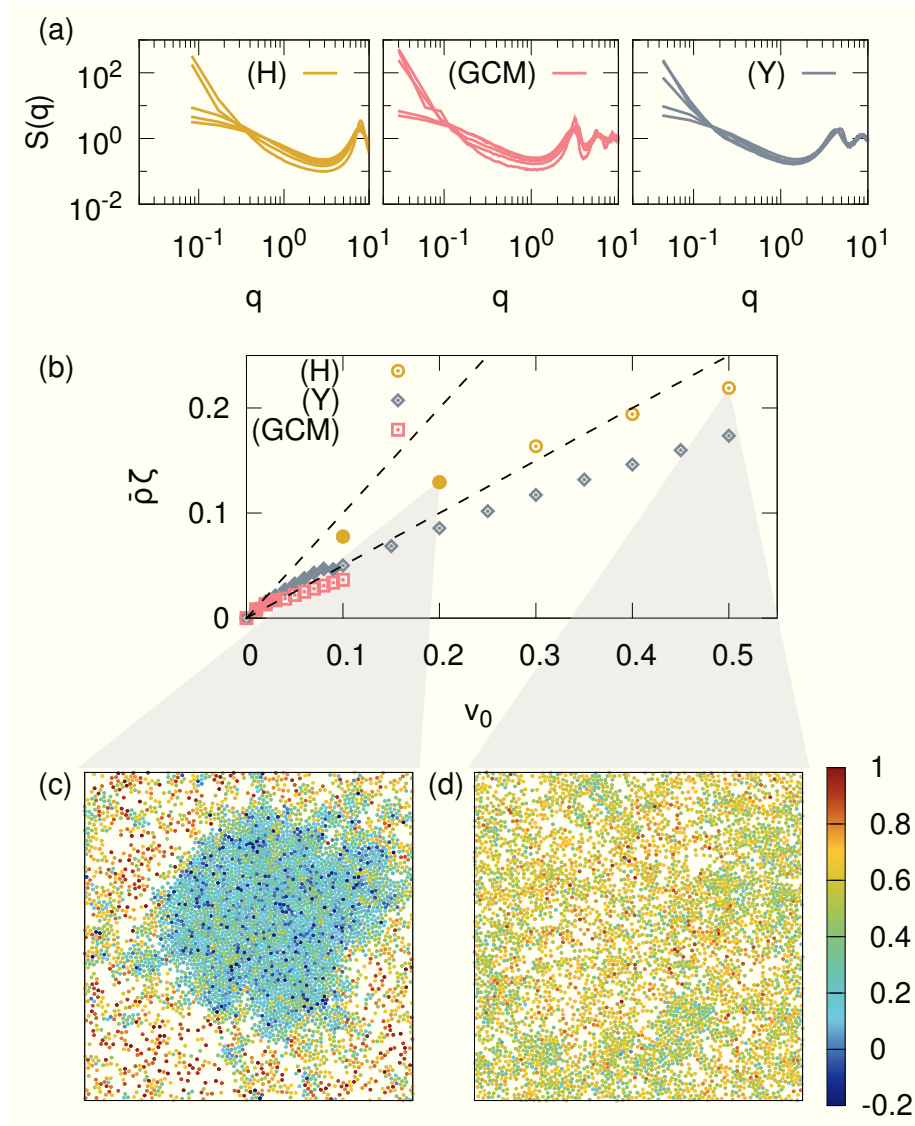


Figure 3.14: (a) Double-logarithmic plot of the static structure factor $S(|\mathbf{q}| = q)$ as a function of the magnitude q of the wave vector for the three systems (H), (GCM) and (Y). (b) Reduced force imbalance coefficient ζ as a function of propelling speed v_0 . Closed symbols correspond to a diverging structure factor for $q \rightarrow 0$, while open symbols represent a non-diverging static structure factor, indicating a stable homogeneous system. (c) Snapshot of the simulation box of the system (H) at $v_0 = 0.2$ and (d) $v_0 = 0.5$. Particles are colored according to their persistence of motion given by the parameter α_i in Eq. (3.70).

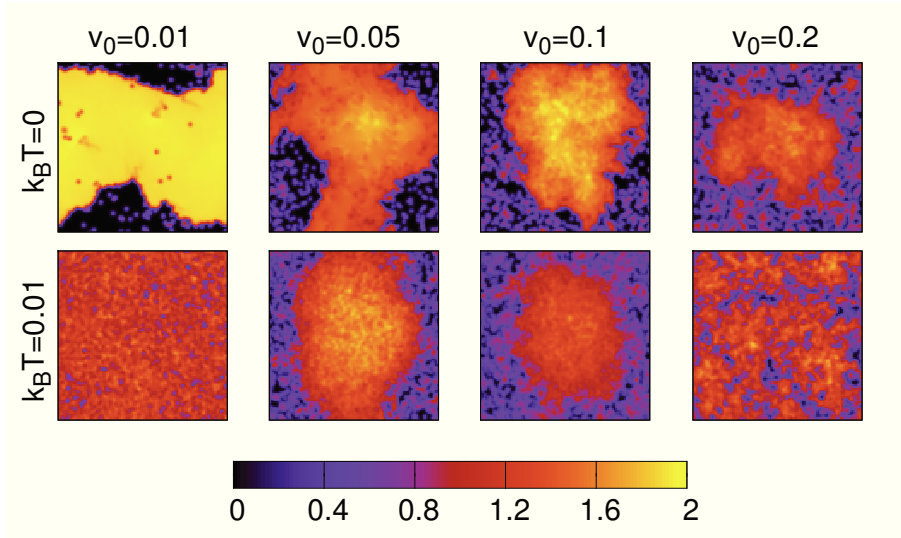


Figure 3.15: Snapshots of the density field $\rho(\mathbf{r})$ of the simulation box for system (H) at $k_B T = 0$ and $k_B T = 0.01$ for $v_0 = 0.01, 0.05, 0.1, 0.2$. In order to create the density field, the simulation box has been divided into 100×100 cells of side length l . Then, a single particle i is considered to have a density distribution given by the normalized radial Gaussian function $e^{-(\mathbf{r}-\mathbf{r}_i)^2/(2\sigma^2)}/2\pi\sigma^2$ with $\sigma = l/\sqrt{2}$. For the considered packing fraction $\phi = 0.7$, this yields a typical width of the Gaussian function, which is comparable to the diameter $2R$ of the particle. Finally, the superposition of the density distributions of all particles are integrated in each cell and divided by the cell area l^2 , yielding the density in each cell. Here, the cells are colored according to their density normalized to the homogeneous density $\bar{\rho} \approx 0.891$.

relative size of the largest cluster in the system for both numerical and experimental data. However, like observable in Fig. 3.16(c), the experimental system does not show one single cluster like the simulation. This is simply due to the quasi-two dimensionality of the experimental setup, where colliding particles try to evade into the z -direction leading to clusters which are three dimensional objects. These clusters are very slow due to hydrodynamic effects near to the cells walls and are not able to join into one single cluster within the experimental time window. In order to continue it is assumed that the steady state is one single cluster and to calculate its size all clusters larger than $N/10$ have been added up where N is the number of particles in the monitored area. For $\phi = 0.36$ the critical velocity of the phase transition is in excellent agreement with the numerical result. On the other hand the experimental system shows a clear clustering transition at lower packing fractions which has not been observed in computer simulations. One reason for that could be the lack of hydrodynamic interactions between particles in the numerical model³.

The theoretical explanation for the mechanism responsible for the clustering leading to

³Later, a quasi-two dimensional study [171] has shown that including hydrodynamic interactions (squirmers model [172–174]) reveals clustering at smaller packing fractions than simulations neglecting hydrodynamic interactions.

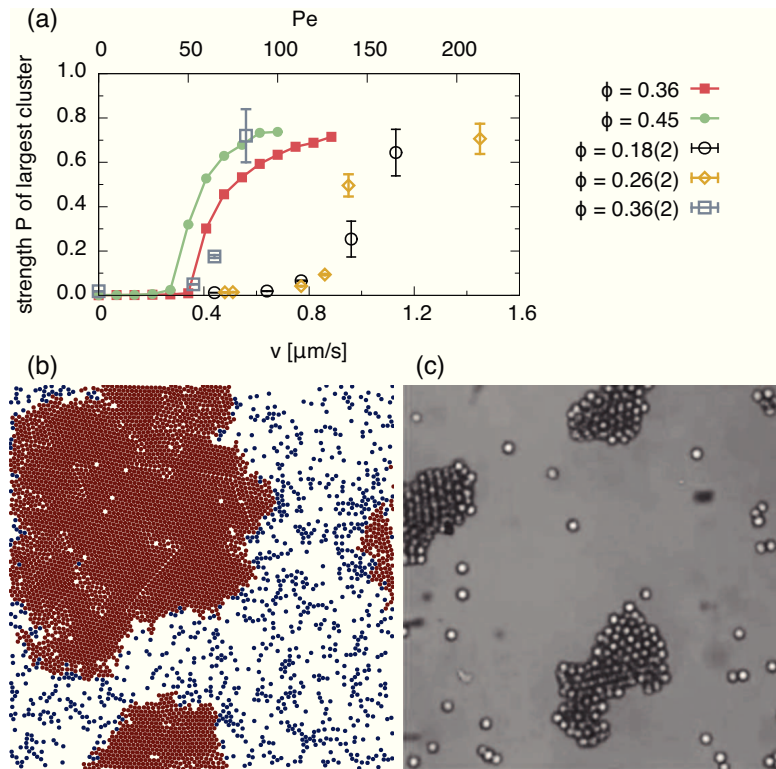


Figure 3.16: (a) Strength P of the largest cluster in the system as a function of physical propelling speed (lower x -axis) and Péclet number (upper x -axis). The closed symbols connected by a straight line are numerical results, while the open symbols correspond to experimental data. (b) Snapshot of the simulation box at $\phi = 0.5$ and $Pe = 100$ where red particles correspond to swimmers being part of the largest cluster. (c) Experimental snapshot at $\phi \simeq 0.25$ and $v \simeq 1.45 \mu\text{m/s}$.

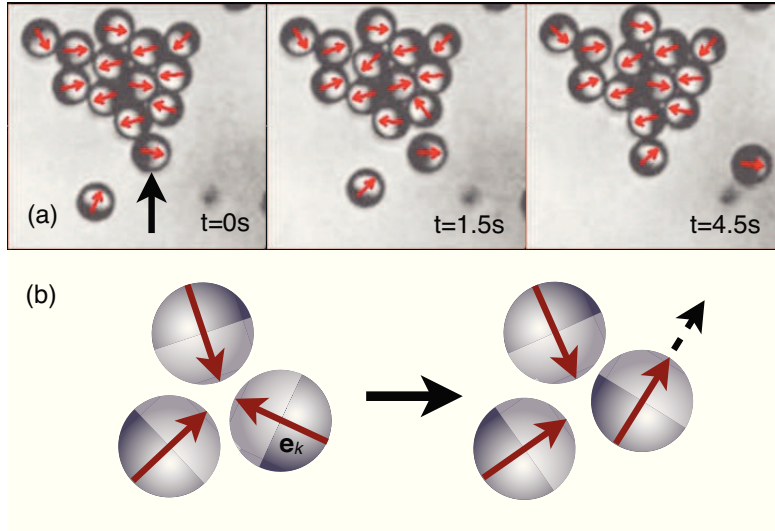


Figure 3.17: Consecutive close-ups of a cluster observed in the experiment. The red arrows indicate the particle orientation which has been able to detect by resolving the graphite cap of the particle and mostly point inward the cluster. In addition, the particle indicated by the black arrow at $t = 0s$ will leave the cluster, while it is replaced by another particle, which demonstrates that particles are interchanged between the two phases. (b) Sketch of the self-trapping mechanism where for a stable suspension particles need to reorient before further particles can join the cluster.

phase separation is that particles trap (block) each other due to the persistent propulsion, which has to be validated at least qualitatively in the experiment. Fig. 3.17(a) shows the orientational configuration of a cluster observed in the experiment, clearly showing that particles point inward the small cluster and thus block other particles trying to leave the cluster. Another aspect shown in Fig. 3.17(a) is that a particle at the edge of the cluster leaves the cluster due to reorientation, but is then replaced by another particle coming from the dilute region of the system. This qualitatively confirms the numerical result that particles are interchanged between the phases, leading to a growing long-time diffusion coefficient D_{lt} as the free propelling speed v_0 increases while the effective swimming speed v saturates (cf. Fig. 3.12).

3.4 Conclusion

In conclusion, a theoretical framework has been derived from first principles, which describes the onset of the instability leading to a phase separation in active systems restricted to two dimensions where hydrodynamic interactions have been neglected. The calculation yields an equation of motion for the one-particle density with an effective swimming speed $v = v_0 - \bar{\rho}\zeta$ which includes both the intrinsic propulsion speed v_0 and

the slowdown due to particle interactions represented by the so-called force imbalance coefficient ζ . After deriving the temporal evolution equations for the density field and orientational field, small perturbations from the homogeneous solution are considered whose behavior is analyzed via a linear stability analysis. This yields a region determined by the value of ζ where the system is unstable regarding small density perturbations. The analysis has been supported by Brownian dynamics simulations which show a transition from a homogeneous suspension to a phase separated system containing one big dense cluster surrounded by a dilute gas phase. After quantifying this transition with an appropriate order parameter, the prediction for an unstable system via the force imbalance coefficient ζ coincides quite well with the critical velocities of the transition estimated via a finite size scaling analysis considering the critical exponents of the two dimensional Ising model.

In order to demonstrate that this is a generic phenomenon, three further pair potentials have been applied where the temperature is treated as a controllable parameter. At $T = 0$ the prediction of the onset of the instability in terms of the force imbalance coefficient is confirmed but also a reentrance into the stable regime for higher propelling forces is observed which is supported by a non-diverging behavior of the static structure factor for $q \rightarrow 0$. For $T > 0$ diffusion is present, causing a stronger critical propulsion speed necessary for the instability to set in, but also a lower propulsion for which the suspension reenters into the stable state, which has also been reported by the developed theory.

The comparison to the experimental setup introduced in Sec. 2.4.1 shows excellent agreement regarding the critical propulsion speed at packing fraction $\phi = 0.36$, which is remarkable considering the minimal model applied. However, in the experiment the suspension does also evolve clusters at lower densities. The self-trapping mechanism and the particle interchange between the phases has been confirmed qualitatively in the experiment by identifying the graphite hemisphere, i.e., the orientation of the particles. There is still a lot of work left to fully understand the phase separation of active pure repulsive particles. One goal is to understand why experiments show clustering behavior at lower densities than simulations based on the minimal model introduced in Sec. 2.4. The key to this problem might be the behavior of self-propelled particles near walls [114], but more important the inclusion of hydrodynamic interactions between particles and also hydrodynamic interactions between particles and the walls of the confining cell. This has already been studied considering the squirmer model [171]. But the scientific community is still debating, if the squirmer model, which prescribes the solvent velocity on the particles surface, is appropriate to model for example diffusiophoretic swimmers. Nevertheless, the role of dimensionality [175] is also an important point since simulations considering a two dimensional fluid instead of a quasi-2d setup show a suppression of the phase separation if hydrodynamic interactions are present [176]. Also mixtures of active and passive particles have recently been studied [177] and do certainly deserve more attention in the context of phase separation. From the experimental point of view it would be desirable to study three dimensional systems, since it has already been done numerically [141, 175]. A more interesting point for experimentalists is to quantify how artificial swimmers behave within a cluster due to shared *fuel* consumption, e.g., over-

lapping demixing zones in the experiment of publication 1. From the numerical point of view, it would be desirable to avoid simulations to improve time efficiency. This could be done by applying an appropriate closure for the BBGKY hierarchy mentioned in Sec. 3.1.1 and calculate the two dimensional pair correlation function directly via a numerical algorithm without being forced to simulate a sufficiently large system. A similar work has already been done for a binary mixture of particles driven in opposite directions [150] where the triplet correlation function has been approximated via the Kirkwood superposition approximation [178]. If this is extended to the system considered in this work, a numerical program would be achievable which only needs the pair potential $u(r)$, the free propulsion speed v_0 and the packing fraction ϕ as input and then calculates whether the suspension is stable or not in a much more quicker way than a simulation could ever do.

Chapter 4

Effective Cahn-Hilliard description

In equilibrium phase separation has been studied in detail for about 50-60 years and is quite well understood [179,180]. It has been shown that only attractive interactions can lead to phase separation in monodisperse systems at equilibrium. This can be explained introducing the free (Helmholtz) energy $F = U - TS$ of the system with U being the total internal energy (potential energy), T the temperature and S the entropy of the system. Any realistic particle pair potential should fulfill $u(r \rightarrow \infty) = 0$ and thus $u(r) > 0$ for any r in case of a pure repulsive potential, yielding $U > 0$ for any spatial configuration. A system always tries to minimize its free energy and therefore tries to maximize its entropy S . Since the entropy is a quantity measuring the number of different possibilities to realize one specific system configuration, an inhomogeneous system is always unfavored by the entropy part and in case of pure repulsive particles even by the internal energy. A very famous example is the model of hard spheres, comparable to billiard balls, which do not interact, but particles are also not able to interpenetrate each other. This yields $U = 0$ for all allowed configurations so that the phases of such a system are always homogeneous and purely determined by the entropy S , i.e., the density of the system, which leaves the temperature T as a scaling parameter [181]. This picture changes if attractive interactions are present which are strong enough to overcome the entropy part of the free energy and lead to an inhomogeneous or macroscopically phase separated system. In this case, the mechanism behind the phase separation is well understood in terms of the free energy F as a function of the density. Below¹ the critical temperature T_c it is assumed that this function exhibits two minima, see Fig. 4.1, which of course favors phase separation to minimize the total free energy. A system with an initial density lying within the region of negative curvature corresponds to the scenario of spinodal decomposition, where the system is unstable against smallest density fluctuations and immediately starts to separate into two phases of different densities. The values of these densities are determined by the well-known common tangent construction, which is the

¹In principle, there also exist mixtures of different composites which start to phase separate above a lower critical solution temperature (LCST). However, for one component systems phase separating into regions of different densities, this is not the case.

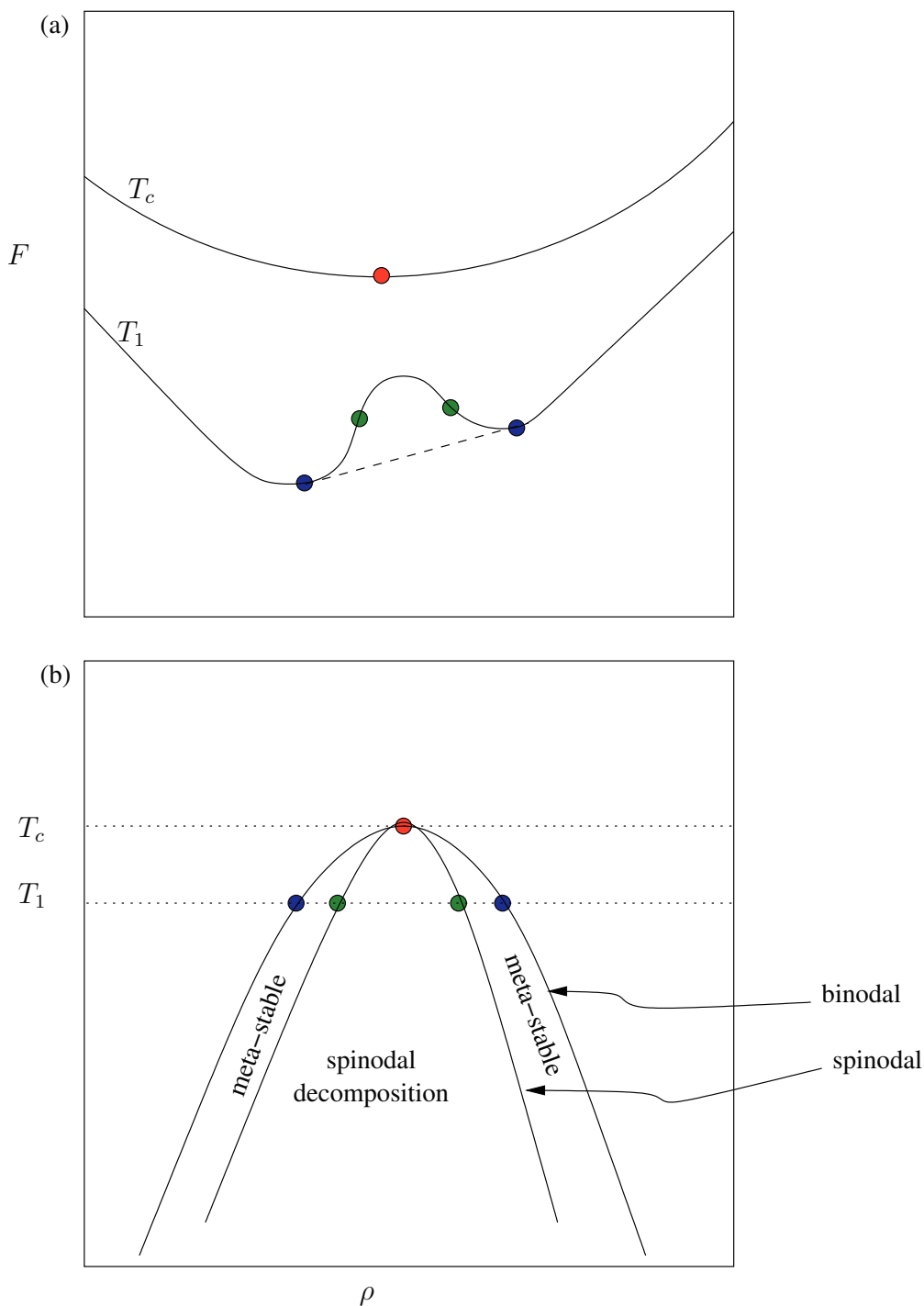


Figure 4.1: (a) Sketch of the free energy F as a function of density ρ for a system at temperature $T = T_c$ and $T = T_1 < T_c$. The red points corresponds to the critical point. Between the two inflection points (green) the curvature is negative, corresponding to the scenario of spinodal decomposition. The common tangent (dashed line) is constructed so that it is the lowest straight line steadily connecting the two parts of the energy with positive curvature. The blue points are these connection points, marking the meta-stable regime. (b) Phase-diagram in the $\rho - T$ plane, where the procedure illustrated in (a) needs to be performed for each temperature. Then the colored points are marked along the corresponding temperature, here shown by the dotted lines. Following this, the spinodal regime and a meta-stable regime is constructed. Above the critical temperature the system always is homogeneous and stable.

lowest straight line steadily connecting the two parts of positive curvature, see Fig. 4.1. This construction is necessary for the curvature to stay positive since

$$-p = \left. \frac{\partial F}{\partial V} \right|_{T,N} \quad (4.1)$$

where the vertical line with indices denotes the derivative at constant temperature and constant particle number. If the common tangent construction is not performed the negative curvature would lead to a pressure increase if the volume V increases, which is clearly unphysical. One should also note that in a phase separated system, the densities of the two phases do not correspond to the actual minima, but are the connecting points of the common tangent on the free energy function and form the boundary of the meta-stable region, i.e., the binodal. At constant temperature (equal temperature for both phases) these points correspond to a constant (equal) chemical potential

$$\mu = \left. \frac{\partial F}{\partial N} \right|_{T,V} \quad (4.2)$$

and equal bulk pressure of the two phases. The meta-stable region is characterized by the fact, that a system lying within that region needs a sufficiently large fluctuation, demonstrative an activation energy, to start phase separation. This is in direct contrast to the region of spinodal decomposition where phase separation starts spontaneously. Any system with its initial density being on the common tangent does eventually separate into two phases with their sizes being in accordance to the lever rule: a system being initially on the common tangent near the left minima will phase separate into a very large dilute phase and a very small dense phase. At sufficient high temperatures $T > T_c$, the free energy has always positive curvature, i.e., only one minimum, and the system is stable and always homogeneous, see Fig. 4.1 for an illustrative summary of the construction of the phase diagram. The temperature T_c at which the free energy changes to only having one minima is the critical temperature at which the two phases have equal density. The behavior of suspensions near the critical point is a highly debated topic being investigated by many different approaches [182–184].

Unfortunately, for self-propelled systems, which are constantly driven out of equilibrium, such a construction is not possible due to the lack of a definition for the free energy. But, considering the phase separation scenario, it would be a striking achievement to find an equilibrium system with attractive interactions, which shows equivalent behavior like the non-equilibrium self-propelled repulsive system. There exist several phenomenological approaches for such an effective mapping [133, 185–190], but not derived from first principles and not all being able to be written in the form of a free energy functional $\mathcal{F}[\rho(\mathbf{r})]$. This is desirable since in equilibrium the density functional theory (DFT), which has been developed during the 1960's and 1970's [191–194], can derive all thermodynamic properties of a system only by the knowledge of such an free energy functional. Even the dynamical density functional theory (DDFT) [195] could be applicable to analyze the temporal evolution of the local density according to

$$\frac{k_B T}{D} \partial_t \rho = \nabla \rho \nabla \frac{\delta \mathcal{F}}{\delta \rho}, \quad (4.3)$$

where $\delta\mathcal{F}/\delta\rho$ represents the functional derivative of \mathcal{F} with respect to the density field $\rho(\mathbf{r}, t)$. The existence of an effective free energy functional would open a completely new access to self-propelled systems.

This chapter is mainly based on publication 3. In the first part, a mean-field description leading to an effective free energy is derived from first principles, which holds near the transition line where phase separation sets in spontaneously. The evolution equation for the density perturbation which implies the existence of an effective free energy function is recognized as the Cahn-Hilliard equation. In consistency with the effective Cahn-Hilliard description, the instability line (a possible spinodal) is constructed in the phase diagram and compared to numerical results. In addition computer simulations reveal that systems below a critical density show indication of a discontinuous transition and a significant hysteresis. This behavior may correspond to the scenario of a meta-stable region illustrated in Fig. 4.1 and is also shown to be already contained in the effective Cahn-Hilliard description. Finally, a possible binodal is obtained from the coexisting densities measured in computer simulations and compared to the spinodal constructed out of the theory.

4.1 Effective free energy functional

The analysis starts with the effective hydrodynamic equations for the density field $\rho(\mathbf{r}, t)$ and the orientational field $\mathbf{p}(\mathbf{r}, t)$ derived in Sec. 3.2.1, i.e.,

$$\partial_t \rho = -\nabla \cdot [v\mathbf{p} - D\nabla\rho], \quad (4.4)$$

$$\partial_t \mathbf{p} = -\frac{1}{2}\nabla(v\rho) + D\nabla^2\mathbf{p} - D_r\mathbf{p}. \quad (4.5)$$

Again, in analogy to Sec. 3.2.2, the equations are simplified by replacing v with the local effective swimming speed $v_l = v_0 - \rho\zeta$, while the force imbalance coefficient ζ is treated as a controllable parameter independent of the density. In addition, to simplify the equations, $1/D_r$ is chosen as the unit of time and $\sqrt{D/D_r}$ as the unit of length (only for the presentation of the coupled equations) and both fields are renormalized with the homogeneous density, giving $\rho \rightarrow \bar{\rho}(1 + \delta\rho)$ and $\mathbf{p} \rightarrow \bar{\rho}\mathbf{p}$. Altogether this yields the dimensionless set of equations

$$\partial_t \delta\rho = -\alpha\nabla \cdot \mathbf{p} + \nabla^2\delta\rho + 4\xi\nabla \cdot (\mathbf{p}\delta\rho) \quad (4.6)$$

$$\partial_t \mathbf{p} = -\beta\nabla\delta\rho + \nabla^2\mathbf{p} - \mathbf{p} + 4\xi\delta\rho\nabla\delta\rho, \quad (4.7)$$

with the dimensionless coefficients

$$\xi = \frac{\bar{\rho}\zeta}{v_*}, \quad \alpha = 4\left(\frac{v_0}{v_*} - \xi\right), \quad \beta = 2\left(\frac{v_0}{v_*} - 2\xi\right), \quad (4.8)$$

where $v_* = 4\sqrt{DD_r}$ is again the minimal velocity needed for an instability. By neglecting the nonlinear terms in Eqs. (4.6) and (4.7), given respectively by the last term, and

considering the Fourier transforms $\delta\tilde{\rho}$ and θ of $\delta\rho$ and $\nabla \cdot \mathbf{p}$ respectively, i.e.,

$$(\delta\tilde{\rho}, \theta) = \frac{1}{(2\pi)^{3/2}} \int d\mathbf{r} e^{-i\mathbf{q}\mathbf{r}} \int dt e^{-i\omega t} (\delta\rho, \nabla \cdot \mathbf{p}), \quad (4.9)$$

one rewrites Eqs. (4.6) and (4.7) in Fourier space, yielding

$$i\omega\delta\tilde{\rho} = -\alpha\theta - q^2\delta\tilde{\rho} \quad (4.10)$$

$$i\omega\theta = \beta q^2\delta\tilde{\rho} - q^2\theta - \theta. \quad (4.11)$$

Solving this set of equations for ω gives

$$\omega = i(q^2 + \frac{1}{2}) \pm \frac{1}{2}\sqrt{4\alpha\beta q^2 - 1}. \quad (4.12)$$

Again, the temporal evolution of the density perturbation $\delta\rho$ is the point of interest and is known from the Fourier transform of $\delta\tilde{\rho}$. That implies $\delta\rho \sim e^{i\omega t}$, while \sim does not denote proportionality, but rather a general dependency. Now the dispersion relation $\sigma(q) = i\omega$ can be defined, which quantifies the growth rate of the density perturbation as a function of the magnitude q of the wave vector and is given by

$$\sigma_{\pm}(q) = -\frac{1}{2} - q^2 \pm \frac{1}{2}\sqrt{1 - 4\alpha\beta q^2}. \quad (4.13)$$

If $\sigma(q) > 0$, a small density perturbation grows exponentially, which is only possible for the plus sign in Eq. (4.13). Similar to the previous chapter, small wave vectors (large length scales) are considered, which allows to approximate the square root according to $\sqrt{1-x} \approx 1 - x/2$ for $x \ll 1$. Altogether the relevant growth rate is written as

$$\sigma(q) \equiv \sigma_+(q) = -\frac{1}{2} - q^2 + \frac{1}{2}\sqrt{1 - 4\alpha\beta q^2} \approx -(1 + \alpha\beta)q^2, \quad (4.14)$$

yielding $1 + \alpha\beta < 0$ as condition for an unstable suspension. So the onset of the instability is given by $1 + \alpha\beta = 0$, which yields in combination with Eq. (4.8) the condition for the reduced imbalance coefficient

$$\xi_{\pm} = \frac{3v_0}{4v_*} \pm \frac{1}{4}\sqrt{\left(\frac{v_0}{v_*}\right)^2 - 1}. \quad (4.15)$$

Since nonlinear terms have been neglected this is equivalent to the result obtained in Sec. 3.2.2. However, as discussed, values above ξ_+ are unphysical ($v < 0$), so that, coming from a stable system, the onset of the instability is given by the minus sign in Eq. (4.15), i.e.,

$$\xi_c = \frac{3v_c}{4v_*} - \frac{1}{4}\sqrt{\left(\frac{v_c}{v_*}\right)^2 - 1}, \quad (4.16)$$

where ξ_c and v_c are the critical values of the reduced force imbalance coefficient and free swimming speed on the transition line.

The crucial point of this chapter is considering an initial perturbation of the critical velocity, i.e., $v_0 = v_c(1 + \epsilon)$ with $\epsilon > 0$, which corresponds to a small quench of depth ϵ into the instability region coming from the transition line where $v_0 = v_c$ and $\xi = \xi_c$. According to the exact relation of Eq. (4.14), the wave vector q_c for which the growth rate of an initial density perturbation is maximal, i.e., the wave vector dominating an initial instability, is given by

$$q_c = \frac{1}{2} \sqrt{(\alpha\beta)^{-1} - \alpha\beta}. \quad (4.17)$$

Now the coefficients α and β are considered as functions of the free swimming speed v_0 . According to this, $\alpha(v_0)$ and $\beta(v_0)$ are expanded near the transition line in linear order of ϵ , i.e.,

$$\alpha = \alpha(v_0 = v_c) + (v_0 - v_c) \left. \frac{\partial \alpha}{\partial v_0} \right|_{v_0=v_c} + \dots \quad (4.18)$$

$$= \alpha_0 + \epsilon \alpha_1 + \dots \quad (4.19)$$

with $\alpha_0 \equiv \alpha(v_0 = v_c)$ and $\alpha_1 \equiv v_c \left. \frac{\partial \alpha}{\partial v_0} \right|_{v_0=v_c}$, while the expansion for β is obtained in an analogous way. According to Eq. (4.17), the critical wave vector is now given by

$$q_c = \frac{1}{2} \sqrt{\frac{1}{(\alpha_0 + \epsilon \alpha_1)(\beta_0 + \epsilon \beta_1)} - (\alpha_0 + \epsilon \alpha_1)(\beta_0 + \epsilon \beta_1)} \quad (4.20)$$

$$= \frac{1}{2} \sqrt{\frac{1}{\alpha_0 \beta_0 + \epsilon \alpha_0 \beta_1 + \epsilon \alpha_1 \beta_0 + \epsilon^2 \alpha_1 \beta_1} - \alpha_0 \beta_0 + \epsilon \alpha_0 \beta_1 + \epsilon \alpha_1 \beta_0 + \epsilon^2 \alpha_1 \beta_1} \quad (4.21)$$

$$\stackrel{\mathcal{O}(\epsilon)}{\simeq} \frac{1}{2} \sqrt{\frac{1}{\epsilon \sigma_1 - 1} - \epsilon \sigma_1 + 1} \quad (4.22)$$

$$\simeq \frac{1}{2} \sqrt{-2\epsilon \sigma_1} \propto \sqrt{\epsilon}, \quad (4.23)$$

where $\alpha_0 \beta_0 = -1$ and the approximation $(1 - x)^{-1} \approx 1 + x$ for $x \ll 1$ and $x > 0$ has been used, $\sigma_1 \equiv \alpha_0 \beta_1 + \alpha_1 \beta_0 < 0$ has been defined and only linear terms in ϵ have been considered. Inserting the α and β expansions into Eq. (4.14), the growth rate of the critical wave vector reads

$$\sigma(q_c) \approx -(1 + \alpha\beta)q_c^2 \quad (4.24)$$

$$\stackrel{\mathcal{O}(\epsilon)}{\simeq} -\epsilon \sigma_1 q_c^2 \propto \epsilon^2. \quad (4.25)$$

Following these scaling laws for the critical wave vector the length and the time scale are rescaled with $1/\sqrt{\epsilon}$ and $1/\epsilon^2$ respectively, yielding $\partial_t \rightarrow \epsilon^2 \partial_t$ and $\nabla \rightarrow \sqrt{\epsilon} \nabla$. In addition, similar to the coefficients α and β , the fields $\delta\rho(\mathbf{r}, t)$ and $\mathbf{p}(\mathbf{r}, t)$ are expanded in integer powers of ϵ (approximated near the transition line), but truncated at second order, i.e.,

$$\delta\rho = \epsilon c + \epsilon^2 c^{(2)} + \dots, \quad (4.26)$$

$$\mathbf{p} = \sqrt{\epsilon} [\epsilon \mathbf{p}^{(1)} + \epsilon^2 \mathbf{p}^{(2)} + \dots], \quad (4.27)$$

while the orientational field is additionally scaled with $1/\sqrt{\epsilon}$ to avoid fractions in the exponents of ϵ for the evolution equation of the density field. The fields $c, c^{(2)}, \mathbf{p}^{(1)}, \mathbf{p}^{(2)}$ describe the perturbation of the homogeneous solutions for the density field and orientational field, but are connected with the corresponding order in the expansion of the total perturbation fields $\delta\rho$ and \mathbf{p} . Plugging in the expansions for $\delta\rho, \mathbf{p}, \alpha, \beta$ into Eqs. (4.6) and (4.7), the coupled evolution equations yield

$$\begin{aligned} \epsilon^3 \partial_t c + \epsilon^4 \partial_t c^{(2)} = & -\alpha_0 \epsilon^2 \nabla \cdot \mathbf{p}^{(1)} - \alpha_0 \epsilon^3 \nabla \cdot \mathbf{p}^{(2)} - \alpha_1 \epsilon^3 \nabla \cdot \mathbf{p}^{(1)} - \alpha_1 \epsilon^4 \nabla \cdot \mathbf{p}^{(2)} + \epsilon^2 \nabla^2 c \\ & + \epsilon^3 \nabla^2 c^{(2)} + 4\xi_c \epsilon \nabla \cdot [\epsilon^2 \mathbf{p}^{(1)} c + \epsilon^3 \mathbf{p}^{(1)} c^{(2)} + \epsilon^3 \mathbf{p}^{(2)} c + \epsilon^4 \mathbf{p}^{(2)} c^{(2)}] \end{aligned} \quad (4.28)$$

and

$$\begin{aligned} \epsilon^3 \partial_t \mathbf{p}^{(1)} + \epsilon^4 \partial_t \mathbf{p}^{(2)} = & -\epsilon \beta_0 \nabla c - \epsilon^2 \beta_0 \nabla c^{(2)} - \epsilon^2 \beta_1 \nabla c - \epsilon^3 \beta_1 \nabla c^{(2)} + \epsilon^2 \nabla^2 \mathbf{p}^{(1)} \\ & + \epsilon^3 \nabla^2 \mathbf{p}^{(2)} - \epsilon \mathbf{p}^{(1)} - \epsilon^2 \mathbf{p}^{(2)} \\ & + 4\xi_c [\epsilon^2 c \nabla c + \epsilon^3 c \nabla c^{(2)} + \epsilon^3 c^{(2)} \nabla c + \epsilon^4 c^{(2)} \nabla c^{(2)}]. \end{aligned} \quad (4.29)$$

Now, the equations are investigated from lowest to highest order in ϵ step by step, while the different orders are treated independently (multiple-scale analysis). In principle, the critical force imbalance coefficient ξ_c in Eqs. (4.28) and (4.29) needs to be replaced by its expansion in powers of ϵ , i.e., $\xi = \xi_c + \epsilon \xi_1$. But in the following only orders of ϵ are considered which would not include the coefficient ξ_1 , allowing one to directly replace its expansion by the lowest order term ξ_c in both equations. Collecting the lowest order terms in Eq. (4.28) (order ϵ^2) yields

$$0 = -\alpha_0 \nabla \mathbf{p}^{(1)} + \nabla^2 c, \quad (4.30)$$

while the terms in linear order of ϵ in Eq. (4.29) give

$$\mathbf{p}^{(1)} = -\beta_0 \nabla c. \quad (4.31)$$

Combining Eqs. (4.30) and (4.31) leads to

$$(1 + \alpha_0 \beta_0) \nabla^2 c = 0, \quad (4.32)$$

which reproduces the condition of the linear stability analysis given in Eq. (4.14), which has been derived considering the very onset of the instability at $v_0 = v_c$, i.e., $\epsilon = 0$, and is therefore a consistent result. Gathering terms of the next order in Eqs. (4.28) (ϵ^3) and (4.29) (ϵ^2) reads respectively

$$\partial_t c = -\alpha_0 \nabla \cdot \mathbf{p}^{(2)} - \alpha_1 \nabla \cdot \mathbf{p}^{(1)} + \nabla^2 c^{(2)} + 4\xi_c \nabla \cdot (c \mathbf{p}^{(1)}) \quad (4.33)$$

$$0 = -\beta_0 \nabla c^{(2)} - \beta_1 \nabla c + \nabla^2 \mathbf{p}^{(1)} - \mathbf{p}^{(2)} + 4\xi_c c \nabla c. \quad (4.34)$$

Solving Eq. (4.34) for $\mathbf{p}^{(2)}$ and plugging this result into Eq. (4.33) one notices, that the terms consisting $c^{(2)}$ cancel out and one gets

$$\partial_t c = \alpha_0 \beta_1 \nabla^2 c - \alpha_0 \nabla \cdot (\nabla^2 \mathbf{p}^{(1)}) - 4\alpha_0 \xi_c \nabla \cdot (c \nabla c) - \alpha_1 \nabla \cdot \mathbf{p}^{(1)} + 4\xi_c \nabla \cdot (c \mathbf{p}^{(1)}). \quad (4.35)$$

Plugging in the result given by Eq. (4.31) into Eq. (4.35) gives

$$\partial_t c = \sigma_1 \nabla^2 c - \nabla^4 c - 2g \nabla \cdot (c \nabla c) = \nabla^2 \frac{\delta \mathcal{F}}{\delta c}, \quad (4.36)$$

where $g \equiv 2\xi_c(\alpha_0 + \beta_0) \geq 0$ has been defined and the free energy functional $\mathcal{F}[c]$ is introduced, which is written as

$$\mathcal{F}[c] = \int d\mathbf{r} \left[\frac{1}{2} |\nabla c|^2 + \underbrace{\frac{1}{2} \sigma_1 c^2 - \frac{1}{3} g c^3}_{f(c)} \right] \quad (4.37)$$

and $\delta F/\delta c$ is the functional derivative with respect to c . Eq. (4.36) is recognized as the well-known Cahn-Hilliard equation [35] typically being used to study phase separation in equilibrium. The first term in the integral of the free energy functional is the contribution due to local inhomogeneities while

$$f(c) = \frac{1}{2} \sigma_1 c^2 - \frac{1}{3} g c^3 \quad (4.38)$$

is the free energy density of the homogeneous system with the corresponding density, also called bulk free energy. The existence of the free energy functional according to Eq. (4.36) is the main result of this chapter. In App. A.2 a proof is shown that Eq. (4.36) can indeed be derived from the free energy functional $\mathcal{F}[c]$. The very first observation of the bulk free energy given by Eq. (4.38) is the absence of the customary stabilizing c^4 term. Physically, it is necessary to ensure $f(c) \rightarrow \infty$ for $c \rightarrow \pm\infty$, which hinders the suspension to collapse into one single point of infinite density. Practically, the collapse is forbidden due to volume exclusion, which is theoretically modeled by the divergence of the pair potential. Since the expansion has been performed on a coarse grained level on length scales, which are much larger compared to the typical particle size, the repelling nature of the particles is not included, which is the reason for the missing stabilization term. In App. A.3 a lower order expansion is presented where also fractional orders of ϵ are included. It is shown, that, in the vicinity of the critical speed $v_c = v_*$, the bulk free energy takes the general form

$$f(c) = \frac{1}{2} \sigma_1 c^2 + \frac{1}{4} \kappa c^4 \quad (4.39)$$

with $\kappa > 0$ being the positive coefficient of the stabilizing term. This form is commonly known as the symmetric Ginzburg-Landau free energy density [196].

4.1.1 Free energy coefficients

The free energy density $f(c)$ given by equation Eq. (4.38) contains two coefficients, σ_1 and g . The latter one has already been defined as $g \equiv 2\xi_c(\alpha_0 + \beta_0)$ and can also be

rewritten as

$$g(u) = 2\xi_c(\alpha_0 + \beta_0) \quad (4.40)$$

$$= 4\xi_c(3u - 4\xi_c) \quad (4.41)$$

$$= 1 - u^2 + 3u\sqrt{u^2 - 1} \quad (4.42)$$

$$\geq 0 \quad (4.43)$$

where $u = v_c/v_*$ is the reduced critical velocity. Since $v_* = 4\sqrt{DD_r}$, the coefficient g can be directly calculated in simulations by measuring D , the long-time diffusion coefficient of the corresponding passive suspension. The analytical expression of the remaining coefficient is given by

$$\sigma_1(u) = \alpha_0\beta_1 + \alpha_1\beta_0 \quad (4.44)$$

$$= -2 + 2g(u)[1 - u\gamma(u)], \quad (4.45)$$

with the dimensionless parameter γ defined as

$$\gamma \equiv \frac{v_*}{\xi_c} \left. \frac{\partial \xi}{\partial v_0} \right|_{v_0=v_c}, \quad (4.46)$$

which is the relative slope of the force imbalance coefficient at the onset of the instability. Unfortunately, the numerical calculation of this coefficient is very difficult so that one rather needs to think of an appropriate approximation as it will be done in Sec. 4.2.2.

4.2 Phase diagram

4.2.1 Numerical results

In computer simulations the phase separation scenario is described by the order parameter P , the mean relative size of the largest cluster in the system. A system is considered to be phase separated if $P \geq 0.1$. The resulting phase diagram is not too sensitive to the choice of threshold, see App. A.4. A crystalline suspension has been identified by evaluating the six-fold order parameter

$$\Psi_6 = \left\langle \left| \frac{1}{N} \sum_{i=1}^N q_6(i) \right|^2 \right\rangle, \quad (4.47)$$

where

$$q_6(i) = \frac{1}{6} \sum_{j \in \mathcal{N}(i)} e^{6i\theta_{ij}} \quad (4.48)$$

with $\mathcal{N}(i)$ are the six nearest neighbors of particle i and θ_{ij} is the angle enclosed between the connection vector \mathbf{r}_{ij} and an arbitrary fixed axis. This order parameter is 1 for a

perfect hexagonal crystal, while it is 0 for a spatially unordered suspension. According to previous studies for self-propelled particles [145] but also for an equilibrium Yukawa system [197], $\Psi_6 \simeq 0.45$ is chosen as a threshold to a crystalline (solid) suspension. An additional criterion is that the suspension has to be homogeneous, so that a phase separated suspension with a large and highly crystalline (but very dynamic) dense phase is not identified as a homogeneous hexagonal crystal. Altogether this yields $\phi_f \simeq 0.74$ as the freezing point of the suspensions. The complete phase diagram is shown later in Fig. 4.4 together with an analytical estimation of the instability line. The data points in this phase diagram have been carried out with the same simulation setup used in Chap. 3 ($N = 4900$ particles, relaxation time $t_r = 100$ starting from equilibrated passive fluid).

4.2.2 Instability line construction

The goal of this section is to demonstrate the construction of the instability line, in equilibrium referred to as the spinodal, starting from the effective Cahn-Hilliard-description. First, to be consistent with the theory developed, the effective free energy density missing the stabilizing c^4 term is considered

$$f(c) = \frac{1}{2}\sigma_1 c^2 - \frac{1}{3}g c^3. \quad (4.49)$$

In Fig. 4.2(a) the bulk free energy $f(c)$ is sketched in the instability region, where $\sigma_1 < 0$ holds, with and without the repelling nature of the particles. Also a possible common tangent construction is shown. However, only values $c < 0$ are considered since the expression Eq. (4.49) does only provide a minimum for that region. Nevertheless, this is sufficient to construct the instability line at densities considered in the computer simulations. Assuming a point (ϕ_1, v_1) is known being exactly on the instability line, increasing the swimming speed to $v_2 = v_1(1 + \epsilon)$, the theory predicts phase separation according to the bulk free energy density $f(c)$, see Fig. 4.2(a). The density corresponding to the inflection point of the bulk free energy should be on the instability line (spinodal) as well as the known point (ϕ_1, v_1) . The inflection point of $f(c)$ is given by $c^* = \sigma_1/(2g)$. The corresponding global density is $\rho^* = \rho_1(1 + \delta\rho^*)$ with ρ_1 being the density corresponding to ϕ_1 and the estimation up to linear order $\delta\rho^* = \epsilon c^*$. Now, in terms of packing fraction, another point on the instability line is known, given by $\phi_2 = \phi^* = \phi_1(1 + \epsilon c^*)$, see Fig. 4.2(b). This expression is now rewritten by inserting $\epsilon = v_2/v_1 - 1$ and $c^* = \sigma_1/(2g)$ yielding

$$\phi_2 = \phi_1 \left(1 + \left(\frac{v_2}{v_1} - 1 \right) \frac{\sigma_1}{2g} \right) \quad (4.50)$$

$$\Leftrightarrow \frac{\phi_2 - \phi_1}{v_2 - v_1} = \frac{\phi_1 \sigma_1}{v_1 2g}. \quad (4.51)$$

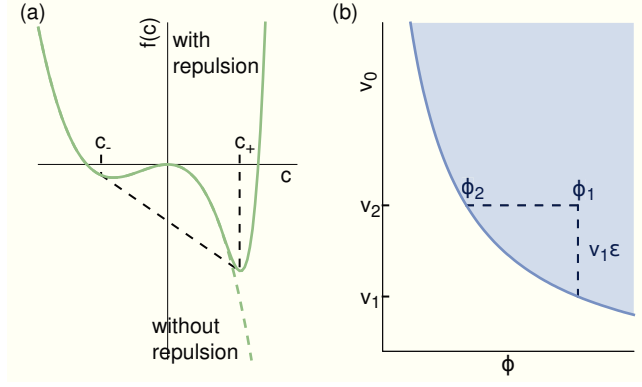


Figure 4.2: (a) Sketch of the free energy density $f(c)$ as a function of the rescaled density perturbation c . The solid line corresponds to the free energy density including repulsion of the particles, while the dashed line shows the result from the ϵ expansion which does not take particle repulsion into account. The black dashed line shows a sketch of the common tangent construction at the points c_{\pm} . (b) Demonstration of the derivation of Eq. (4.52) where from a known point (ϕ_1, v_1) the swimming speed is slightly increased to $v_2 = v_1(1 + \epsilon)$ to estimate the packing fraction ϕ_2 of the new inflection point of $f(c)$. The blue area represents the instability region.

By considering the limit $v_2 \rightarrow v_1$, one obtains the differential equation

$$\frac{d\phi}{dv_0} = \frac{\phi}{v_0} \frac{\sigma_1}{2g}, \quad (4.52)$$

which is formally equal to the Clausius-Clapeyron equation and quantifies the slope along the instability line without ever including the stabilizing c^4 term or a second minimum of the bulk free energy density. The only condition is that one arbitrary point on the instability line is known. In order to proceed and solve the differential equation above, the free energy coefficients g and σ_1 need to be known analytically as a function of ϕ and v_0 . As already discussed in Sec. 4.1.1 the coefficient g is given by $g(u) = 1 - u^2 + 3u\sqrt{u^2 - 1}$ where $u = v_c/v_*$ is a function of both the critical swimming speed v_c on the instability line and the packing fraction ϕ since $v_* = 4\sqrt{DD_r}$ is density dependent. In Fig. 4.3 the measured long-time coefficients D of the passive suspension are shown as a function of the relevant packing fractions. A quadratic fit has been performed, yielding

$$D(\phi) \simeq -0.76\phi^2 - 0.34\phi + 0.72. \quad (4.53)$$

The fit is obviously poor in the dilute limit due to the fact that $D(\phi \rightarrow 0) = 0.72 \neq D_0 = 1$. Also for dense systems the fit leads to unphysical negative values. Nevertheless, for intermediate densities this analytical expression is used to solve Eq. (4.52), which requires expressions for the coefficients g (known analytically, easy to calculate) and σ_1 . The coefficient σ_1 is highly difficult to be estimated in simulations based on its analytical expression Eq. (4.45). Therefore it is approximated based on the observation,

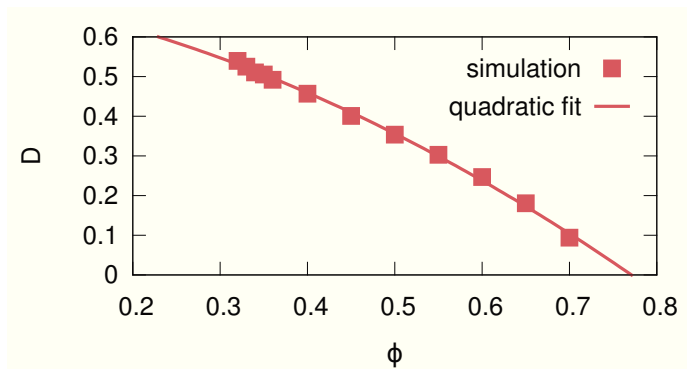


Figure 4.3: Long-time diffusion coefficient D of the passive suspension measured in simulations as a function of the packing fraction ϕ (squares) fitted by a quadratic function (solid line).

that there is a minimal packing fraction ϕ_* for which the suspension spontaneously phase separates starting from the homogeneous state. According to this, the coefficient σ_1 needs to change its sign from positive to negative at this density. This is implemented in the most minimalistic way, i.e., a linear relation $\sigma_1 \propto (\phi_* - \phi)$, where $\phi_* = 0.29$ and the proportionality factor are fitting parameters. As known point on the instability line ($\phi = 0.7, v_0 = 35$) is chosen so that the instability line can now be calculated from $v_0 = 35$ until $v_0 = 200$ according to the differential equation (4.52). As a result one observes the instability line shown in Fig. 4.4 which coincides superbly with the numerically obtained data points.

4.3 Nature of the phase transition

4.3.1 Numerical evidence

So far numerical results have only been presented for systems with packing fractions $\phi \geq 0.36$, showing a continuous increase of the mean relative size P of the largest cluster as the intrinsic swimming speed v_0 increases. For lower densities this behavior changes to a discontinuous jump of the order parameter P at significant higher propelling speeds, see solid lines in Fig. 4.5(b). This behavior may be explained in terms of the metastable region between the binodal and spinodal, where the system needs a sufficiently large fluctuation to start the phase separation process. Apparently, for smaller propelling speeds $v_0 < 180$ at $\phi = 0.3$ the probability of such a fluctuation is too low to be observed in the finite time window. For sufficiently high propelling speeds at $\phi = 0.3$ a critical fluctuation emerges (sometimes after the relaxation time during the data collection) which is then followed by macroscopic phase separation. Hence, the order parameter has not been averaged over the whole time of data collecting, but from the steady state of the phase separated system. The steady state has been identified by the mean

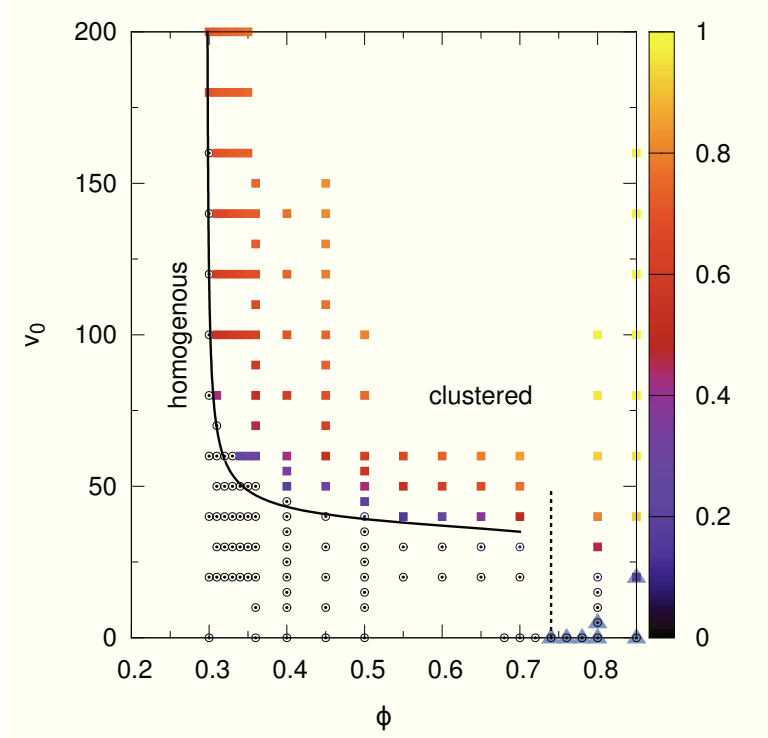


Figure 4.4: Phase diagram in the $\phi - v_0$ plane where each data point is extracted out of a simulation starting from an equilibrated passive fluid. The circles correspond to not phase separated suspensions with $P < 0.1$, while the squared symbols represent systems with $P > 0.1$. The squares are colored according to the value of the order parameter P . The blue triangles correspond to homogeneous crystalline suspensions identified by the order parameter $\Psi_6 > 0.45$ defined in Eq. (4.47). The solid line is the instability line estimated via Eq. (4.52) with the starting point $\phi = 0.7$ and $v_0 = 35$.

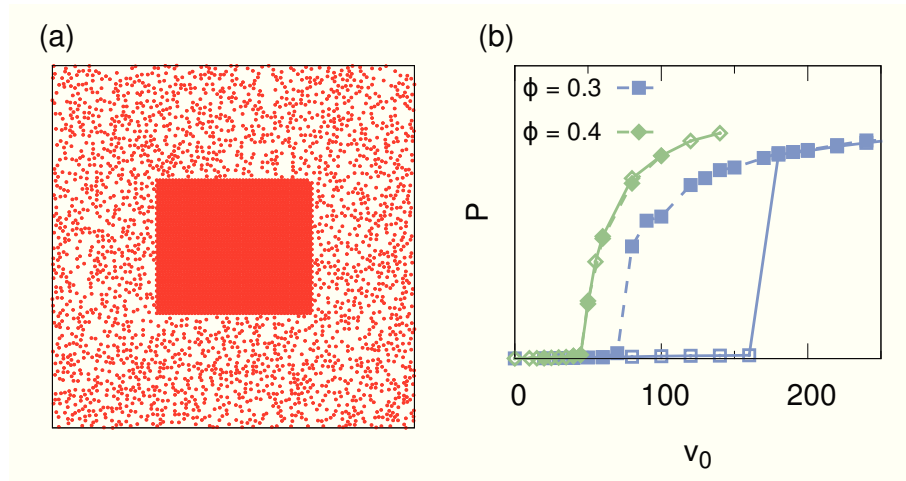


Figure 4.5: (a) Snapshot of an example start configuration for the hysteresis simulation protocol mentioned in the text. This is a sketch of the configuration so that the circles do not represent the actual size of the particles. (b) Mean relative size P of the largest cluster in the system for packing fractions $\phi = 0.3$ (blue) and $\phi = 0.4$ (green) as a function of the intrinsic swimming speed v_0 . The open symbols correspond to simulations starting in the equilibrated passive suspension and are connected by solid straight lines. The filled symbols are data points obtained via simulations with the hysteresis simulation protocol, where the suspension artificially contains a cluster of size $N/2$ before it starts to relax into steady state. The filled symbols are connected via dashed straight lines.

relative size P of the largest cluster, which shows fluctuations around its mean value but no further growth over a considerably time window. Due to the high propelling speed v_0 needed to achieve such a critical fluctuation, the dense cluster in steady state is quite big which is then represented by a sudden jump of the order parameter P , see open symbols in Fig. 4.5(b). However, if the number of particles is increased, e.g., $N = 40000$, the probability for a critical fluctuation does increase and one observes phase separation on shorter time scales. In Fig. 4.6 the temporal evolution of a system with $N = 40000$ particles is shown for packing fractions $\phi = 0.3$ and $\phi = 0.4$, which respectively correspond to systems developing phase separation in the meta-stable regime and in the region of spontaneous nucleation. The most significant visual difference is the development of several clusters which merge as time goes by for $\phi = 0.4$ (spontaneous nucleation), while for $\phi = 0.3$ only one critical fluctuation starts the phase separation into one single growing cluster until its size saturates. For a proper analysis of the different scenarios without the computational effort of simulating large system sizes for each set of parameters, an additional simulation protocol has been used: the system does not relax into steady state starting from the equilibrated fluid, but is provided with an artificially placed nucleus of size $N/2$ as start configuration. The remaining $N/2$ particles are placed randomly but non-overlapping around the nucleus, see Fig. 4.5(a). The orientation of all N particles are randomly distributed. Then, the intrinsic swimming speed is turned on and the system relaxes into steady state. The comparison to the simulations starting as an equilibrated passive fluid reveals a wide hysteresis for $\phi = 0.3$ while for $\phi = 0.4$ no hysteresis is observable, see Fig. 4.5(b). This again fortifies that the phase separation process of this non-equilibrium system shows similarities of an equilibrium (attractive) system explained by the concept of a binodal and spinodal.

4.3.2 Bifurcation diagrams

This section shows that the numerically observed hysteresis is in principle already contained in the analytically derived effective Cahn-Hilliard description of the system. Starting from the evolution equation for the density fluctuations

$$\partial_t c = \sigma_1 \nabla^2 c - \nabla^4 c - 2g \nabla \cdot (c \nabla c) \quad (4.54)$$

$$= \nabla^2 [\sigma_1 c - gc^2 - \nabla^2 c] \quad (4.55)$$

the existence of a stabilizing c^4 term in the bulk free energy density is postulated to take into account the repulsion between particles. The Cahn-Hilliard Equation is then given by

$$\partial_t c = \nabla^2 [\sigma_1 c - gc^2 + \kappa c^3 - \nabla^2 c] \quad (4.56)$$

with $\kappa > 0$ being the strength of the stabilizing term. Considering only linear terms of c in Fourier space, one obtains the dispersion relation

$$\tilde{\sigma}(q) = -\sigma_1 q^2 - q^4, \quad (4.57)$$

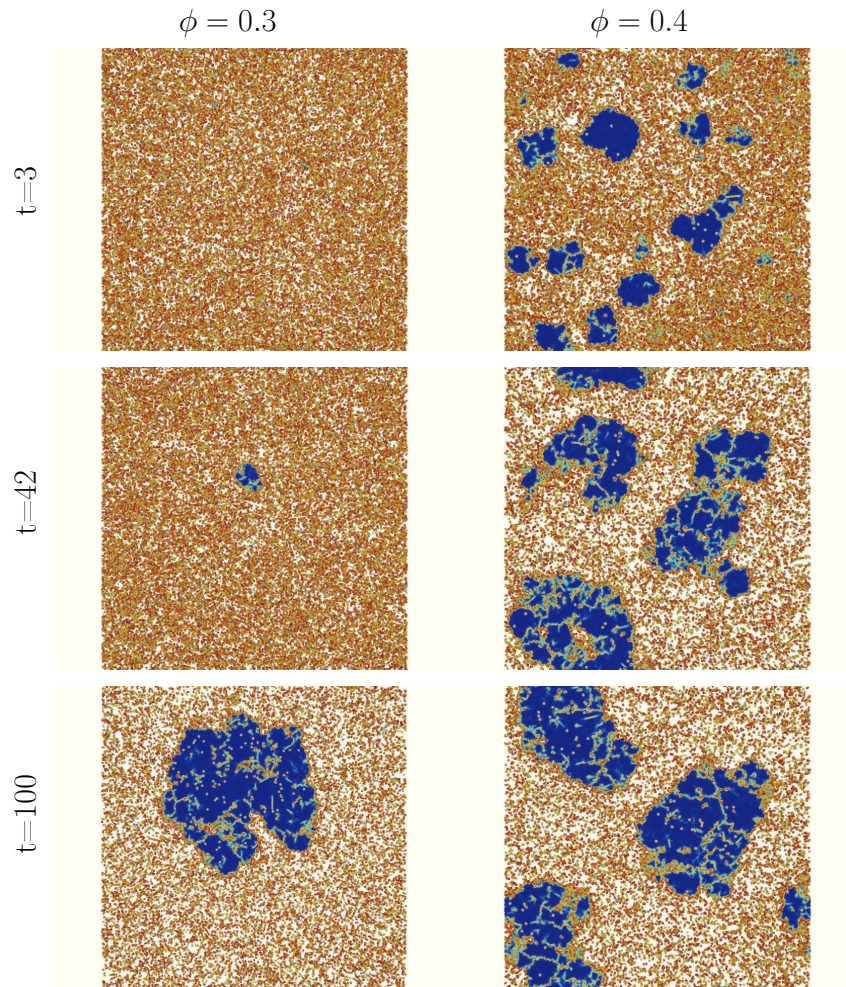


Figure 4.6: Phase separation dynamics for a system consisting of $N = 40000$ particles at $\phi = 0.3$ (left column) and $\phi = 0.4$ (right column). The three different times $t = 3$ (first row), $t = 42$ (second row) and $t = 100$ (third row) show the temporal evolution of spontaneously formed clusters which merge slowly for $\phi = 0.4$, while the system at $\phi = 0.3$ phase separates starting from one critical fluctuation leading to one single cluster which grows until saturation is reached. Particles are colored according to their q_6 value (Eq. (4.48)) where red particles correspond to $q_6 = 0$ and blue particles to $q_6 = 1$ indicating that clusters are highly crystalline but still very dynamic.

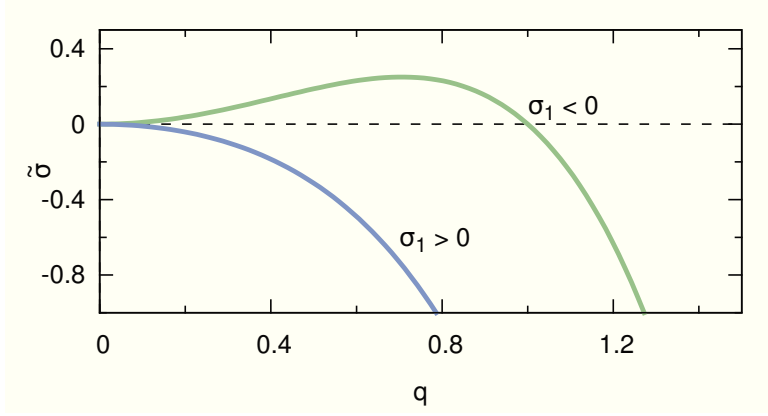


Figure 4.7: Sketch of the dispersion relation $\tilde{\sigma}(q)$ for $\sigma_1 < 0$ and $\sigma_1 > 0$ as a function of the magnitude q of the wave vector.

which quantifies the growth rate of the wave vector \mathbf{q} with magnitude q in the limit of linear stability. The growth rate reaches its maximum for $q_c^2 = -\sigma_1/2$ and is zero for $q_0^2 = -\sigma_1$ if $\sigma_1 < 0$. For $\sigma_1 > 0$ the growth rate is negative for any value of q , which means that the suspension is linearly stable, see Fig. 4.7.

Starting from q_0 with $\sigma_1 < 0$, the suspension is now considered to be slightly quenched either into the positive or negative region of the growth rate, i.e., $q^2 = q_0^2 - \lambda_q \epsilon^2$ with λ_q characterizing the quench depth and its sign the quench direction. The growth rate then follows

$$\tilde{\sigma}(q) = -\sigma_1(q_0^2 - \lambda_q \epsilon^2) - q_0^4 + 2q_0^2 \lambda_q \epsilon^2 - \lambda_q^2 \epsilon^4 \quad (4.58)$$

$$= q_0^2 \lambda_q \epsilon^2 - \lambda_q^2 \epsilon^4. \quad (4.59)$$

Based on this result an even slower time scale $s = \epsilon^2 t$ is introduced and together with $\sigma_1 = -q^2 - \lambda_q \epsilon^2$ the Cahn-Hilliard Eq. (4.56) reads

$$\epsilon^2 \partial_s c = \mathcal{L}c + \nabla^2 [-\lambda_q \epsilon^2 c - gc^2 + \kappa c^3], \quad (4.60)$$

while the self-adjoint operator $\mathcal{L} = -q^2 \nabla^2 - \nabla^4$ contains the terms being linear in both c and ϵ . In the next step the density field is expanded according to

$$c(\mathbf{r}, s) = \epsilon c_1(\mathbf{r}, s) + \epsilon^2 c_2(\mathbf{r}, s) + \dots. \quad (4.61)$$

Now, in analogy to Ref. 198, the amplitude equation for so-called roll solutions is derived. The unstable mode of a density fluctuation may saturate due to the coupling to nonlinear terms into a state which is spatially periodic, see Ref. 199 for a detailed review on instabilities. Therefore, the density fields in the expansion are considered to have the form

$$c_1(\mathbf{r}, s) = a(s)e^{i\mathbf{q}\mathbf{r}} + \text{c.c.} \quad (4.62)$$

$$c_2(\mathbf{r}, s) = b(s)e^{2i\mathbf{q}\mathbf{r}} + \text{c.c.} \quad (4.63)$$

$$\vdots \quad (4.64)$$

where a, b, \dots are complex amplitudes and c.c. denotes the complex conjugate. Similar to the previous multiple-scale analysis, Eq. (4.60) is now considered in orders of ϵ step by step. To linear order in ϵ one gets

$$\mathcal{L}c_1 = 0, \quad (4.65)$$

leading to an unbounded growth of the amplitude, which practically saturates due to the coupling to higher order terms. To quadratic order, one obtains

$$0 = \mathcal{L}c_2 - g\nabla^2 c_1^2 \quad (4.66)$$

leading to

$$0 = -12q^4 b + 4gq^2 a^2 \quad (4.67)$$

$$\stackrel{q \neq 0}{\Leftrightarrow} b = \frac{g}{3q^2} a^2. \quad (4.68)$$

To order ϵ^3 , Eq. (4.60) reads

$$\partial_s c_1 = \mathcal{L}c_3 + \nabla^2[-\lambda_q c_1 - 2g(c_1 c_2) + \kappa c_1^3], \quad (4.69)$$

which is multiplied by $e^{-i\mathbf{q}\mathbf{r}}$ and then integrated over an area A with an edge length being positive integers of $2\pi/q$. Hence, only terms with an initial dependence $e^{i\mathbf{q}\mathbf{r}}$ contribute to the integration while the rest vanishes due to translational invariance regarding integers of $2\pi/q$. Eq. (4.69) then becomes

$$\partial_s a = q^2 \lambda_q a + 2gq^2 a^* b - 2\kappa q^2 a^* a^2 \quad (4.70)$$

$$= q^2 \lambda_q a + \frac{2}{3} \left(g^2 - \frac{9}{2} \kappa q^2 \right) |a|^2 a \quad (4.71)$$

which is the desirable amplitude equation, where a^* denotes the complex conjugate of the amplitude a and $|a|^2 = aa^*$. For the magnitude of the amplitude one finds

$$\partial_s |a| = \frac{\partial}{\partial s} (aa^*)^{1/2} \quad (4.72)$$

$$= \frac{1}{2|a|} (a\partial_s a^* + (\partial_s a)a^*) \quad (4.73)$$

$$= q^2 \lambda_q |a| + \frac{2}{3} (g^2 - g_*^2) |a|^3 \quad (4.74)$$

with $g_*^2 = \frac{9}{2} \kappa q^2$. A stationary solution is given by the fixed point where the right hand side of Eq. (4.74) vanishes, i.e., $\partial_s |a| = 0$. The derivative of the right hand side of Eq. (4.74) with respect to $|a|$ is given by $\mathcal{S} = q^2 \lambda_q + 2(g^2 - g_*^2)|a|^2$ and determines the stability of a fixed point solution, i.e., unstable for $\mathcal{S} > 0$ and stable otherwise. The stationary solutions are given by

$$|a| = 0, \quad |a|^2 = \frac{\frac{3}{2} q^2 \lambda_q}{g_*^2 - g^2} = \frac{\lambda_q}{3\kappa} \frac{1}{1 - (g/g_*)^2}. \quad (4.75)$$

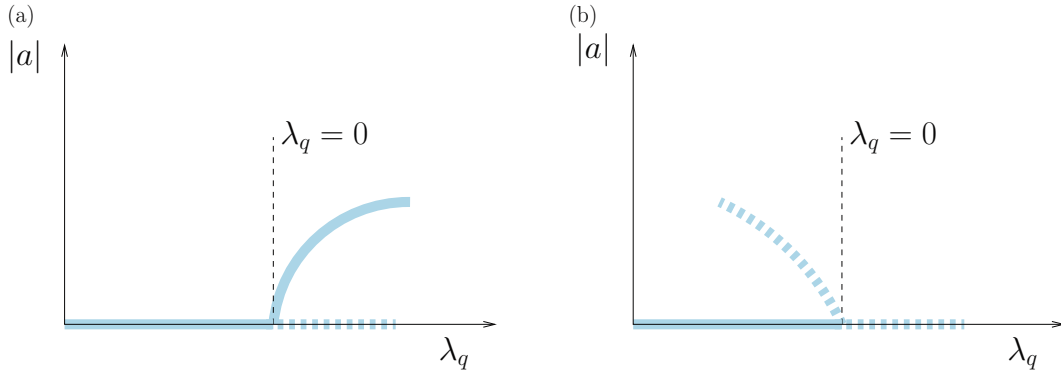


Figure 4.8: Bifurcation diagrams for (a) $g < g_*$ and (b) $g > g_*$ in form of a sketch of the magnitude $|a|$ of the amplitude as a function of the quench depth λ_q . The solid lines indicate stable solutions for the amplitude while the dashed lines represent unstable solutions.

Now two cases have to be distinguished where g_* is the relevant threshold. For $g < g_*$ and $\lambda_q < 0$, only the solution $|a| = 0$ is found, which is stable because $\mathcal{S} < 0$. This scenario corresponds to a homogeneous system since the amplitude of the density perturbation field is $|a| = 0$. If $\lambda_q > 0$ and still $g < g_*$, both solutions in Eq. (4.75) become possible, but the trivial one $|a| = 0$ is unstable ($\mathcal{S} > 0$) while the solution $|a| \propto \sqrt{\lambda_q}$ is stable ($\mathcal{S} < 0$). This behavior is known as supercritical bifurcation and corresponds to a continuous phase transition, in this case from the homogeneous system to a density perturbation field with finite amplitude, i.e., a phase separated system. The transition is illustrated in Fig. 4.8(a) where all solutions for the amplitude $|a|$ are plotted as a function of the quench λ_q . If $g > g_*$ and $\lambda_q < 0$ both solutions are possible with $|a| = 0$ being stable and $|a| \propto \sqrt{-\lambda_q}$ being unstable. Surprisingly, for $\lambda_q > 0$ only the unstable solution $|a| = 0$ is found, indicating a lack of a stable periodic roll solution, see Fig. 4.8(b). In case of a general differential equation, also negative values of the variable of interest (here the amplitude) are allowed, so that the graphs in Fig. 4.8 have to be mirrored with respect to the x -axis, resulting in the name pitchfork bifurcations due to their characteristic form.

For a better understanding of what happens at $g > g_*$ and $\lambda_q > 0$ where no stable solution seems to exist, one needs to expand the parameter g^2 around g_*^2 , i.e., $g^2 = g_*^2(1 + \epsilon^2)$. For the sake of simplicity the detailed math is not provided. In principle one needs to follow the previous method with a time scale $\epsilon^4 t$ (see second term on right hand side of Eq. (4.59)) to fifth order in ϵ , see also Refs. 198, 200. Finally, the condition for the complex amplitude a has the general form

$$\partial_s a = Aa + B|a|^2 a - C|a|^4 a \quad (4.76)$$

with A, B, C being real constants and $C > 0$ ensuring stabilization. In analogy to the previous approach, the evolution equation for the magnitude of the amplitude is derived, yielding

$$\partial_s |a| = A|a| + B|a|^3 - C|a|^5, \quad (4.77)$$

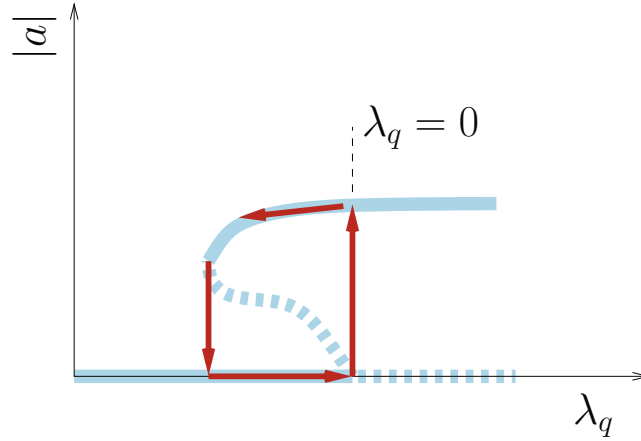


Figure 4.9: Bifurcation diagram of the subcritical behavior according to Eq. (4.77). The solid lines denote stable roll solutions while the dashed lines represent unstable solutions. The red arrows sketch the hysteresis loop when increasing/decreasing the quench parameter λ_q .

with the sign of $\tilde{\mathcal{S}} = A + 3B|a|^2 - 5C|a|^4$ determining the stability of the stationary solution. Comparing Eq. (4.77) with Eq. (4.74) and applying $\lambda_q > 0$ and $g > g_*$ which is the scenario of interest, one quickly identifies $A, B > 0$. In order to achieve a stable solution, the condition $\tilde{\mathcal{S}} < 0$ needs to be fulfilled, which is the case for the stationary solution

$$|a| = \sqrt{\frac{3B}{10C} + \sqrt{\left(\frac{3B}{10C}\right)^2 + A}}. \quad (4.78)$$

The corresponding bifurcation diagram is sketched in Fig. 4.9, where it is illustrated that the transition from zero to large amplitude happens in a big jump. This scenario is called subcritical bifurcation and corresponds to the discontinuous transition observed in simulations. In addition, the hysteresis behavior discovered in simulations can also be seen in Fig. 4.9 denoted by the red arrows. As λ_q decreases from large amplitude, it drops down to zero at a lower value of λ_q than it jumps from zero to large amplitude as λ_q increases. Unfortunately these results do not hold a quantitative comparison with numerical data, but are rather a demonstration of the capability of the theoretical description.

4.4 Numerical coexistence curve

This section presents the numerical estimation of the coexistence curve, in terms of phase separation in equilibrium also referred as binodal. Practically, this is done by measuring the densities of the two coexisting phases of a phase separated system. These densities correspond to the two points where the double tangent is steadily attached to the free

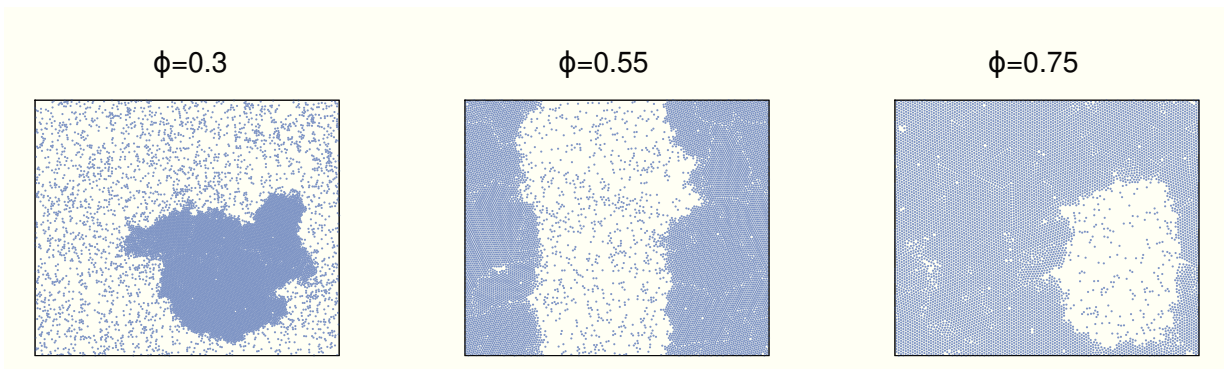


Figure 4.10: Finite size transitions for an almost quadratic simulation box with aspect ratio $L_x/L_y = 1.2$. While the density increases the phase separated system shows a dense droplet, a slab configuration and finally a gas bubble.

energy function. In accordance with studies in equilibrium [201, 202] a rectangular box of size $L_x \times L_y$ is applied with $L_x > L_y$. The numerical data has been carried out by computer simulations of $N = 10000$ particles where a dense slab consisting all N particles has been used as start configuration with randomly distributed particle orientations. Again, after a relaxation time $t_r = 100$ data has been collected. Due to the box geometry one can observe the typical finite size transitions, i.e., a dense droplet, to a slab which is spanned along the shorter length of the systems and finally to a gas bubble, see Fig. 4.10 for snapshots.

The choice of rectangular box geometry favor the formation of a slab, which has the advantage that it is easy to calculate a density profile $\rho(x)$ as a function of x , simply by dividing the simulation box into small slices (bins) and measuring the density in each bin. In addition the profile is shifted in the x -direction so that the slab is located around $L_x/2$ while the center of mass is fixed to the bin at $L_x/2$. What is not represented by the averaged density profiles are the instantaneous fluctuations not only at the interface, but also within the slab where fluctuations can create holes, see Fig. 4.11(a), (b). However, on average the density within the slab is constant and then smoothly decays to the dilute density. The region of that density decay is the interface of the two phases and will be analyzed in Chap. 5. The density profile can be expressed as its mean field functional form [35]

$$\rho(x) = \frac{1}{2}(\rho_+ + \rho_-) + \frac{1}{2}(\rho_+ - \rho_-)\tanh\left(\frac{x - x_0}{2w}\right) \quad (4.79)$$

with ρ_{\pm} being the bulk densities of the dense (+) and dilute (-) phase, x_0 the position of the interface and w the width of the interface. As shown in Fig. 4.11(c), the measured density profile is symmetric with respect to the position $x = L_x/2$ while the slab gets denser and the interface width smaller as propelling speed increases. Due to the symmetry of the system, the function in Eq. (4.79) is fitted to the left and to the right half of the box showing excellent agreement with the measured profile, see Fig.4.11(d). As a first approximation the resulting fit parameters of each half are treated independently.

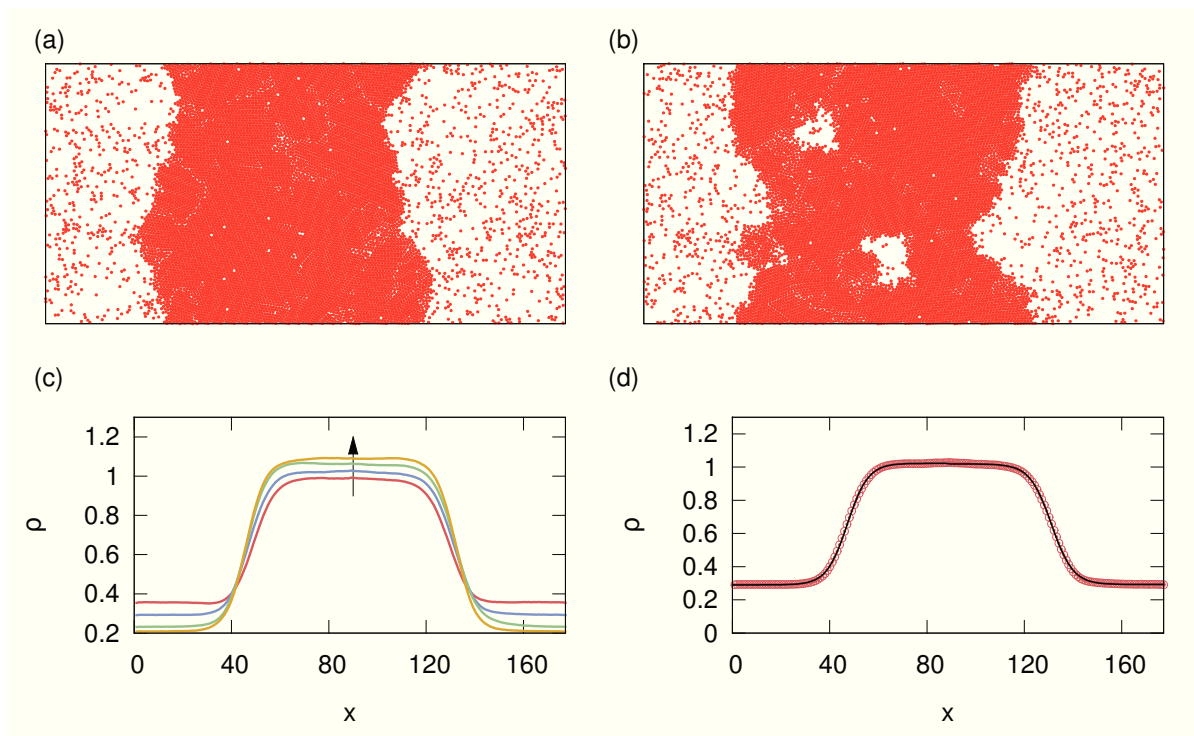


Figure 4.11: Snapshots of a phase separated system with box geometry $L_x/L_y = 2$ where a dense slab is surrounded by the dilute gas phase without (a) and with (b) fluctuations not only regarding the interface but also the inner region of the slab. (c) Density profiles $\rho(x)$ as a function of x for systems at average packing fraction $\phi = 0.5$ and intrinsic swimming speeds $v_0 = 80, 100, 130, 150$. The arrow indicates the direction of increasing propulsion, i.e., the higher the swimming speed the higher is the density of the dense slab. (d) Fit according to Eq. (4.79) for the left and right half of the system (solid line) and the measured average density profile (open circles) at overall packing fraction $\phi = 0.5$ and $v_0 = 100$.

The coexisting packing fractions $\phi_{\pm} = \rho_{\pm}\pi/4$ for a certain swimming velocity v_0 are then obtained by the average of the two values and are plotted into the $\phi - v_0$ -plane of the phase diagram to construct the coexistence curve, see Fig. 4.12. In addition a second (upper) x -axis is introduced, which shows the effective packing fraction ϕ_{eff} of an equivalent hard sphere system. This is calculated using the concept of the effective hard sphere diameter [203–206] given by the equality

$$\int_0^{\infty} f_{\text{HS}}(r)dr = \int_0^{\infty} f_{\text{WCA}}(r)dr \quad (4.80)$$

with the Mayer f-function

$$f_{\text{name}}(u_{\text{name}}(r)) = e^{-u_{\text{name}}/(k_B T)} - 1. \quad (4.81)$$

The left hand side of Eq. (4.80) yields $-d_{\text{eff}}$, the negative diameter of the equivalent hard spheres (HS). By numerically evaluating the right hand side one gets $d_{\text{eff}} \simeq 0.984$ for the WCA potential employed. One should note that this expression is given in units of $2R$, which is at the same time the distance for which the WCA potential drops to 0. Due to the softness of the potential an equivalent hard sphere system has an effective diameter somewhat lower than the potential cutoff. The concept of the effective hard sphere diameter works quite well since scaling the estimated freezing point $\phi_f^{(HS)} \simeq 0.705$ of a real hard sphere system [207,208] with the effective diameter $d_{\text{eff}} \simeq 0.984$ of the employed WCA system, gives $\phi \simeq 0.73$ which is in quite good agreement with the numerically estimated freezing point $\phi_f \simeq 0.74$ where $\Psi_6 \simeq 0.45$. This concept demonstrates how closely packed the dense phase is in terms of a hard sphere system. Fig. 4.12 does also show the possible spinodal constructed via Eq. (4.52) derived from the Cahn-Hilliard description. It can easily be seen that for $\phi > 0.3$ the meta-stable region, i.e., the gap between the coexistence curve and instability line (respectively binodal and spinodal in equilibrium), is not resolved very well by this representation which may be due to the approximations made in the Cahn-Hilliard theory. Nonetheless, for $\phi \leq 0.3$ there is a significant gap between the coexistence curve and the instability line from the Cahn-Hilliard theory, which explains the sudden jump of the order parameter for $\phi = 0.3$ as the instability line is crossed at $v_0 = 180$. As discussed, for lower swimming speeds the system is in the meta-stable region, where for a homogeneous active fluid the probability of a critical nucleation within the time window and size of the simulation is so low, that no phase separation is observed, leading to a significant hysteresis when an artificially constructed nucleus is provided.

4.5 Conclusion

In summary, starting from the effective hydrodynamic equations given in Sec. 3.2.1, a Cahn-Hilliard description of the system has been derived by considering a quench of depth $\epsilon > 0$ from the critical velocity on the instability line into the unstable regime of the system, i.e., $v_0 = v_c(1 + \epsilon)$. By expanding the physical quantities in integer orders

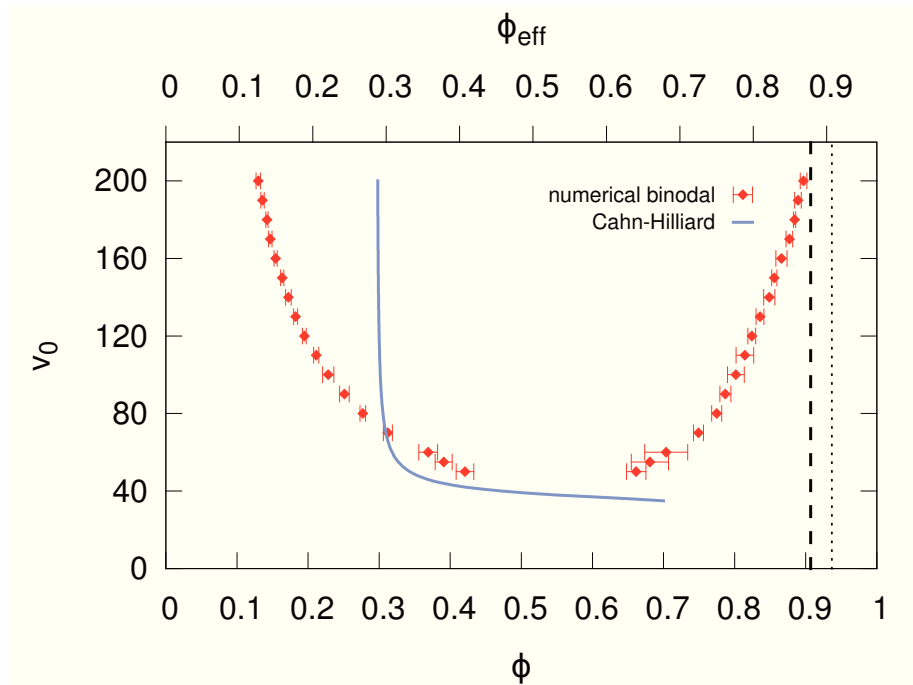


Figure 4.12: Numerically constructed coexistence curve in the $\phi - v_0$ -plane of the phase diagram according to the coexisting densities obtained from the fit function given by Eq. (4.79). The error bars are estimated by the standard deviation obtained from 5 independent simulation runs. The solid line represents the instability line (spinodal) constructed from the Cahn-Hilliard description in Sec. 4.2.2. The lower x -axis represents the packing fraction calculated with the particle diameter defined as the cutoff distance of the WCA potential, see Sec. 2.4. The densest possible packing of this definition is given by the dashed vertical line. The upper x -axis shows the effective packing fraction calculated by applying the effective diameter according to Eq. (4.80), which is lower than the previous definition due to the softness of the pair potential. The dotted line is the densest packing fraction of disks with the effective diameter.

of ϵ , an effective free energy functional has been deduced where only the density perturbation field c (in linear order of ϵ) has to be taken into account for the bulk free energy. Due to the chosen integer orders of the expansion, the customary stabilizing c^4 term is missing, but is shown to be derivable by expanding the density field in fractional orders of ϵ , yielding an expression which considers even smaller length scales and therefore resolves the repelling nature of the particles represented by the well-known symmetric Ginzburg-Landau free energy density.

Nonetheless, starting from the bulk free energy missing the stabilizing term, the instability line of this system has been constructed, showing excellent agreement with the transition line obtained from computer simulations. Next, the nature of the phase transition has been discussed in detail due to the observation of a discontinuous jump of the order parameter P at sufficiently low density, while for denser systems a continuous increase is observed at much lower propelling speeds. Applying an additional simulation protocol, where the system is provided with a cluster of size $N/2$, a significant hysteresis is observed in case of the discontinuous transition while there is no difference at higher densities. It is shown that this behavior is already contained in the effective Cahn-Hilliard description. By including a stabilizing term κc^4 in the bulk free energy density and analyzing the temporal evolution of the amplitudes of so-called roll solutions, bifurcation diagrams have been sketched where the hysteresis behavior is illustrated qualitatively. Besides the construction of a possible spinodal from the theory, a possible binodal has been constructed by measuring the coexistence densities at different v_0 . All previous observations, like the behavior of the order parameter P at different densities, are qualitatively consistent with the phase diagram constructed.

Although the work presented in this chapter is for sure a big step towards an entire understanding of the phase separation process, the scientific community is still at the very beginning of a complete theoretical framework for active phase separation. The effective Cahn-Hilliard description is valid near the critical velocity v_c . If fractional powers of ϵ are included, the theory is restricted to the vicinity of the minimal possible critical velocity $v = v_*$. However, simulations have shown that practically $v_c \gg v_*$, which instantly rises the demand of an effective free energy functional which is valid for any choice of parameters. Another point is the analytical construction of the possible spinodal which could be improved by a better approximation for the coefficient σ . In addition, by finding an analytical expression for the long-time diffusion coefficient of the passive suspension at higher densities, one could obtain the remaining part of the instability line ($\phi > 0.7$). Also the choice of the order parameter may need to be reconsidered since the denser the system gets the less swimming speed v_0 is needed to obtain a huge network of overlapping particles, i.e., a large cluster. Unfortunately this monotonic behavior is not in agreement with the picture of a spinodal, which is expected to change its slope at the critical point and follow the form of the binodal. As a result, the mean size of the largest cluster in the system may only serve as a good order parameter for systems below the density of a possible critical point. Since the active suspension has been effectively mapped to an equilibrium system, another approach may be to apply methods already used to analyze phase separation in equilibrium like it has recently been done in Refs. 209, 210. One aspect is without any doubt the applicability of equilibrium

concepts considering the physical properties of the interface between the two coexisting phases and is the topic of the next chapter.

Chapter 5

Interfacial tension

The description and investigation of interfaces separating two phases have been subject of several equilibrium studies both theoretically [16, 201] and in experiments [211, 212]. One key aspect is the interfacial tension γ , quantifying the energy needed to create interfaces at equilibrium. For phase separating active suspensions which are intrinsically out of equilibrium, there is a lack of concept to calculate the interfacial tension.

Motivated by the effective Cahn-Hilliard description in the previous chapter and a recently suggested mechanical swim pressure [213, 214], this chapter, based on publication 5, discusses the applicability of equilibrium concepts for calculating the interfacial tension of active suspensions. Again, the particle model introduced in Sec. 2.4 with $N = 10000$ particles serves as approximation of a quasi two-dimensional setup. In order to favor the formation of a dense slab (instead of a spherical dense cluster) the simulation box is rectangular with $L_x > L_y$ such that the slab spans along the shorter system length. Again, the start configuration of the system is a slab consisting all N particles which then relaxes for $t_r = 100$ before data is collected. After revisiting the active pressure introduced in Ref. 213, simulations have been performed of particles being confined in the x -direction by flat short range repulsive walls. As a result, the applicability of the active pressure is investigated by comparing it to the mechanical pressure exerted on the walls. Afterwards, extensive simulations without walls are performed to numerically measure the pressure profile along the x -direction which then leads to the line tension of the interface, see Eq. (2.62) in Sec. 2.7.1. Furthermore a fluctuation route is presented, connecting the mean squared interfacial width with the line tension of the interface for a system at equilibrium. This connection is then applied to the active system and compared to the determination via the pressure anisotropy at the interface.

5.1 Virial route

5.1.1 Active pressure tensor

As already discussed in Sec. 2.6 the pressure due to particle interactions is calculated via the virial expression

$$\bar{\bar{p}}^{(i)} = \frac{1}{A} \sum_{i=1}^N \sum_{j>i}^N \langle \mathbf{r}_{ij} \otimes \mathbf{f}_{ij} \rangle. \quad (5.1)$$

Due to the formation of a dense slab along the y -direction the system is translational invariant in that direction while symmetry is broken in the x -direction. This is the reason why the pressure tensor needs to be a function of x and is calculated by dividing the simulation box in slices along the x -direction with equal area A_s . The pressure tensor due to particle interactions is then given by

$$\bar{\bar{p}}^{(i)}(x) = \frac{1}{2A} \langle \mathbf{r}_{ij} \otimes \mathbf{f}_{ij} \rangle_x \quad (5.2)$$

where the brackets $\langle \cdot \rangle_x$ denote the average over time and pair of particles where at least one particle is in the considered slab at position x . The total virial of such a pair is then equally distributed to each particle which justifies the factor $\frac{1}{2}$.

Recently the idea of a mechanical pressure due to the self-propulsion motion of the particles has been discussed in Ref. 213. The approach is to consider the basic form of the virial, i.e., $\mathbf{r}_i \otimes \mathbf{f}_i$, with absolute particle position \mathbf{r}_i and force \mathbf{f}_i acting on particle i . The active swimming pressure tensor is postulated to be given as

$$\bar{\bar{p}}^{(a)} = \frac{1}{A} \sum_{i=1}^N \langle \mathbf{r}_i \otimes \mathbf{f}_i^{(s)} \rangle \quad (5.3)$$

with $\mathbf{f}_i^{(s)}$ being the swim force of particle i . The authors of Ref. 213 provide the following picture: the swim force is the force required to prevent the propulsion of a particle. In the particle model and reduced units employed in this work this force is given by

$$\mathbf{f}_i^{(s)} = v_0 \mathbf{e}_i, \quad (5.4)$$

yielding the active pressure tensor

$$\bar{\bar{p}}^{(a)} = \frac{v_0}{A} \sum_{i=1}^N \langle \mathbf{r}_i \otimes \mathbf{e}_i \rangle, \quad (5.5)$$

which correlates the particle position with its orientation. The total pressure of the system now reads

$$\bar{\bar{p}} = \bar{\bar{p}}_{id} + \bar{\bar{p}}^{(i)} + \bar{\bar{p}}^{(a)}, \quad (5.6)$$

while the active scalar pressure is given by [213]

$$p^{(a)} = \text{Tr} \left(\frac{\bar{\bar{p}}^{(a)}}{2} \right) = \frac{v_0}{2A} \sum_{i=1}^N \mathbf{r}_i \mathbf{e}_i. \quad (5.7)$$

Assuming non-interacting swimmers (ideal gas, $\dot{\mathbf{r}}_i = v_0 \mathbf{e}_i + \mu_0 \mathbf{f}_i^{(r)}$) the scalar active pressure is calculated as

$$p_{id}^{(a)} = \frac{v_0}{2A} \sum_{i=1}^N \int_{-\infty}^t dt' \langle \mathbf{e}_i(t) \dot{\mathbf{r}}_i(t') \rangle = \frac{1}{2D_r} \bar{\rho} v_0^2 \quad (5.8)$$

where the correlation $\langle \mathbf{e}(t) \mathbf{e}(t') \rangle = e^{-D_r |t-t'|}$ has been used. One clearly sees the dependency on the previous history of each particle which is an important point. In analogy to Eq. (5.2) the profile in x -direction is obtained by the expression

$$\bar{\bar{p}}^{(a)}(x) = \frac{v_0}{A} \langle \mathbf{r}_i \otimes \mathbf{e}_i \rangle_x. \quad (5.9)$$

This expression considers particles being in a slice at position x at time t and does not care about the previous history which is necessary for the correct pressure, see Eq. (5.8). Therefore the correlation between the x -position and projected orientation $\cos\varphi$ is not measured by the expression Eq. (5.9), but rather the mean orientation within a slice which is zero in a bulk phase and clearly not a physical pressure. Since the system is only sliced in the x -direction, the history regarding movement in y -direction is not neglected, so that $p_{yy}^{(a)}(x)$ provides the virial active pressure in the y -direction. The interaction part $\bar{\bar{p}}^{(i)}$ solely depends on interparticle distances, allowing to calculate both directional pressure terms $p_{xx}^{(i)}(x)$ and $p_{yy}^{(i)}(x)$ as a function of the x -direction. However, hydrostatic equilibrium dictates

$$\nabla \cdot \bar{\bar{p}} = 0, \quad (5.10)$$

implying a diagonal tensor. Furthermore, mechanical equilibrium demands a constant total normal pressure $p_N = p_{xx}$ throughout the whole box, otherwise the slab would not be stable. As explained, the total normal pressure can not be measured via the virial, but is needed to calculate the line tension. One solution to that, which is done in the following, is to obtain the total normal pressure via the total tangential pressure p_T in the bulk phase where the pressure is isotropic, i.e., $p_N = p_T$ holds.

5.1.2 Mechanical pressure

In this section it is shown that the proposed active swimming pressure does correspond to the actual mechanical pressure. In order to show this, periodic boundary conditions are employed in the y -direction while two confining short-ranged repulsive walls are located at $x = 0$ and $x = L_x$. The advantage is that the total normal pressure can directly be measured by the force exerted on the wall of length L_y . Due to the persistent

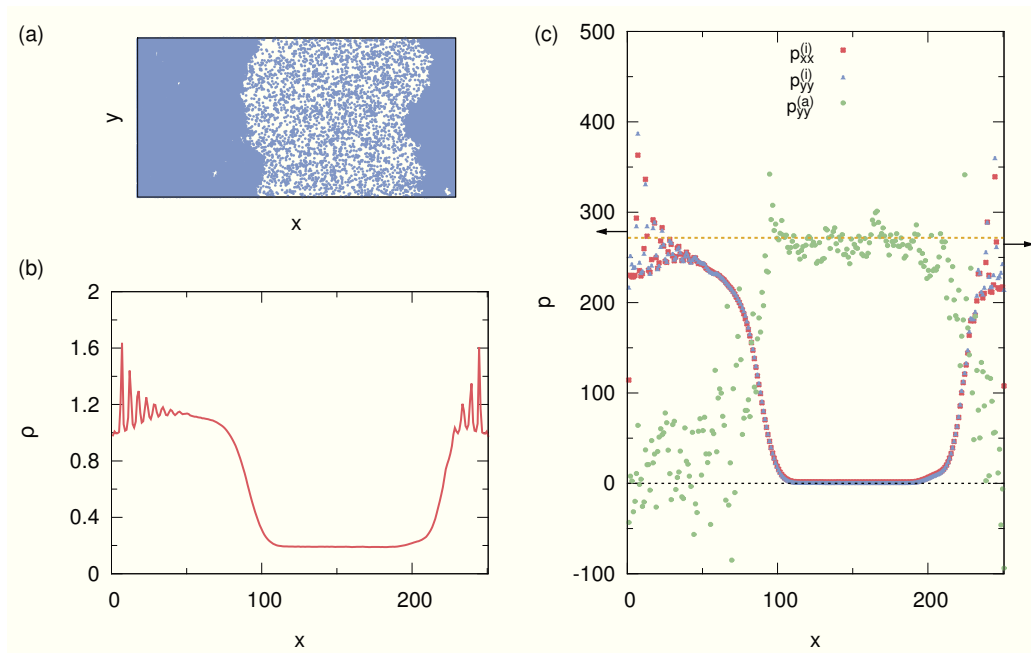


Figure 5.1: Suspension confined between two walls at $x = 0$ and $x = L_x$ at swimming speed $v_0 = 100$ and packing fraction $\phi = 0.5$. (a) Snapshot of the system showing the accumulation of particles at both walls. (b) Density profile $\rho(x)$ along the x -direction where the oscillations clearly show layering effects near the walls. (c) Pressure profiles along the x -direction. The two arrows indicate the pressure measured directly on the walls while the dashed yellow line shows the average. The lower black dashed line corresponds to zero pressure.

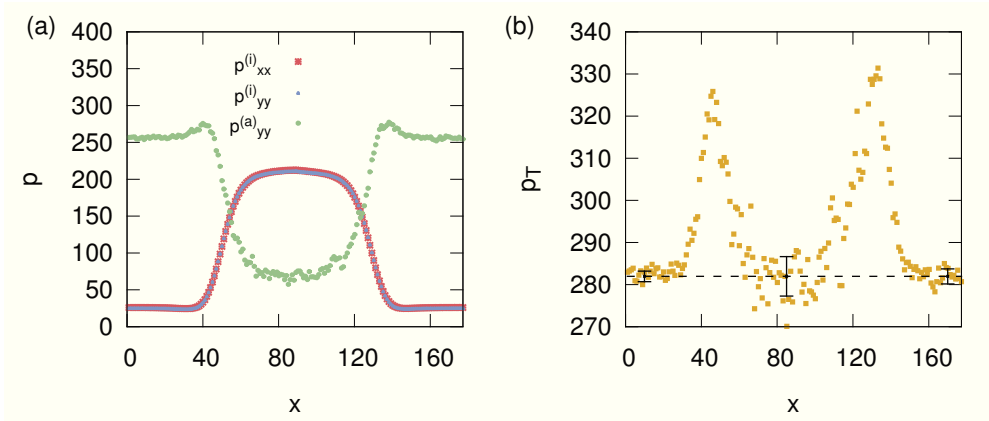


Figure 5.2: System at periodic boundary conditions in both directions at swimming speed $v_0 = 100$ and packing fraction $\phi = 0.5$. (a) Pressure profiles along the x -direction of the system. (b) Total tangential pressure $p_T = \rho + p_{yy}^{(i)} + p_{yy}^{(a)}$ along the x -direction. The dashed black line indicates the total (constant) normal pressure $p_N \simeq 282$ and has been obtained by averaging the values of horizontal fits in the intervals $[0 : 20]$, $[75 : 95]$, $[160 : L_x]$. The error bars correspond to the root mean squared residuals of each fit. The graphs have been obtained by averaging the profiles of 100 independent simulations.

propulsion of the particle against the walls and layering effects (cf. the oscillations in Fig. 5.1(b)) the pressure measured is not the actual bulk pressure, but serves as a sufficient approximation. Fig. 5.1(a) shows that particles do accumulate at both walls. The phase separation favors the formation of a larger slab at one wall while the accumulation at the other wall is due to the persistent motion of the particles. Fig 5.1(c) shows the various pressure profiles along the x -direction and the directly measured pressure on the walls. Here, the ideal gas part \bar{p}_{id} is neglected since its contribution is comparable to the typical error of the active pressure. One observes that the directly measured pressure on the walls does actually coincide with the tangential active pressure in the dilute bulk phase. The pressure due to particle interactions practically drops to zero in the dilute regime, which shows that the virial expression for the active pressure does indeed provide an intensive pressure fulfilling $p_N \approx p_T$ in bulk. One should also note that, likewise the interaction part of the pressure in the dilute phase, the swimming pressure averages to zero in the dense phase since particles hinder each other to propel persistently. The total pressure is then mainly dominated by the repulsive pair interactions.

5.1.3 Active interfacial tension

After the virial expression for the active swimming pressure has been shown to be consistent with the directly measured mechanical pressure, this section deals with the calculation of the interfacial tension. Now, periodic boundary conditions are applied in

both spatial directions and a rectangular simulation box with aspect ratio $L_x/L_y = 2$ is considered. The interfacial tension is obtained according to

$$\gamma = \frac{1}{2} \int_0^{L_x} [p_N - p_T(x)] dx, \quad (5.11)$$

where a factor $\frac{1}{2}$ is employed due to the existence of two interfaces. Fig. 5.2(a) shows the three pressure profiles along the x -direction. It is noteworthy that the interaction pressure is isotropic throughout the whole simulation box. It basically follows the density profile and is always positive due to the pure repulsive interaction (low pressure in dilute region, high pressure in dense region). Therefore the anisotropy of the total pressure at the interface is completely caused by the active nature of the system. One observes that the active pressure first increases at the interface which is a wall effect. The particles accumulate at the interface, which functions as a flexible wall, while particles are still able to propel parallel to the interface almost as persistently as they do in the dilute phase. Finally, since there is a higher density near the interface, the tangential swimming pressure is larger than in the dilute bulk phase. As density increases while entering the dense slab particles hinder each other to propel persistently, resulting in a decrease of the tangential swimming pressure. Fig. 5.2(b) shows the total tangential pressure $p_T = \rho + p_{yy}^{(i)} + p_{yy}^{(a)}$ along the x -direction. The constant total normal pressure p_N is now obtained by averaging the values of horizontal fits in regions which are as far away from the interface as the system size allows, yielding $p_N \simeq 282$. It is noteworthy, that in contrast to phase separated equilibrium systems the total tangential pressure is higher at the interface than in the bulk phases. As a result one obtains a negative interfacial tension

$$\gamma = \frac{1}{2} \int_0^{L_x} [p_N - p_T(x)] dx \simeq -842. \quad (5.12)$$

This result is completely counterintuitive regarding the equilibrium picture of the interfacial tension. It would imply that the system can lower its free energy by creating interfaces which is not consistent with the observation of a stable slab. Also the order of magnitude is rather high compared to two-dimensional Lennard-Jones interfaces [215–218] where $\gamma \sim 1$. In Sec. 5.3 the sign and order of magnitude will be discussed in detail and will also be compared to the result given by the following method.

5.2 Fluctuation route

For the sake of generality it is desirable to have another approach to estimate the interfacial tension, hopefully being comparable to the previously calculated value. This section does discuss such an approach via the fluctuations of the interface which is similar to the capillary wave theory [219–223].

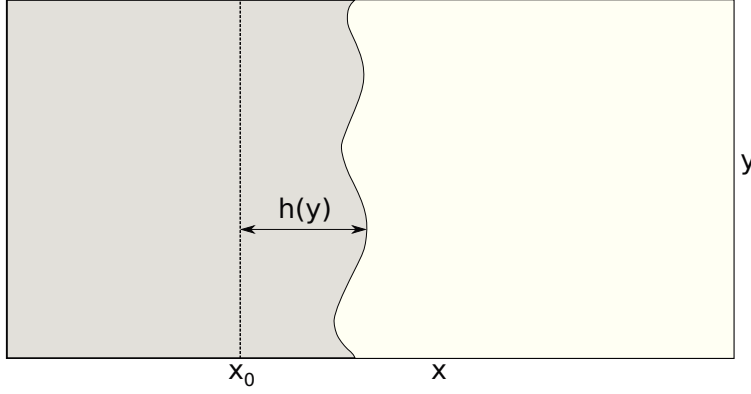


Figure 5.3: Sketch of an instantaneous interface without overhangs, which is then describable by a function $h(y)$. The mid point of the slab is represented by the dashed line located at x_0 .

5.2.1 Derivation

The instantaneous interface is considered to have no overhangs and be describable as a function $h(y)$ which measures the deviation from the mid point of the density profile, see Fig. 5.3 for a sketch. This function may be decomposed into Fourier modes

$$h(y) = \sum_q h_q e^{iqy} \quad (5.13)$$

with

$$h_q = \frac{1}{L_y} \int_0^{L_y} dy h(y) e^{-iqy}. \quad (5.14)$$

The magnitude of the wave vector q is given by (positive and negative) integers of $2\pi/L_y$. The interfacial width due to fluctuations is given by averaging over different interface configurations and integrating along the y -direction

$$w^2 = \frac{1}{L_y} \int_0^{L_y} dy \langle [h(y)]^2 \rangle = \sum_q \langle |h_q|^2 \rangle. \quad (5.15)$$

For a system at thermodynamic equilibrium the excess free energy due to the existence of a phase interface is given by $E_i = \gamma l$ where l is the interface length. In case of vapor-liquid phase separation in equilibrium, the interfacial tension γ is equal to the interfacial stiffness κ . For not too rough (slowly varying) interfaces the total interface length reads

$$l = \int_0^{L_y} dy \sqrt{1 + [h'(y)]^2} \quad (5.16)$$

$$\approx \int_0^{L_y} dy \left(1 + \frac{1}{2} [h'(y)]^2 \right) \quad (5.17)$$

$$= L_y + \frac{1}{2} L_y \sum_q q^2 |h_q|^2. \quad (5.18)$$

In equilibrium the equipartition theorem assigns each fluctuation mode an average energy of $k_B T/2$, yielding

$$\langle |h_q|^2 \rangle = \frac{1}{\kappa L_y q^2}. \quad (5.19)$$

By plugging Eq. (5.19) into Eq. (5.15)

$$w^2 = w_0^2 + \frac{2}{\kappa L_y} \sum_{q>0} \frac{1}{q^2} \quad (5.20)$$

is obtained, where w_0^2 is the fluctuation due to the $q = 0$ mode which is bounded due to periodic boundary conditions. Employing $q = 2\pi n/L_y$ with $n \geq 1$ ($n \in \mathbb{N}$) and the sum

$$\sum_{n=1}^{\infty} \frac{1}{n^2} = \frac{\pi^2}{6} \quad (5.21)$$

leads to

$$w^2 = w_0^2 + \frac{L_y}{12\kappa}. \quad (5.22)$$

It is now assumed that this relation still holds for the active system in non-equilibrium, but in general with a stiffness $\kappa \neq \gamma$. Furthermore it is necessary to point out that, regarding one single configuration, the dense phase is highly polycrystalline with a lot of point and line defects, see also Fig. 4.6. However, the crystalline order of such an active dense phase is only stable over a short time scale. That is why, in contrast to stable crystals being in coexistence with another phase in equilibrium [19], the active phase separation is basically comparable to vapor-liquid coexistence such that the interfacial stiffness does not depend on the crystalline orientation.

5.2.2 Active interfacial tension

In order to calculate the stiffness according to Eq. (5.22) the function

$$\rho(x) = \frac{1}{2}(\rho_+ + \rho_-) + \frac{1}{2}(\rho_+ - \rho_-)\tanh\left(\frac{x - x_0}{2w}\right) \quad (5.23)$$

is recalled, describing the mean field functional form of the density profile where w measures the interfacial width. Since the mean field form is not able to distinguish between the $q = 0$ mode and the undulations (capillary waves), the parameter w in Eq. (5.23) is equal to the total width given by Eq. (5.22). First, it is essential to ensure that one is considering systems in a regime where the interfacial width does not depend on the box dimension L_x . Fig. 5.4(a) shows the values of w (obtained by the fit) for self-propelled particles with $v_0 = 100$ at fixed $L_y = 90$ as a function of L_x while the number of particles has been varied such that all data points correspond to a packing fraction $\phi = 0.5$. One indeed observes within statistical errors a constant interfacial width. As a next step $L_x = 200$ is fixed while L_y is varied, also at fixed packing fraction

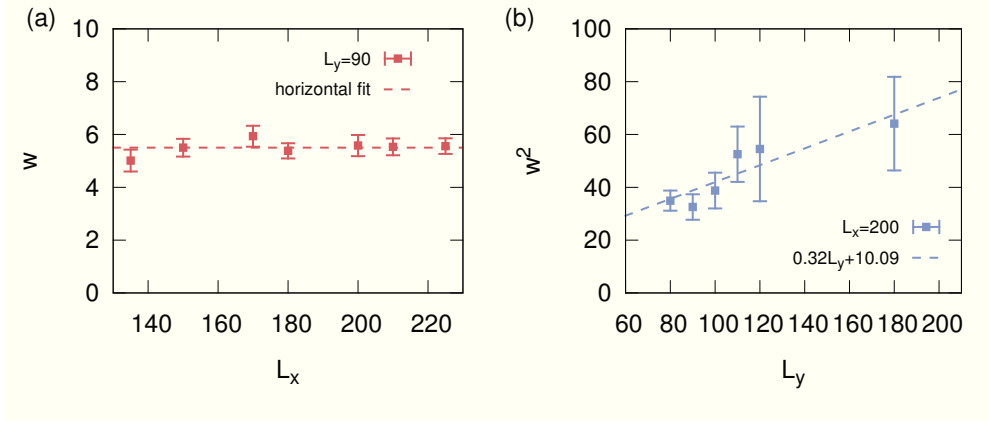


Figure 5.4: Self-propelled system at $v_0 = 100$ and constant $\phi = 0.5$. The interfacial width has been obtained according to Eq. (5.23) by averaging over 10 independent simulation runs. (a) Interfacial width w at fixed $L_y = 90$ as a function of L_x . The dashed line shows a horizontal fit. (b) The squared interfacial width w^2 at fixed $L_x = 200$ as a function of L_y . The dashed line corresponds to a linear fit. The error bars denote the standard deviation given by the 10 independent runs.

$\phi = 0.5$, see Fig. 5.4(b). In accordance with Eq. (5.22) a linear fit is applied showing quite good agreement with the data points although for larger L_y the estimated error is relatively large. The linear fit yields an interfacial stiffness

$$\kappa = \frac{1}{12 \cdot 0.32} \simeq 0.26. \quad (5.24)$$

The magnitude of order of this result is comparable to equilibrium studies [216], but seems to be contrary to the large negative interfacial tension obtained in Sec 5.1.3 which is discussed in the following.

5.3 Housekeeping work

For the active system it is necessary to recall that particles maintain a fixed velocity v_0 which means that particles constantly spent a “housekeeping” work $\mathcal{W} < 0$ on the surrounding fluid. An energy scale for this work is the hydrodynamic force times the persistence length $l_p = v_0/D_r$. Accordingly, the work spent on the solvent per particle is $\mathcal{W}/N = -v_0^2/D_r$ (recall $\mu_0 = 1$ in reduced units). If the amount of work γ gained by increasing the interface is lower than the energy pumped into the system by the active motion the interface (and therefore the slab) is stable. Scaling the interfacial tension with this housekeeping work one gets an interfacial stiffness $\kappa = -\gamma D_r/v_0^2 \simeq 0.25$ which is in excellent agreement with the value obtained via the interface fluctuations. Since the fluctuation route is derived from a passive suspensions and just mapped onto the

active system the “housekeeping” work \mathcal{W} is already incorporated. This is different for the virial route which considers an explicit swimming pressure leading to the negative interfacial tension.

5.4 Conclusion

In summary it has been shown that the mechanical interfacial tension in active suspensions is negative. In contrast to equilibrium systems this energy can not be “used” by the system to lower its free energy, but is part of the work constantly spent by the active particles on the surrounding solvent. If the mechanical derived interfacial tension is normalized to that negative work one finds a value which coincides impressively well with the interfacial stiffness determined by the concept of interface fluctuations, i.e., capillary waves.

For active bulk phases thermodynamic concepts known from equilibrium seem to work [133,209,224] as well as the effective Cahn-Hilliard description derived in Chap. 4. However, the inclusion of a negative tension into these concepts will be a future challenging task which will hopefully give a deeper general insight into the effective description of non-equilibrium systems. An essential question needed to be solved is whether fluctuations of active suspensions can be described by an equivalent equilibrium system or if that concept only works for mean-field descriptions. Furthermore it is desirable to consider even larger systems ($N \geq 10^5$) where the width of the two phases is several orders of magnitude larger than the persistent length of the particles. This would ensure that particles reorient several times before reaching the next periodic copy of the slab, leading to the actual bulk pressure which is measured. This is illustrated by the following picture: imagine (periodically copied) slabs separated by a dilute phase of width l_p . The particles entering the dilute phase do not reorient until they reach the next slab. Consequently, the collision frequency with particles coming from the other slab, which also do not reorient in the dilute phase, is increased significantly, leading to a lower active pressure than it would be measured in bulk where there is no preferred orientation. Beside performing the analysis of the interfacial tension/stiffness for larger systems one should also consider larger propelling speeds since in this work only the case $v_0 = 100$ is discussed. Although the results should not change qualitatively these aspects are postponed to future works.

Chapter A

Appendix

A.1 Finite size analysis of the phase transition

In order to justify the choice of the system size $N = 4900$ the behavior of the mean relative size P of the largest cluster in the system is studied for system sizes $N = 1600, 2500$ being below and $N = 40000$ being way above the system size $N = 4900$ used in the main simulations. However, for the large system, the coarsening dynamics change: since clusters form spontaneously there are several more clusters in the larger system. Due to the system size, steady state (one large cluster) for intermediate intrinsic swimming speeds v_0 is not reached even after simulating for $t = 300$, see Fig. A.1(c). For larger swimming speeds, steady state is reached within the relaxation time $t_r = 100$, see Fig. A.1(d). For a proper analysis, the simulation protocol stays the same also for the large system, i.e., $t_r = 100$ relaxation time starting from the equilibrated passive suspension followed by data collecting for $t_s = 100$, while for the large system also the largest and smallest size of the biggest cluster is tracked to obtain error bars, yielding a better comparability with the smaller systems, see Fig. A.2. The numerical data demonstrates that the onset of the clustering occurs at approximatively the same speed. In addition, although different coarsening dynamics are present, the steady state at sufficiently large swimming speeds, here $v_0 = 120$, is the same for $N = 4900$ as it is for $N = 40000$ particles. This shows that increasing the system size ($N > 4900$) does not change the properties of the steady state and therefore fortifies simulations of $N = 4900$ particles to avoid huge computational times.

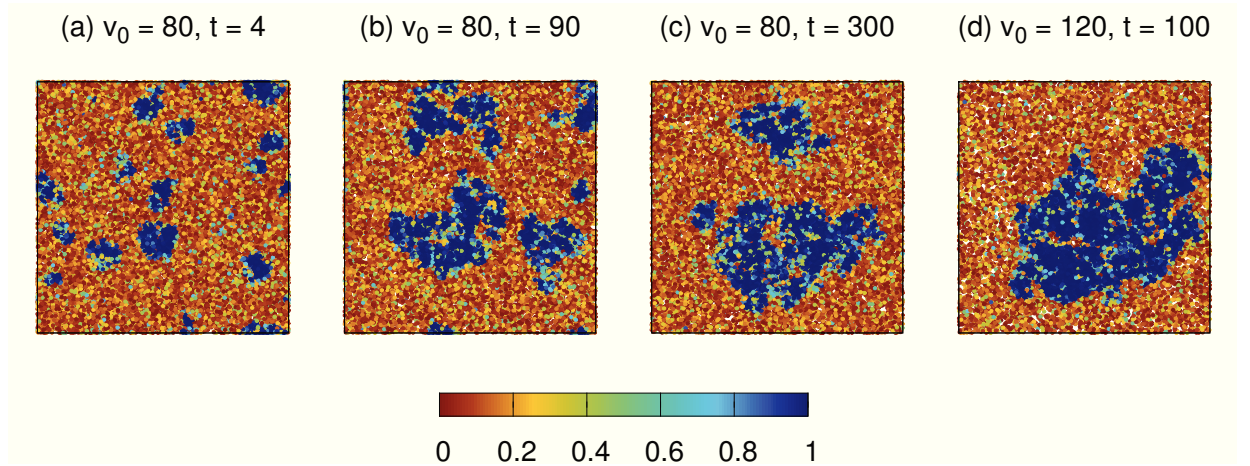


Figure A.1: Simulation snapshots of the system containing $N = 40000$ particles at area fraction $\phi = 0.4$. The snapshots (a)-(c) are at intrinsic propelling speed $v_0 = 80$ and recorded at times $t = 4, t = 90$ and $t = 300$ after the propulsion has been turned on starting from the passive equilibrium suspension. The snapshot (d) is at swimming speed $v_0 = 120$ where the system reached the steady state of one big cluster after $t = 100$. Particles are colored according to their local bond orientational order, measured by the parameter q_6 given by Eq. (4.48) in Sec. 4.2.1

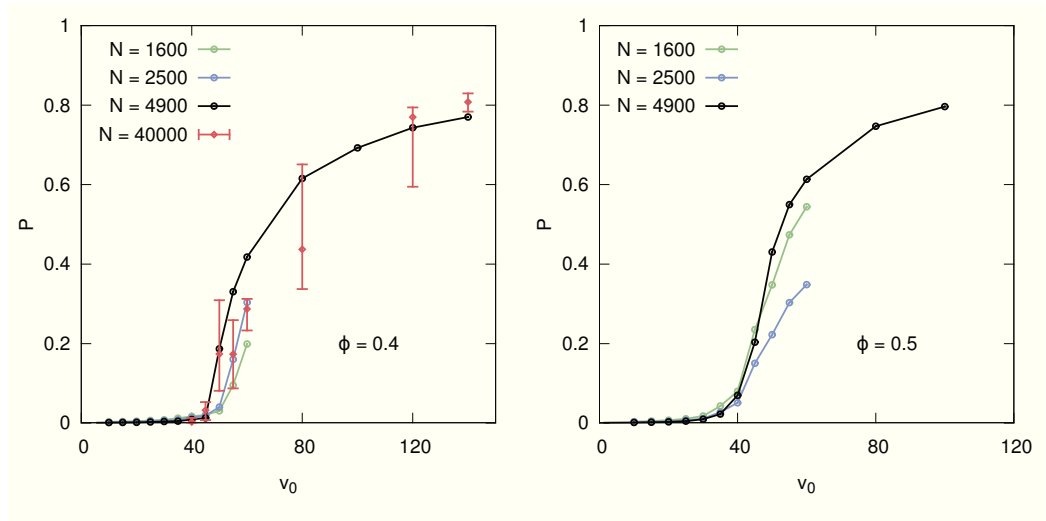


Figure A.2: Mean relative size of the largest cluster in the system as a function of intrinsic propelling speed v_0 at area fractions $\phi = 0.4$ (left) and $\phi = 0.5$ (right) and system sizes $N = 1600, N = 2500, N = 4900$ and $N = 40000$. The error bars for the $N = 40000$ system correspond to the largest and smallest measured size of the order parameter P .

A.2 Free energy functional

Here the relation

$$\partial_t c = \sigma_1 \nabla^2 c - \nabla^4 c - 2g \nabla \cdot (c \nabla c) = \nabla^2 \frac{\delta \mathcal{F}}{\delta c} \quad (\text{A.1})$$

is shown to be valid with

$$\mathcal{F}[c] = \int d\mathbf{r} \left[\frac{1}{2} |\nabla c|^2 + f(c) \right] \quad (\text{A.2})$$

where

$$f(c) = \frac{1}{2} \sigma_1 c^2 - \frac{1}{3} g c^3 \quad (\text{A.3})$$

is the effective bulk free energy density. First, the functional derivative is performed

$$\frac{\delta \mathcal{F}}{\delta c(\mathbf{r})} = \int \left[\frac{\delta}{\delta c(\mathbf{r})} \frac{1}{2} |\nabla c(\mathbf{r}')|^2 + \frac{\delta}{\delta c(\mathbf{r})} \frac{1}{2} \sigma_1 c^2(\mathbf{r}') - \frac{\delta}{\delta c(\mathbf{r})} \frac{1}{3} g c^3(\mathbf{r}') \right] d\mathbf{r}' \quad (\text{A.4})$$

$$= \int \left[(\nabla c) \nabla \frac{\delta c(\mathbf{r}')}{\delta c(\mathbf{r})} + \sigma_1 c \frac{\delta c(\mathbf{r}')}{\delta c(\mathbf{r})} - g c^2 \frac{\delta c(\mathbf{r}')}{\delta c(\mathbf{r})} \right] d\mathbf{r}'. \quad (\text{A.5})$$

Using the identity $\frac{\delta c(\mathbf{r}')}{\delta c(\mathbf{r})} = \delta(\mathbf{r}' - \mathbf{r})$, where $\delta(\mathbf{r})$ is the Dirac-function, one gets

$$\frac{\delta \mathcal{F}}{\delta c(\mathbf{r})} = \int \left[(\nabla c) \nabla \delta(\mathbf{r}' - \mathbf{r}) \right] d\mathbf{r}' + \sigma_1 c(\mathbf{r}) - g c^2(\mathbf{r}) \quad (\text{A.6})$$

$$= \underbrace{\left[\nabla c \delta(\mathbf{r}' - \mathbf{r}) \right]_{-\infty}^{\infty}}_{=0} - \int \left[\nabla^2 c \delta(\mathbf{r}' - \mathbf{r}) \right] d\mathbf{r}' + \sigma_1 c(\mathbf{r}) - g c^3(\mathbf{r}) \quad (\text{A.7})$$

$$= -\nabla^2 c(\mathbf{r}) + \sigma_1 c(\mathbf{r}) - g c^2(\mathbf{r}). \quad (\text{A.8})$$

As the last step the Nabla operator is applied twice, giving

$$\nabla^2 \frac{\delta \mathcal{F}}{\delta c} = -\nabla^4 c + \sigma_1 \nabla^2 c - g \nabla^2 c^2 \quad (\text{A.9})$$

$$= -\nabla^4 c + \sigma_1 \nabla^2 c - 2g \nabla \cdot (c \nabla c), \quad (\text{A.10})$$

which coincides with the statement in Eq. (A.1).

A.3 Lower order expansion

In order to obtain a stabilizing c^4 term in the free energy density one needs to include fractional orders of ϵ in the expansion, i.e.,

$$\delta \rho = \epsilon^{1/2} c + \epsilon c_1 + \epsilon^{3/2} c_{3/2} \quad (\text{A.11})$$

$$\mathbf{p} = \sqrt{\epsilon} [\epsilon^{1/2} \mathbf{p}_1 + \epsilon \mathbf{p}_{3/2} + \epsilon^{3/2} \mathbf{p}_2] \quad (\text{A.12})$$

where the orientational field is again additionally scaled with $1/\sqrt{\epsilon}$ as it is done in the main text. The coefficients α, β, ξ are defined as

$$\xi = \frac{\bar{\rho}\zeta}{v_*}, \quad \alpha = 4 \left(\frac{v_0}{v_*} - \xi \right), \quad \beta = 2 \left(\frac{v_0}{v_*} - 2\xi \right) \quad (\text{A.13})$$

and are therefore treated to be analytical functions in v_0 . Accordingly, their expansion lacks fractional powers of ϵ , i.e., the expansions until the relevant order read

$$\alpha = \alpha_0 + \epsilon\alpha_1, \quad (\text{A.14})$$

$$\beta = \beta_0 + \epsilon\beta_1, \quad (\text{A.15})$$

$$\xi = \xi_c + \epsilon\xi_1. \quad (\text{A.16})$$

Starting again at the set of equations

$$\partial_t \delta\rho = -\alpha \nabla \cdot \mathbf{p} + \nabla^2 \delta\rho + 4\xi \nabla \cdot (\mathbf{p} \delta\rho), \quad (\text{A.17})$$

$$\partial_t \mathbf{p} = -\beta \nabla \delta\rho + \nabla^2 \mathbf{p} - \mathbf{p} + 4\xi \delta\rho \nabla \delta\rho \quad (\text{A.18})$$

and plugging in the above expansions for $\delta\rho, \mathbf{p}, \alpha, \beta, \xi$ together with the time and length scales being rescaled with $1/\epsilon^2$ and $1/\sqrt{\epsilon}$ respectively, one obtains to lowest order ($\epsilon^{3/2}$ in Eq. (A.17) and ϵ in Eq. (A.18))

$$0 = -\alpha_0 \nabla \cdot \mathbf{p}_1 + \nabla^2 c, \quad (\text{A.19})$$

$$0 = -\beta_0 \nabla c - \mathbf{p}_1. \quad (\text{A.20})$$

Solving the second equation for \mathbf{p}_1 yields

$$\mathbf{p}_1 = -\beta_0 \nabla c \quad (\text{A.21})$$

and plugging this result into the first one, the linear stability condition

$$1 + \alpha_0 \beta_0 = 0 \quad (\text{A.22})$$

is recovered. The next order (ϵ^2 in Eq. (A.17) and $\epsilon^{3/2}$ in Eq. (A.18)) gives

$$0 = -\alpha_0 \nabla \cdot \mathbf{p}_{3/2} + \nabla^2 c_1 + 4\xi_c \nabla \cdot (\mathbf{p}_1 c), \quad (\text{A.23})$$

$$0 = -\beta_0 \nabla c_1 + 4\xi_c c \nabla c - \mathbf{p}_{3/2}. \quad (\text{A.24})$$

Solving Eq. (A.24) for $\mathbf{p}_{3/2}$ one obtains

$$\mathbf{p}_{3/2} = -\beta_0 \nabla c_1 + 4\xi_c c \nabla c. \quad (\text{A.25})$$

Inserting this result into Eq. (A.23), using Eq. (A.21) and $\alpha_0 \beta_0 = -1$ one derives the condition

$$0 = 4\xi_c (\alpha_0 + \beta_0) \nabla \cdot (c \nabla c). \quad (\text{A.26})$$

There are two scenarios for which Eq. (A.26) is fulfilled: the first one corresponds to $c = 0$ where density fluctuations of order $\epsilon^{1/2}$ vanish. This route has been followed in

Sec. 4.1 and is reasonable under the assumption $v_c \gg v_*$ which has been confirmed by computer simulations, see Fig. 3.11. However, the second scenario is

$$\alpha_0 + \beta_0 = 6 \frac{v_c}{v_*} - 8\xi_c = 0, \quad (\text{A.27})$$

which is true for $v_c = v_*$ and reduces the applicability of this lower order expansion to this special case. The free energy coefficients are then simply given by $g = 0$ and $\sigma_1 = -2$. The set of equations in the next higher order ($\epsilon^{5/2}$ in Eq. (A.17) and ϵ^2 in Eq. (A.18)) reads

$$\partial_t c = -\alpha_0 \nabla \cdot \mathbf{p}_2 - \alpha_1 \nabla \cdot \mathbf{p}_1 + \nabla^2 c_{3/2} + 4\xi_c \nabla \cdot (c_1 \mathbf{p}_1 + c \mathbf{p}_{3/2}), \quad (\text{A.28})$$

$$0 = -\beta_0 \nabla c_{3/2} - \beta_1 \nabla c + \nabla^2 \mathbf{p}_1 - \mathbf{p}_2 + 4\xi_c (c \nabla c_1 + c_1 \nabla c). \quad (\text{A.29})$$

Similar to the previous steps, the second equation is solved for \mathbf{p}_2 while the derived expressions for \mathbf{p}_1 and $\mathbf{p}_{3/2}$ are used. By considering the conditions Eqs. (A.22) and (A.27) one gets

$$\partial_t c = \sigma_1 \nabla^2 c - \nabla^4 c + (4\xi_c)^2 \nabla \cdot (c^2 \nabla c). \quad (\text{A.30})$$

In analogy to App. A.2 one shows that this implies a free energy functional with free energy density

$$\frac{1}{2} |\nabla c|^2 + f_{GL}(c) = \frac{1}{2} |\nabla c|^2 + \frac{1}{2} \sigma_1 c^2 + \frac{4}{3} \xi_c^2 c^4, \quad (\text{A.31})$$

commonly known as the symmetric Ginzburg-Landau free energy density.

A.4 Numerical phase diagrams for different threshold choices

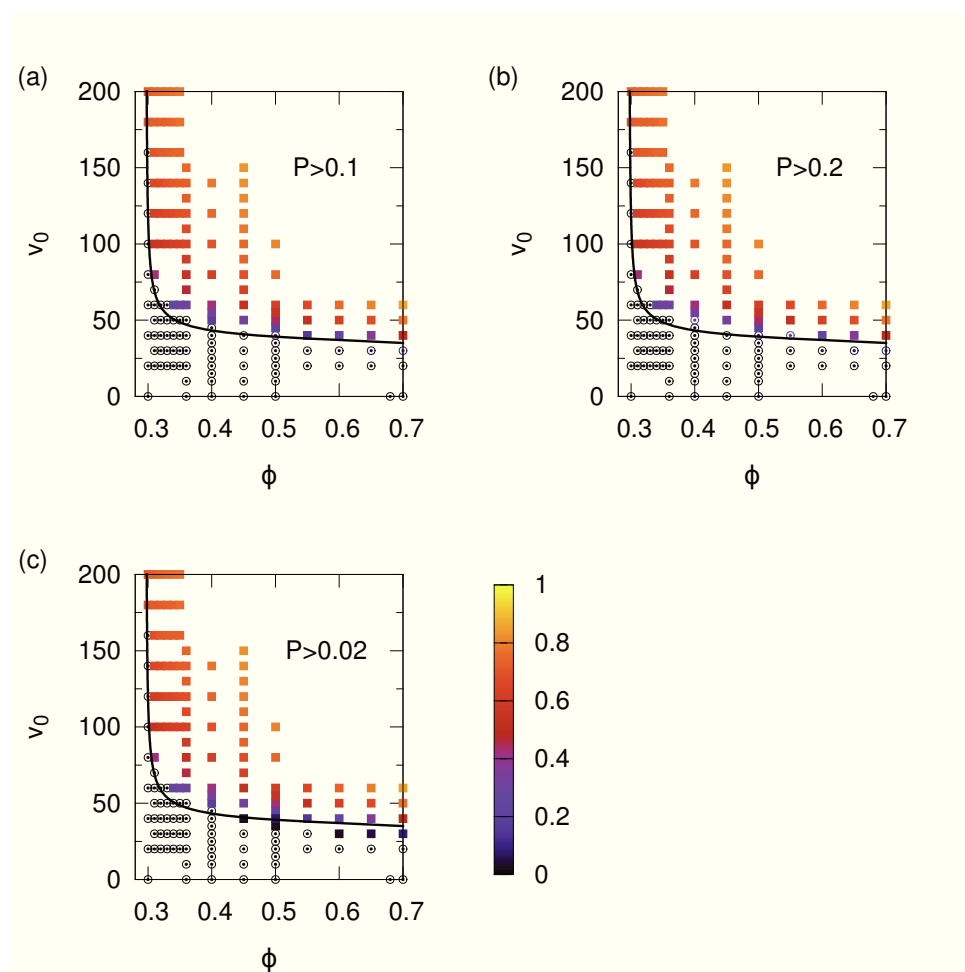


Figure A.3: Phase diagrams in the $\phi - v_0$ plane: the data points in (a), (b) and (c) are extracted out of the same simulation runs starting from an equilibrated passive fluid. The circles correspond to suspensions below the threshold (a) $P < 0.1$ (b) $P < 0.2$ and (c) $P < 0.02$, while the squared symbols represent systems which are considered as phase separated with (a) $P > 0.1$ (b) $P > 0.2$ and (c) $P > 0.02$. The squares are colored according to the value of the order parameter P . The solid line is the instability line estimated via Eq. (4.52) with the starting point $\phi = 0.7$ and $v_0 = 35$.

Fig. A.3 demonstrates the minor sensitivity of the choice of threshold of the order parameter P from which a system is considered as phase separated. While the threshold changes from $P > 0.1$ to $P > 0.2$ and even one order of magnitude lower to $P > 0.02$, the numerical data points still show quite good agreement with the instability line obtained from the construction via the Cahn-Hilliard description.

Bibliography

- [1] I. BUTTINONI, J. BIALKÉ, F. KÜMMEL, H. LÖWEN, C. BECHINGER, and T. SPECK, *Physical Review Letters* **110**, 238301 (2013).
- [2] J. BIALKÉ, H. LÖWEN, and T. SPECK, *Europhysics Letters* **103**, 30008 (2013).
- [3] T. SPECK, J. BIALKÉ, A. M. MENZEL, and H. LÖWEN, *Physical Review Letters* **112**, 218304 (2014).
- [4] J. BIALKÉ, T. SPECK, and H. LÖWEN, *Journal of Non-Crystalline Solids* **407**, 367 (2015), 7th IDMRCS: Relaxation in Complex Systems.
- [5] J. BIALKÉ, H. LÖWEN, and T. SPECK, *ArXiv e-prints* **arXiv:1412.4601** (2014).
- [6] J. J. THOMSON, *Philosophical Magazine Series 5* **44**, 293 (1897).
- [7] E. RUTHERFORD, *Philosophical Magazine (reprint)* **92**, 379 (2012).
- [8] J. CHADWICK, *Nature* **129**, 312 (1932).
- [9] M. N. ROSENBLUTH and A. W. ROSENBLUTH, *The Journal of Chemical Physics* **22**, 881 (1954).
- [10] W. W. WOOD and J. D. JACOBSON, *The Journal of Chemical Physics* **27**, 1207 (1957).
- [11] B. J. ALDER and T. E. WAINWRIGHT, *The Journal of Chemical Physics* **27**, 1208 (1957).
- [12] P. N. PUSEY and W. VAN MEGEN, *Nature* **320**, 340 (1986).
- [13] Z. CHENG, P. CHAIKIN, W. RUSSEL, W. MEYER, J. ZHU, R. ROGERS, and R. OTTEWILL, *Materials & Design* **22**, 529 (2001).
- [14] E. P. BERNARD and W. KRAUTH, *Physical Review Letters* **107**, 155704 (2011).
- [15] J. E. LENNARD-JONES, *Proceedings of the Physical Society* **43**, 461 (1931).
- [16] R. L. C. VINK and J. HORBACH, *Journal of Physics: Condensed Matter* **16**, S3807 (2004).

- [17] S. W. SIDES, G. S. GREY, and M.-D. LACASSE, *Physical Review E* **60**, 6708 (1999).
- [18] M. J. P. NIJMEIJER, A. F. BAKKER, C. BRUIN, and J. H. SIKKENK, *The Journal of Chemical Physics* **89**, 3789 (1988).
- [19] A. HÄRTEL, M. OETTEL, R. E. ROZAS, S. U. EGELHAAF, J. HORBACH, and H. LÖWEN, *Physical Review Letters* **108**, 226101 (2012).
- [20] D. ILVER, A. ARNQVIST, J. GREN, I.-M. FRICK, D. KERSULYTE, E. T. INCECIK, D. E. BERG, A. COVACCI, L. ENGSTRAND, and T. BORN, *Science* **279**, 373 (1998).
- [21] G. A. DE BLAS, A. DARSZON, A. Y. OCAMPO, C. J. SERRANO, L. E. CASTELLANO, E. O. HERNANDEZ-GONZALEZ, M. CHIRINOS, F. LARREA, C. BELTRN, and C. L. TREVIO, *PLOS ONE* **4**, e6095 (2009).
- [22] M. C. MARCHETTI, J. F. JOANNY, S. RAMASWAMY, T. B. LIVERPOOL, J. PROST, M. RAO, and R. A. SIMHA, *Reviews of Modern Physics* **85**, 1143 (2013).
- [23] T. VICSEK, A. CZIRÓK, E. BEN-JACOB, I. COHEN, and O. SHOCHET, *Physical Review Letters* **75**, 1226 (1995).
- [24] J. TONER and Y. TU, *Physical Review E* **58**, 4828 (1998).
- [25] A. CAVAGNA, L. DEL CASTELLO, I. GIARDINA, T. GRIGERA, A. JELIC, S. MELILLO, T. MORA, L. PARISI, E. SILVESTRI, M. VIALE, and A. WALCZAK, *Journal of Statistical Physics* , 1 (2014).
- [26] J. P. CELLI, B. S. TURNER, N. H. AFDHAL, S. KEATES, I. GHIRAN, C. P. KELLY, R. H. EWOLDT, G. H. MCKINLEY, P. SO, S. ERRAMILI, and R. BAN-SIL, *Proceedings of the National Academy of Sciences* **106**, 14321 (2009).
- [27] A. CAVAGNA, A. CIMARELLI, I. GIARDINA, G. PARISI, R. SANTAGATI, F. STEFANINI, and M. VIALE, *Proceedings of the National Academy of Sciences* **107**, 11865 (2010).
- [28] C. BECCO, N. VANDEWALLE, J. DELCOURT, and P. PONCIN, *Physica A* **367**, 487 (2006).
- [29] H. P. ZHANG, A. BEER, E.-L. FLORIN, and H. L. SWINNEY, *Proceedings of the National Academy of Sciences* **107**, 13626 (2010).
- [30] S. J. EBBENS and J. R. HOWSE, *Soft Matter* **6**, 726 (2010).
- [31] I. BUTTINONI, G. VOLPE, F. KÜMMEL, G. VOLPE, and C. BECHINGER, *Journal of Physics: Condensed Matter* **24**, 284129 (2012).
- [32] J. PALACCI, S. SACANNA, S.-H. KIM, G.-R. YI, D. J. PINE, and P. M. CHAIKIN, *Philosophical Transactions of the Royal Society A* **372** (2014).
- [33] Y. FILY and M. C. MARCHETTI, *Physical Review Letters* **108**, 235702 (2012).

- [34] G. S. REDNER, M. F. HAGAN, and A. BASKARAN, *Physical Review Letters* **110**, 055701 (2013).
- [35] J. W. CAHN and J. E. HILLIARD, *The Journal of Chemical Physics* **28**, 258 (1958).
- [36] A. EINSTEIN, *Annalen der Physik* **322**, 549 (1905).
- [37] D. S. LEMONS and A. GYTHIEL, *American Journal of Physics* **65**, 1079 (1997).
- [38] K. PEARSON, *Nature* **72**, 294 (1905).
- [39] M. DOI and H. SEE, *Introduction to polymer physics*, Oxford science publications, Clarendon Press, 1996.
- [40] M. HOLZ, S. R. HEIL, and A. SACCO, *Physical Chemistry Chemical Physics* **2**, 4740 (2000).
- [41] M. LAX, *Reviews of Modern Physics* **38**, 541 (1966).
- [42] M. DOI and S. EDWARDS, *The theory of polymer dynamics*, International series of monographs on physics, Clarendon Press, 1988.
- [43] A. FICK, *Annalen der Physik* **170**, 59 (1855).
- [44] J. PALACCI, S. SACANNA, A. P. STEINBERG, D. J. PINE, and P. M. CHAIKIN, *Science* **339**, 936 (2013).
- [45] I. THEURKAUFF, C. COTTIN-BIZONNE, J. PALACCI, C. YBERT, and L. BOCQUET, *Physical Review Letters* **108**, 268303 (2012).
- [46] G. VOLPE, I. BUTTINONI, D. VOGT, H.-J. KÜMMERER, and C. BECHINGER, *Soft Matter* **7**, 8810 (2011).
- [47] J. E. JONES, *Proceedings of the Royal Society of London. Series A* **106**, 463 (1924).
- [48] J. D. WEEKS, D. CHANDLER, and H. C. ANDERSEN, *The Journal of Chemical Physics* **54**, 5237 (1971).
- [49] P. DEBYE, *Polar molecules*, Dover Publications, 1929.
- [50] A. EINSTEIN, *Annalen der Physik* **324**, 371 (1906).
- [51] M. ALLEN and D. TILDESLEY, *Computer simulation of liquids*, Clarendon Press, 1999.
- [52] D. L. ERMAK and Y. YEH, *Chemical Physics Letters* **24**, 243 (1974).
- [53] G. E. P. BOX and M. E. MULLER, *The Annals of Mathematical Statistics* **29**, 610 (1958).
- [54] W. H. PRESS, S. A. TEUKOLSKY, W. T. VETTERLING, and B. P. FLANNERY, *Numerical Recipes 3rd Edition: The Art of Scientific Computing*, Cambridge University Press, New York, NY, USA, 3 edition, 2007.

- [55] X. LU, Y. HU, and H. CHEN, *Molecular Thermodynamics of Complex Systems, Structure and Bonding*, Springer, 2008.
- [56] B. TEN HAGEN, S. VAN TEEFFELEN, and H. LÖWEN, *Condensed Matter Physics* **12**, 725 (2009).
- [57] B. TEN HAGEN, R. WITTKOWSKI, and H. LÖWEN, *Physical Review E* **84**, 031105 (2011).
- [58] B. TEN HAGEN, S. VAN TEEFFELEN, and H. LÖWEN, *Journal of Physics: Condensed Matter* **23**, 194119 (2011).
- [59] S. BABEL, B. TEN HAGEN, and H. LÖWEN, *Journal of Statistical Mechanics: Theory and Experiment* **2014**, P02011 (2014).
- [60] F. KÜMMEL, B. TEN HAGEN, R. WITTKOWSKI, I. BUTTINONI, R. EICHHORN, G. VOLPE, H. LÖWEN, and C. BECHINGER, *Physical Review Letters* **110**, 198302 (2013).
- [61] F. PERUANI, J. STARRUSS, V. JAKOVLJEVIC, L. SØGAARD-ANDERSEN, A. DEUTSCH, and M. BÄR, *Physical Review Letters* **108**, 098102 (2012).
- [62] F. PERUANI and M. BÄR, *New Journal of Physics* **15**, 065009 (2013).
- [63] Y. HONG, N. M. K. BLACKMAN, N. D. KOPP, A. SEN, and D. VELEGOL, *Physical Review Letters* **99**, 178103 (2007).
- [64] W. F. PAXTON, K. C. KISTLER, C. C. OLMEDA, A. SEN, S. K. ST. ANGELO, Y. CAO, T. E. MALLOUK, P. E. LAMMERT, and V. H. CRESPI, *Journal of the American Chemical Society* **126**, 13424 (2004).
- [65] W. F. PAXTON, P. T. BAKER, T. R. KLINE, Y. WANG, T. E. MALLOUK, and A. SEN, *Journal of the American Chemical Society* **128**, 14881 (2006).
- [66] A. ERBE, M. ZIENTARA, L. BARABAN, C. KREIDLER, and P. LEIDERER, *Journal of Physics: Condensed Matter* **20**, 404215 (2008).
- [67] H.-R. JIANG, N. YOSHINAGA, and M. SANO, *Physical Review Letters* **105**, 268302 (2010).
- [68] R. DREYFUS, J. BAUDRY, M. L. ROPER, M. FERMIGIER, H. A. STONE, and J. BIBETTE, *Nature* **437**, 862 (2005).
- [69] H. KE, S. YE, R. L. CARROLL, and K. SHOWALTER, *The Journal of Physical Chemistry A* **114**, 5462 (2010).
- [70] A. BROWN and W. POON, *Soft Matter* **10**, 4016 (2014).
- [71] M. P. BRENNER, L. S. LEVITOV, and E. O. BUDRENE, *Biophysical Journal* **74**, 1677 (1998).
- [72] R. GOLESTANIAN, T. B. LIVERPOOL, and A. AJDARI, *Physical Review Letters* **94**, 220801 (2005).

- [73] R. GOLESTANIAN, *Physics* **3**, 108 (2010).
- [74] B. SABASS and U. SEIFERT, *The Journal of Chemical Physics* **136**, 214507 (2012).
- [75] B. SABASS and U. SEIFERT, *The Journal of Chemical Physics* **136**, 064508 (2012).
- [76] R. SOTO and R. GOLESTANIAN, *Physical Review Letters* **112**, 068301 (2014).
- [77] S. RAMASWAMY, *Annual Review of Condensed Matter Physics* **1**, 323 (2010).
- [78] F. PERUANI, A. DEUTSCH, and M. BÄR, *Physical Review E* **74**, 030904 (2006).
- [79] I. S. ARANSON, *Comptes Rendus Physique* **14**, 518 (2013).
- [80] E. PUTZIG and A. BASKARAN, *Physical Review E* **90**, 042304 (2014).
- [81] J. DUNKEL, S. HEIDENREICH, K. DRESCHER, H. H. WENSINK, M. BÄR, and R. E. GOLDSTEIN, *Physical Review Letters* **110**, 228102 (2013).
- [82] I. S. ARANSON, D. VOLFSO, and L. S. TSIMRING, *Physical Review E* **75**, 051301 (2007).
- [83] H. H. WENSINK, J. DUNKEL, S. HEIDENREICH, K. DRESCHER, R. E. GOLDSTEIN, H. LÖWEN, and J. M. YEOMANS, *Proceedings of the National Academy of Sciences* **109**, 14308 (2012).
- [84] M. ABKENAR, K. MARX, T. AUTH, and G. GOMPPER, *Physical Review E* **88**, 062314 (2013).
- [85] H. H. WENSINK and H. LÖWEN, *Journal of Physics: Condensed Matter* **24**, 464130 (2012).
- [86] F. D. C. FARRELL, M. C. MARCHETTI, D. MARENDUZZO, and J. TAILLEUR, *Physical Review Letters* **108**, 248101 (2012).
- [87] V. NARAYAN, S. RAMASWAMY, and N. MENON, *Science* **317**, 105 (2007).
- [88] Y. YANG, V. MARCEAU, and G. GOMPPER, *Physical Review E* **82**, 031904 (2010).
- [89] A. GOPINATH, M. F. HAGAN, M. C. MARCHETTI, and A. BASKARAN, *Physical Review E* **85**, 061903 (2012).
- [90] G. BAGLIETTO and E. V. ALBANO, *Physical Review E* **80**, 050103 (2009).
- [91] J. BARRÉ, R. CHÉTRITE, M. MURATORI, and F. PERUANI, *Journal of Statistical Physics* , 1 (2014).
- [92] T. VICSEK and A. ZAFEIRIS, *Physics Reports* **517**, 71 (2012).
- [93] H. LEVINE, W.-J. RAPPEL, and I. COHEN, *Physical Review E* **63**, 017101 (2000).
- [94] Y.-L. CHOU, R. WOLFE, and T. IHLE, *Physical Review E* **86**, 021120 (2012).
- [95] S. K. DAS, S. A. EGOROV, B. TREFZ, P. VIRNAU, and K. BINDER, *Physical Review Letters* **112**, 198301 (2014).

- [96] E. MONES, C. ANDRÁS, and T. VICSEK, *ArXiv e-prints arXiv:1401.0951* (2014).
- [97] A. SUMA, G. GONNELLA, G. LAGHEZZA, A. LAMURA, A. MOSSA, and L. F. CUGLIANDOLO, *Physical Review E* **90**, 052130 (2014).
- [98] H. H. WENSINK, V. KANTSLER, R. E. GOLDSTEIN, and J. DUNKEL, *Physical Review E* **89**, 010302 (2014).
- [99] H. WENSINK, H. LÖWEN, M. MARECHAL, A. HÄRTEL, R. WITTKOWSKI, U. ZIMMERMANN, A. KAISER, and A. MENZEL, *The European Physical Journal Special Topics* **222**, 3023 (2013).
- [100] N. H. P. NGUYEN, D. KLOTSAS, M. ENGEL, and S. C. GLOTZER, *Physical Review Letters* **112**, 075701 (2014).
- [101] B. TEN HAGEN, F. KÜMMEL, R. WITTKOWSKI, D. TAKAGI, H. LÖWEN, and C. BECHINGER, *Nature Communications* **5**, (2014).
- [102] D. F. HINZ, A. PANCHENKO, T.-Y. KIM, and E. FRIED, *Soft Matter* **10**, 9082 (2014).
- [103] L. ANGELANI, C. MAGGI, M. L. BERNARDINI, A. RIZZO, and R. DI LEONARDO, *Physical Review Letters* **107**, 138302 (2011).
- [104] H. H. WENSINK and H. LÖWEN, *Physical Review E* **78**, 031409 (2008).
- [105] A. KAISER, H. H. WENSINK, and H. LÖWEN, *Physical Review Letters* **108**, 268307 (2012).
- [106] A. KAISER, K. POPOWA, H. H. WENSINK, and H. LÖWEN, *Physical Review E* **88**, 022311 (2013).
- [107] A. COSTANZO, J. ELGETI, T. AUTH, G. GOMPPER, and M. RIPOLL, *Europhysics Letters* **107**, 36003 (2014).
- [108] A. KAISER, A. SOKOLOV, I. S. ARANSON, and H. LÖWEN, *ArXiv e-prints arXiv:1411.0964* (2014).
- [109] P. K. GHOSH, P. HÄNGGI, F. MARCHESONI, and F. NORI, *Physical Review E* **89**, 062115 (2014).
- [110] B.-Q. AI and J.-C. WU, *The Journal of Chemical Physics* **140**, (2014).
- [111] Y. FILY, A. BASKARAN, and M. F. HAGAN, *Physical Review E* **91**, 012125 (2015).
- [112] N. KOUMAKIS, A. LEPORE, C. MAGGI, and R. DI LEONARDO, *Nature Communications* **4**, 2588 (2013).
- [113] N. KOUMAKIS, C. MAGGI, and R. DI LEONARDO, *Soft Matter* **10**, 5695 (2014).
- [114] J. ELGETI and G. GOMPPER, *Europhysics Letters* **101**, 48003 (2013).
- [115] Y. FILY, A. BASKARAN, and M. F. HAGAN, *Soft Matter* **10**, 5609 (2014).

- [116] P. K. GHOSH, V. R. MISKO, F. MARCHESONI, and F. NORI, *Physical Review Letters* **110**, 268301 (2013).
- [117] C. REICHHARDT and C. J. OLSON REICHHARDT, *Physical Review E* **90**, 012701 (2014).
- [118] C. REICHHARDT and C. J. O. REICHHARDT, *Physical Review E* **88**, 042306 (2013).
- [119] C. REICHHARDT and C. J. O. REICHHARDT, *Physical Review E* **88**, 062310 (2013).
- [120] B.-Q. AI, Q.-Y. CHEN, Y.-F. HE, F.-G. LI, and W.-R. ZHONG, *Physical Review E* **88**, 062129 (2013).
- [121] S. A. MALLORY, A. ŠARIĆ, C. VALERIANI, and A. CACCIUTO, *Physical Review E* **89**, 052303 (2014).
- [122] D. LEVIS and L. BERTHIER, *Physical Review E* **89**, 062301 (2014).
- [123] C. J. OLSON REICHHARDT, D. RAY, and C. REICHHARDT, *Proceedings SPIE* **9164**, 91641N (2014).
- [124] E. YARIV and O. SCHNITZER, *Physical Review E* **90**, 032115 (2014).
- [125] M. TARAMA, A. M. MENZEL, B. TEN HAGEN, R. WITTKOWSKI, T. OHTA, and H. LÖWEN, *The Journal of Chemical Physics* **139**, (2013).
- [126] M. TARAMA, A. M. MENZEL, and H. LÖWEN, *Physical Review E* **90**, 032907 (2014).
- [127] M. TARAMA and T. OHTA, *The European Physical Journal B* **83**, 391 (2011).
- [128] M. TARAMA and T. OHTA, *Progress of Theoretical and Experimental Physics* **2013** (2013).
- [129] M. TARAMA and T. OHTA, *Physical Review E* **87**, 062912 (2013).
- [130] M. TARAMA and T. OHTA, *Journal of Physics: Condensed Matter* **24**, 464129 (2012).
- [131] J. R. HOWSE, R. A. L. JONES, A. J. RYAN, T. GOUGH, R. VAFABAKHSH, and R. GOLESTANIAN, *Physical Review Letters* **99**, 048102 (2007).
- [132] J. TAILLEUR and M. E. CATES, *Physical Review Letters* **100**, 218103 (2008).
- [133] M. E. CATES and J. TAILLEUR, *ArXiv e-prints* **arXiv:1406.3533** (2014).
- [134] M. E. CATES, D. MARENUZZO, I. PAGONABARRAGA, and J. TAILLEUR, *Proceedings of the National Academy of Sciences* **107**, 11715 (2010).
- [135] G. S. REDNER, A. BASKARAN, and M. F. HAGAN, *Physical Review E* **88**, 012305 (2013).
- [136] Y. FILY, S. HENKES, and M. C. MARCHETTI, *Soft Matter* **10**, 2132 (2014).

- [137] T. SHEN, X. QI, and R. B. NELLAS, *The Journal of Physical Chemistry B* **117**, 12844 (2013).
- [138] R. GOLESTANIAN, *Physical Review Letters* **108**, 038303 (2012).
- [139] J. STENHAMMAR, A. TIRIBOCCHI, R. J. ALLEN, D. MARENDUZZO, and M. E. CATES, *Physical Review Letters* **111**, 145702 (2013).
- [140] A. P. SOLON and J. TAILLEUR, *Physical Review Letters* **111**, 078101 (2013).
- [141] A. WYSOCKI, R. G. WINKLER, and G. GOMPPER, *Europhysics Letters* **105**, 48004 (2014).
- [142] B. M. MOGNETTI, A. ŠARIĆ, S. ANGIOLETTI-UBERTI, A. CACCIUTO, C. VALERIANI, and D. FRENKEL, *Physical Review Letters* **111**, 245702 (2013).
- [143] O. POHL and H. STARK, *Physical Review Letters* **112**, 238303 (2014).
- [144] C. REICHHARDT and C. J. OLSON REICHHARDT, *Soft Matter* **10**, 7502 (2014).
- [145] J. BIALKÉ, T. SPECK, and H. LÖWEN, *Physical Review Letters* **108**, 168301 (2012).
- [146] L. BERTHIER and J. KURCHAN, *Nature Physics* **9**, 310 (2013).
- [147] L. BERTHIER, *Physical Review Letters* **112**, 220602 (2014).
- [148] R. NI, M. A. C. STUART, and M. DIJKSTRA, *Nature Communications* **4**, 2704 (2013).
- [149] R. NI, M. A. COHEN STUART, M. DIJKSTRA, and P. G. BOLHUIS, *Soft Matter* **10**, 6609 (2014).
- [150] M. KOHL, A. V. IVLEV, P. BRANDT, G. E. MORFILL, and H. LÖWEN, *Journal of Physics: Condensed Matter* **24**, 464115 (2012).
- [151] T. GLANZ and H. LÖWEN, *Journal of Physics: Condensed Matter* **24**, 464114 (2012).
- [152] T. VISSERS, A. WYSOCKI, M. REX, H. LÖWEN, C. P. ROYALL, A. IMHOF, and A. VAN BLAADEREN, *Soft Matter* **7**, 2352 (2011).
- [153] A. M. MENZEL, *Physical Review E* **85**, 021912 (2012).
- [154] J. YVON, *La Theorie statistique des fluides et l'equation d'etat*, Hermann, Paris, 1935.
- [155] N. BOGOLYUBOV, *Journal of Physics USSR* **10**, 265 (1946).
- [156] J. G. KIRKWOOD, *The Journal of Chemical Physics* **14**, 180 (1946).
- [157] M. BORN and H. S. GREEN, *Proceedings of the Royal Society of London. Series A* **188**, 10 (1946).
- [158] J. G. KIRKWOOD, *The Journal of Chemical Physics* **15**, 72 (1947).

- [159] J. HANSEN and I. McDONALD, *Theory of Simple Liquids*, Elsevier Science, 3rd edition, 2006.
- [160] A. BASKARAN and M. C. MARCHETTI, *Proceedings of the National Academy of Sciences* **106**, 15567 (2009).
- [161] J. TONER and Y. TU, *Physical Review Letters* **75**, 4326 (1995).
- [162] M. E. CATES and J. TAILLEUR, *Europhysics Letters* **101**, 20010 (2013).
- [163] M. SUZUKI, *Progress of Theoretical Physics* **58**, 1142 (1977).
- [164] K. BINDER, *Zeitschrift für Physik B Condensed Matter* **43**, 119 (1981).
- [165] A. PELISSETTO and E. VICARI, *Physics Reports* **368**, 549 (2002).
- [166] E. ISING, *Zeitschrift für Physik* **31**, 253 (1925).
- [167] A. LANG, C. N. LIKOS, M. WATZLAWEK, and H. LÖWEN, *Journal of Physics: Condensed Matter* **12**, 5087 (2000).
- [168] F. H. STILLINGER, *The Journal of Chemical Physics* **65**, 3968 (1976).
- [169] B. V. DERJAGUIN and L. LANDAU, *Acta Physicochimica URSS* **14**, 633 (1941).
- [170] E. J. VERWEY and J. T. G. OVERBEEK, *Theory of the stability of Lyophobic Colloids*, Elsevier, Amsterdam, 1948.
- [171] A. ZÖTTL and H. STARK, *Physical Review Letters* **112**, 118101 (2014).
- [172] T. ISHIKAWA, M. P. SIMMONDS, and T. J. PEDLEY, *Journal of Fluid Mechanics* **568**, 119 (2006).
- [173] J. R. BLAKE, *Journal of Fluid Mechanics* **46**, 199 (1971).
- [174] M. YANG, A. WYSOCKI, and M. RIPOLL, *Soft Matter* **10**, 6208 (2014).
- [175] J. STENHAMMAR, D. MARENDUZZO, R. J. ALLEN, and M. E. CATES, *Soft Matter* **10**, 1489 (2014).
- [176] R. MATAS-NAVARRO, R. GOLESTANIAN, T. B. LIVERPOOL, and S. M. FIELDING, *Physical Review E* **90**, 032304 (2014).
- [177] J. STENHAMMAR, R. WITTKOWSKI, D. MARENDUZZO, and M. E. CATES, *Physical Review Letters* **114**, 018301 (2015).
- [178] J. G. KIRKWOOD, *The Journal of Chemical Physics* **3**, 300 (1935).
- [179] M. HILLERT, *A Theory of nucleation for solid metallic solutions*, Massachusetts Institute of Technology. Department of Metallurgy, 1956.
- [180] M. HILLERT, *Acta Metallurgica* **9**, 525 (1961).
- [181] J. P. HANSEN, D. LEVESQUE, and J. ZINN-JUSTIN, *Liquids, Freezing and the Glass Transition : Part I (Les Houches Summer School Proceedings)*, North-Holland, 1991.

- [182] S. K. DAS, M. E. FISHER, J. V. SENEGERS, J. HORBACH, and K. BINDER, *Physical Review Letters* **97**, 025702 (2006).
- [183] A. CHEN, E. H. CHIMOWITZ, S. DE, and Y. SHAPIR, *Physical Review Letters* **95**, 255701 (2005).
- [184] P. C. HOHENBERG and B. I. HALPERIN, *Reviews of Modern Physics* **49**, 435 (1977).
- [185] A. P. SOLON, H. CHATÉ, and J. TAILLEUR, *ArXiv e-prints arXiv:1406.6088* (2014).
- [186] J. SCHWARZ-LINEK, C. VALERIANI, A. CACCIUTO, M. E. CATES, D. MAREN-DUZZO, A. N. MOROZOV, and W. C. K. POON, *Proceedings of the National Academy of Sciences* **109**, 4052 (2012).
- [187] R. WITTKOWSKI, A. TIRIBOCCHI, J. STENHAMMAR, R. J. ALLEN, D. MAREN-DUZZO, and M. E. CATES, *Nature Communications* **5**, (2014).
- [188] J. PALACCI, C. COTTIN-BIZONNE, C. YBERT, and L. BOCQUET, *Physical Review Letters* **105**, 088304 (2010).
- [189] G. SZAMEL, *Physical Review E* **90**, 012111 (2014).
- [190] J. TAILLEUR and M. E. CATES, *Europhysics Letters* **86**, 60002 (2009).
- [191] P. HOHENBERG and W. KOHN, *Physical Review* **136**, B864 (1964).
- [192] N. D. MERMIN, *Physical Review* **137**, A1441 (1965).
- [193] C. EBNER, W. F. SAAM, and D. STROUD, *Physical Review A* **14**, 2264 (1976).
- [194] R. EVANS, *Advances in Physics* **28**, 143 (1979).
- [195] U. M. B. MARCONI and P. TARAZONA, *The Journal of Chemical Physics* **110**, 8032 (1999).
- [196] V. GINZBURG and L. LANDAU, *Zhurnal Eksperimentalnoi i Teoreticheskoi Fiziki* **20**, 1064 (1950).
- [197] P. HARTMANN, G. J. KALMAN, Z. DONKÓ, and K. KUTASI, *Physical Review E* **72**, 026409 (2005).
- [198] A. NOVICK-COHEN, *Journal of Statistical Physics* **38**, 707 (1985).
- [199] M. C. CROSS and P. C. HOHENBERG, *Reviews of Modern Physics* **65**, 851 (1993).
- [200] V. L. GERTSBERG and G. I. SIVASHINSKY, *Progress of Theoretical Physics* **66**, 1219 (1981).
- [201] J. WALTON, D. TILDESLEY, J. ROWLINSON, and J. HENDERSON, *Molecular Physics* **48**, 1357 (1983).
- [202] F. SCHMITZ, P. VIRNAU, and K. BINDER, *Physical Review E* **90**, 012128 (2014).
- [203] J. ROWLINSON, *Molecular Physics* **7**, 349 (1964).

- [204] J. ROWLINSON, *Molecular Physics* **8**, 107 (1964).
- [205] J. A. BARKER and D. HENDERSON, *The Journal of Chemical Physics* **47**, 4714 (1967).
- [206] D. HENDERSON, *Journal of Chemical and Engineering Data* **55**, 4507 (2010).
- [207] H. WEBER, D. MARX, and K. BINDER, *Physical Review B* **51**, 14636 (1995).
- [208] H. WEBER and D. MARX, *Europhysics Letters* **27**, 593 (1994).
- [209] S. C. TAKATORI and J. F. BRADY, *ArXiv e-prints* **arXiv:1411.5776** (2014).
- [210] F. GINOT, I. THEURKAUFF, D. LEVIS, C. YBERT, L. BOCQUET, L. BERTHIER, and C. COTTIN-BIZONNE, *ArXiv e-prints* **arXiv:1411.7175** (2014).
- [211] E. H. A. DE HOOG and H. N. W. LEKKERKERKER, *The Journal of Physical Chemistry B* **103**, 5274 (1999).
- [212] B.-H. CHEN, B. PAYANDEH, and M. ROBERT, *Physical Review E* **62**, 2369 (2000).
- [213] S. C. TAKATORI, W. YAN, and J. F. BRADY, *Physical Review Letters* **113**, 028103 (2014).
- [214] S. C. TAKATORI and J. F. BRADY, *Soft Matter* **10**, 9433 (2014).
- [215] R. E. ROZAS and J. HORBACH, *Europhysics Letters* **93**, 26006 (2011).
- [216] J. SIKKENK, J. V. LEEUWEN, E. VOSSNACK, and A. BAKKER, *Physica A* **146**, 622 (1987).
- [217] B. SMIT and D. FRENKEL, *The Journal of Chemical Physics* **94**, 5663 (1991).
- [218] M. SANTRA, S. CHAKRABARTY, and B. BAGCHI, *The Journal of Chemical Physics* **129**, (2008).
- [219] F. P. BUFF, R. A. LOVETT, and F. H. STILLINGER, *Physical Review Letters* **15**, 621 (1965).
- [220] J. D. WEEKS, *The Journal of Chemical Physics* **67**, 3106 (1977).
- [221] M. P. A. FISHER, D. S. FISHER, and J. D. WEEKS, *Physical Review Letters* **48**, 368 (1982).
- [222] D. BEDEAUX and J. D. WEEKS, *The Journal of Chemical Physics* **82**, 972 (1985).
- [223] K. BINDER, M. MÜLLER, F. SCHMID, and A. WERNER, *Advances in Colloid and Interface Science* **94**, 237 (2001).
- [224] A. P. SOLON, Y. FILY, A. BASKARAN, M. E. CATES, Y. KAFRI, M. KARDAR, and J. TAILLEUR, *ArXiv e-prints* **arXiv:1412.3952** (2014).

Eidesstattliche Versicherung

Ich versichere an Eides Statt, dass die Dissertation von mir selbständig und ohne unzulässige fremde Hilfe unter Beachtung der Grundsätze zur Sicherung guter wissenschaftlicher Praxis an der Heinrich-Heine-Universität Düsseldorf erstellt worden ist.

Düsseldorf, den 02.02.2015

Alexander Julian Marcel Bialké